Part 2:

Application of Finite Element Technology to Topology Optimization

Chapter 5

New schemes to deal with problematic material layouts exploiting elements with drilling degrees of freedom

5.1 Summary

In this chapter, the use of membrane finite elements with drilling degrees of freedom (to be denoted Q4X) in topology optimization is investigated. Special attention is paid to their use in schemes to treat problematic material layouts resulting from numerical instabilities, e.g. checkerboarding and one-node connected hinges. A treatment for a less prominent problem, termed the diagonal member herein, is also suggested.

Firstly it is shown that the severity of checkerboarding is significantly reduced when employing elements with drilling degrees of freedom (DOFs), as compared to results obtained using standard Q4 elements. The salient features of elements with drilling DOFs are further exploited in the development of new methods to treat one-node hinges and diagonal members.

As an application, topology optimization is applied in the design of a piezoelectrically driven micropositioner. Typically, such devices are designed on an inefficient trial-and-error basis, whereas in this study topology optimization is applied as a design tool, to somewhat automate the process. The mechanism employs two piezoelectric stack actuators in a push-pull configuration to provide the input displacement. Various objective and constraint functions, including simply maximizing output rotation, as well as maximizing stiffness measures subject to a required rotation being maintained, are investigated. In each case, unsuitable results are achieved due to the presence of one-node connected hinges in 'optimal' designs. Finally, the most promising of the two proposed schemes is successfully applied to improve upon designs achieved using conventional Q4 elements and filter strategies.

5.2 Introduction

In membrane and shell elements, drilling degrees of freedom (DOFs) are highly desirable. They allow for the modeling of, for instance, folded plates and beam-slab intersections. Due to the enriched displacement field, these elements are also significantly more accurate than their counterparts with translational DOFs only [21]. For bending dominated problems for example, drilling DOFs enhance the accuracy of 4-node elements to a level comparable to that of 8- or 9-node elements, while the 4-node element with only translational DOFs (Q4) is notoriously inaccurate. The computational effort associated with elements with drilling DOFs is low, since the connectivity of the assembled structural stiffness matrix is comparable to that of Q4.

While most commercial finite element codes include elements with an in-plane rotational DOFs, in some cases these 'vertex' rotations are artificial. In contrast, the membrane finite elements with drilling rotations used in the problems herein, are based on the continuum mechanics definition of in-plane rotations. In Chapter 2 a brief overview of these elements was presented in an elastostatics setting, and some accuracy and stability issues were addressed. In Chapter 3 the focus was on elements with drilling DOFs in the context of the piezoelectricity problem.

In this chapter, the use of the elements developed in Chapters 2 and 3 are employed in a topology optimization environment. A reasonably detailed introduction to topology optimization using the SIMP (Simple Isotropic Material with Penalization) material parameterization is presented in Appendix A. Also discussed are common numerical instabilities, as well as previously proposed methods to deal with them.

Specifically, the utility of elements with drilling DOFs to deal with checkerboarding, one-node hinges and diagonal members is investigated. Checkerboarding is characterized by material being distributed in alternating solid and void elements in a checkerboard-like pattern, as depicted in Figure 5.1(a). A one-node connected hinge occurs when two diagonally opposite elements are solid while the other two surrounding elements are void as illustrated in Figure 5.1(b). Finally, diagonal members (which have received far less attention than either checkerboarding or one-node hinges[1]) are formed by multiple diagonally connected elements as depicted in Figure 5.1(c). In each case, the numerical model of these layouts is poor, the checkerboard being over-stiff and the one-node hinge representing a perfect (impractical) hinge with zero rotational stiffness. On the other hand, the numerical model of a diagonal member subjected to axial loads is acceptable, while in bending it is unacceptably flexible.

Firstly, it is shown, by numerical example, that simply employing elements with drilling DOFs, instead of standard Q4 elements, results in a significant reduction in checkerboarding severity. Additionally, two new schemes to treat specifically one-node connected hinges and diagonal structural members, are suggested. In principle, the first scheme uses the rotations computed at interior nodes to detect excessive rotations at suspect nodes. The second scheme essentially replaces planar elements forming a one-node hinge, where appropriate,

[1] In fairness, many of the methods to deal with checkerboarding and one-node hinges will also prevent diagonal members. However some do not, see for example [98].

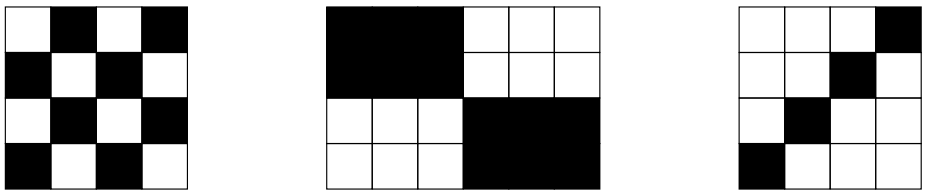

(a) (b) (c)

Figure 5.1: Checkerboard, diagonal member and one node hinge material layouts: (a) checkerboard. (b) one node hinge, (c) diagonal member.

with a more realistic beam model of the material layout while other elements in the mesh are modelled using planar elements as usual. Instead of only evaluating these new schemes on popular test problems, such as the MBB beam or the force inverter, their application is extended to the practical design of a compliant mechanism for micropositioning applications. The device under investigation is a prototype, designed to demonstrate capability for an infrared optical system.

In infrared detectors in particular, the detector elements need to be relatively large and sufficiently isolated from one another. The result is therefore a relatively sparse detector array often with insufficient density to prevent image aliasing. A possible method to improve resolution is to mount the detector array on a piezoelectric actuator, to collect the lost part of the image. To be feasible however, this would need to be accommodated in the design phase of the optical system. A further possibility (the one considered here) is to retro-fit existing infrared cameras with an actuator that manipulates other optical devices, such as lenses or mirrors, in order to recover lost parts of the image.

The design problem is formulated using three different optimization statements. The first requires only that the rotation of a mirror be maximised. In the other two formulations, a measure of mechanism stiffness is maximised, subject to a mirror rotation requirement being met. Upon inspection of the designs resulting from this optimization process, using Q4 elements and standard filter techniques, unsatisfactory one-node hinges are found at points where significant bending is required. Therefore, the most promising of the two newly developed schemes is applied to improve on these results.

This chapter is set out as follows: In Section 5.3 elements with drilling DOFs are briefly re-capped, while in Section 5.4 the topology optimization problem formulations, for all examples evaluated in this chapter, are presented. In Section 5.4.2 the effect of element formulation on checkerboarding is briefly considered. Two new schemes to deal with one-node hinges and diagonal members are presented in Section 5.5. Numerical results are presented in Section 5.6 and finally concluding remarks are related in Section 5.7.

5.3 Elements with drilling degrees of freedom

For completeness, in this section a very short introduction to elements with drilling DOFs is presented in no detail whatsoever. Further details regarding elastic elements can be found in, for instance [18, 21] and in the other references in Chapter 2. This formulation has also been extended to piezoelectric materials and the resulting planar piezoelectric elements with drilling DOFs can be found in Chapter 3 and Long *et al.* [80].

Usually planar elements possess only two (translational) DOFs per node. Formulations with a third (in-plane rotational) degree of freedom result in elements with superior accuracy, and modelling capabilities. For example, planar configurations such as beam-slab connections can be modelled, and when the planar elements are combined with plate elements, folded plates can be modelled properly.

In this work, the standard 4-node bilinear quadrilateral elements *without* drilling DOFs will be denoted Q4, while the corresponding elements *with* drilling DOFs will be denoted Q4X. Finally, 9-node Lagrangian elements (*without* drilling DOFs) are labeled Q9.

5.4 Problem formulations

In this chapter, a number of different topology optimization problems, all using the SIMP material model, are considered. For convenience and ease of reference, in this section details of *all* test problem formulations are given. The first (and simplest) is the minimum compliance problem. This problem is often used to benchmark newly proposed procedures since reference solutions[2] exist for many problems, including the MBB beam problem. Minimum compliance problems will be used to numerically determine the effect of element formulation on checkerboarding.

Since one-node connected hinges are more common in compliant mechanism design problems than in minimum compliance problems, the efficacy of our new schemes will be evaluated on popular compliant mechanism topology optimization problems[3].

Finally, a topology optimization procedure is employed in the design of a practical compliant mechanism. The device under consideration is a demonstrator mirror scanning device for optical applications. For comparison, the problem is posed using three different formulations. In the remainder of this section, the afforementioned problems are described in more detail.

Unless otherwise specified, a penalty value of $p = 3$ is employed throughout.

[2] At least qualitative solutions are known [99]. Generally authors do not publish objective function values, or only present normalised values making quantitative comparisons difficult.

[3] Once again, only qualitative comparisons will be made with results for problems such as the force inverter.

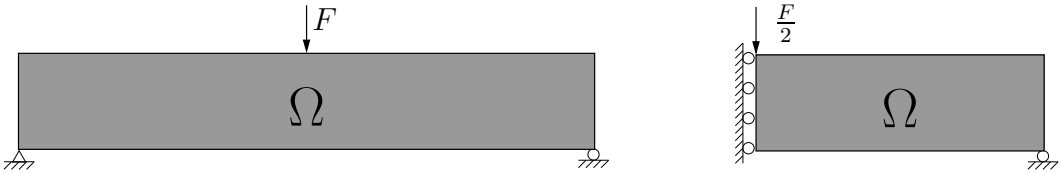

(a) (b)

Figure 5.2: The minimum compliance problem for the MMB beam: (a) Full model, (b) symmetric model.

5.4.1 The minimum compliance topology optimization problem using SIMP

The minimum compliance problem seeks to find the material distribution which maximizes the global stiffness, subject to a bound on the available material. The discrete form of the minimum compliance problem employing the SIMP material model can be written as:

$$\min_{\boldsymbol{\rho}} \; c(\boldsymbol{\rho}) \tag{5.1}$$

$$\text{such that} \; : v(\boldsymbol{\rho}) = \frac{1}{v_\Omega}\left(\sum_{i=1}^{Nel} \rho_i v_i\right) - v^* \leq 0 \tag{5.2}$$

$$: \boldsymbol{KU} = \boldsymbol{F} \tag{5.3}$$

$$: \mathbf{0} \leq \boldsymbol{\rho}_{\min} \leq \boldsymbol{\rho} \leq \mathbf{1}, \tag{5.4}$$

where compliance is calculated, for the planar problem depicted in Figure 5.2, as

$$c(\boldsymbol{\rho}) = \boldsymbol{F}^T\boldsymbol{U} = \boldsymbol{U}^T\boldsymbol{KU} = \sum_{i=1}^{Nel}(\rho_i)^p \boldsymbol{u}_i^T \boldsymbol{k}_i^0 \boldsymbol{u}_i. \tag{5.5}$$

In the foregoing, c is the compliance, $\boldsymbol{\rho}$ is the vector of design variables (representing elemental densities) made up of elemental values ρ_i, $i = 1, 2, ..., Nel$. In order to prevent singularities in the finite element analysis, a lower bound on the densities is imposed, denoted $\boldsymbol{\rho}_{\min}$. Furthermore, v_Ω is the volume of the design domain Ω, v_i is the volume of each element, and v^* is an upper bound on the permissible volume fraction. The volume constraint (not the actual material volume) is denoted $v(\boldsymbol{\rho})$. Finally, $\boldsymbol{U}$ and $\boldsymbol{F}$ are the global assembled displacement and force vectors, $\boldsymbol{K}$ is the global stiffness matrix, and $\boldsymbol{u}_i$ and $\boldsymbol{k}_i^0$ are the elemental displacement vector and the stiffness matrix of a solid element respectively.

If the force is not design dependant, the sensitivity of compliance to the density of a given element ρ_i is

$$\frac{\partial c}{\partial \rho_i} = \boldsymbol{F}^T \frac{\partial \boldsymbol{U}}{\partial \rho_i}, \tag{5.6}$$

where $\frac{\partial \boldsymbol{U}}{\partial \rho_i}$ can be found using (5.3) as

$$\frac{\partial \boldsymbol{U}}{\partial \rho_i} = -\boldsymbol{K}^{-1}\frac{\partial \boldsymbol{K}}{\partial \rho_i}\boldsymbol{U}. \tag{5.7}$$

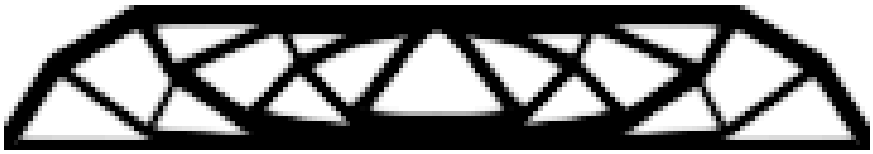

Figure 5.3: A reference optimal topology for the MBB beam discretized using 180×30 elements.

Now, combining (5.6) and (5.7) gives:

$$\frac{\partial c}{\partial \rho_i} = -\boldsymbol{F}^T \boldsymbol{K}^{-1} \frac{\partial \boldsymbol{K}}{\partial \rho_i} \boldsymbol{U}. \tag{5.8}$$

Equation (5.8) can be shown to further reduce to

$$\frac{\partial c}{\partial \rho_i} = -\boldsymbol{U}^T \frac{\partial \boldsymbol{K}}{\partial \rho_i} \boldsymbol{U} = -p(\rho_i)^{p-1} \boldsymbol{u}_i^T \boldsymbol{k}_i^0 \boldsymbol{u}_i, \tag{5.9}$$

which contains only elemental quantities.

Finally, the sensitivity of the volume constraint can simply be written as

$$\frac{\partial v}{\partial \rho_i} = \frac{v_i}{v_\Omega}. \tag{5.10}$$

For comparison, Figure 5.3 depicts a reference optimal topology for the MBB beam problem depicted in Figure 5.2. To avoid checkerboarding, the sensitivities of the objective function are filtered using the methods suggested by Sigmund [100]. The solution is computed using a heuristic updating scheme proposed by Bendsøe [4, 101], based on standard optimality criterion methods. The scheme for updating the elemental densities is expressed as:

$$\rho_i^{\text{new}} = \begin{cases} \max(\rho_{\min}, \rho_i - m) & \text{if} \quad \rho_i B_i^\eta \leq \max(\rho_{\min}, \rho_i - m) \\ \rho_i B_i^\eta & \text{if} \quad \max(\rho_{\min}, \rho_i - m) < \rho_i B_i^\eta < \min(1, \rho_i + m) \\ \min(1, \rho_i + m) & \text{if} \quad \min(1, \rho_i + m) \leq \rho_i B_i^\eta \end{cases} \tag{5.11}$$

where m is a move limit, $\eta (= \frac{1}{2})$ is a numerical damping coefficient and B_i is found from the optimality condition as

$$B_i = \frac{-\dfrac{\partial c}{\partial \rho_i}}{\lambda \dfrac{\partial v}{\partial \rho_i}}, \tag{5.12}$$

where λ is a Lagrange multiplier found using a bisection algorithm. A more complete derivation of B_i can be found, for example in [4].

In order to reduce the likelihood of convergence to local minima, the penalty parameter p is increased slowly from 1 to 3 during the optimization procedure. In the following paragraphs, some brief comments on checkerboarding in minimum compliance problems are presented.

(a) (b) (c)

Figure 5.4: MBB beam optimal designs for a 30×90 mesh employing: (a) Q4 elements, (b) Q9 elements, (c) Q4X elements.

5.4.2 Comments on checkerboarding

Checkerboarding is a numerical instability, commonly observed in reported solutions of minimum compliance problems. It is characterized by material being distributed in alternating solid and void elements in a checkerboard-like pattern. The numerical model of this material layout is poor, and appears over-stiff as detailed in [14, 102] and Chapter 7. Although filters are frequently used to reduce or eliminate this effect, the use of filters complicates interpretation of results, due to their largely heuristic nature. It is well known that under certain circumstances, checkerboarding is eliminated when higher order elements (Q8 or Q9) are used. These elements, however, greatly increase the time required to solve the structural problem due to the higher number of nodes per element and the reduced sparsity of the stiffness matrix.

A more detailed theoretical study of checkerboarding, investigating the effect of various planar element formulations, is presented in Chapter 7 and therefore only selected numerical results will be presented here. In each case, results are computed using the heuristic updating scheme based on optimality criteria, see (5.11). To reduce the likelihood of convergence to local minima, the penalty parameter is increased linearly from 1 to 3 in 33 iterations and held at $p = 3$ for a further 16 iterations.

Figure 5.4 illustrates the effect of element formulation on the optimal topology of the popular MBB beam problem. This problem is detailed in Section 5.4.1 and a reference solution employing the mesh independency filter due to Sigmund is depicted in Figure 5.3. Note that in Figure 5.4 only the topology of the symmetric model, see Figure 5.2(b), is depicted.

As is well known, Q4 elements are prone to checkerboard layouts, as depicted in Figure 5.4(a), while in most cases, Q9 elements eliminate checkerboards in the optimal design, see Figure 5.4(b). Elements with drilling DOFs are shown here to significantly reduce the amount of checkerboarding in the optimal layout, as depicted in Figure 5.4(c). In fact, in a number of test problems employing elements with drilling DOFs, checkerboarding has only been observed in diagonal structural members, similar to those in Figure 5.4(c).

Although checkerboarding is not completely eliminated upon application of elements with drilling DOFs, the resulting topology is considered more usable than that found using Q4 elements. Major features of the topology, found using elements with drilling DOFs, will not be lost after a 'smoothing' post-processing step, unlike the result found with Q4 elements. It is however explained in Chapter 7, that it is not possible completely prevent checkerboarding

by mere application of elements with drilling DOFs. Additionally, it is shown that only if the skew-symmetric part of the displacement gradient is non-zero will checkerboarding be (slightly) alleviated.

Finally, in an attempt to highlight the numerical cost benefits of employing lower order elements, the time required to solve for $\boldsymbol{U}$ in $\boldsymbol{KU} = \boldsymbol{F}$, was recorded for one iteration of the MBB beam problem, using Q4, Q9, and elements with drilling DOFs. When the computational effort (in CPU seconds) is normalized with respect to that of the Q4 results, the effort using elements with drilling DOFs is 1.80, while the relative effort with Q9 elements is 11.19, illustrating the significant saving achieved when using lower order elements.

We now return to the presentation of the various topology optimization problem formulations used to evaluate the proposed schemes.

5.4.3 Compliant mechanism design using topology optimization and SIMP

Compliant mechanism design employing topology optimization, involves seeking the optimal material distribution within a design domain which optimizes a given objective function (usually maximizing a certain displacement) while subject to a limit on the available material. To illustrate, the popular force inverter problem is used, with the problem graphically depicted in Figure 5.5. The goal is to maximise the output displacement, in the direction opposite to the applied force. The problem may be formulated, similar to the minimum compliance problem, as

$$\max_{\boldsymbol{\rho}} \; u_{\text{out}}(\boldsymbol{\rho}) \tag{5.13}$$

$$\text{such that} \;\; : v(\boldsymbol{\rho}) = \frac{1}{v_\Omega}\left(\sum_{i=1}^{Nel} \rho_i v_i\right) - v^* \leq 0 \tag{5.14}$$

$$: \boldsymbol{KU} = \boldsymbol{F} \tag{5.15}$$

$$: \mathbf{0} \leq \boldsymbol{\rho}_{\min} \leq \boldsymbol{\rho} \leq \mathbf{1}, \tag{5.16}$$

where u_{out} is the output displacement. The output displacement can be extracted from the solution of the equilibrium equations (5.15) and is given by

$$u_{\text{out}} = \boldsymbol{L}^T \boldsymbol{U}. \tag{5.17}$$

In (5.17), $\boldsymbol{L}$ is a unit vector in the desired output direction within the finite element space. In the case of the force inverter depicted in Figure 5.5, $\boldsymbol{L}$ is a vector with a single non-zero (unit) entry corresponding to the DOF which extracts u_{out} from $\boldsymbol{U}$.

In a process similar to that used to compute the sensitivities of compliance, the sensitivity of u_{out} to the design variables $\boldsymbol{\rho}$ can be found using (5.15) and (5.17):

$$\frac{\partial u_{\text{out}}}{\partial \rho_i} = \boldsymbol{L}^T \frac{\partial \boldsymbol{U}}{\partial \rho_i}, \tag{5.18}$$

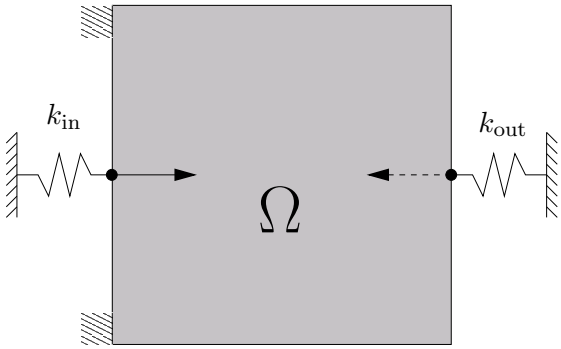

Figure 5.5: Compliant mechanism design of a force inverter.

where from (5.15),

$$\frac{\partial \boldsymbol{U}}{\partial \rho_i} = -\boldsymbol{K}^{-1}\frac{\partial \boldsymbol{K}}{\partial \rho_i}\boldsymbol{U}. \tag{5.19}$$

Combining (5.18) and (5.19) results in

$$\frac{\partial u_{\text{out}}}{\partial \rho_i} = -\boldsymbol{L}^T\boldsymbol{K}^{-1}\frac{\partial \boldsymbol{K}}{\partial \rho_i}\boldsymbol{U}, \tag{5.20}$$

which can, using the fact that $\boldsymbol{K}$ is symmetric and positive definite, in turn be rewritten as

$$\frac{\partial u_{\text{out}}}{\partial \rho_i} = -\boldsymbol{\lambda}^T\frac{\partial \boldsymbol{K}}{\partial \rho_i}\boldsymbol{U}. \tag{5.21}$$

In this case, $\boldsymbol{\lambda}$ is the solution of the adjoint problem

$$\boldsymbol{K}\boldsymbol{\lambda} = \boldsymbol{L}. \tag{5.22}$$

Finally, the sensitivity of u_{out} can be written in terms of only elemental quantities as

$$\frac{\partial u_{\text{out}}}{\partial \rho_i} = -p(\rho_i)^{p-1}\boldsymbol{\lambda}_i^T\boldsymbol{k}_i^0\boldsymbol{u}_i, \tag{5.23}$$

where $\boldsymbol{\lambda}_i$ is the elemental vector (for element i) of displacements associated with the adjoint load, $\boldsymbol{k}_i^0$ is the stiffness matrix of solid element i and $\boldsymbol{u}_i$ is the displacements of the original problem for element i.

An illustrative reference solution to the force inverter problem is depicted in Figure 5.6. Once again, the heuristic updating scheme, with some minor adjustments to improve stability, is employed in the solution. In this particular solution, the formation of one-node hinges are clearly visible even though the mesh-independency filter of Sigmund is again employed.

5.4.4 Mirror scanning design using topology optimization and SIMP

In this section a traditional topology optimization procedure, using standard filtering techniques, is employed in the design of a prototype mirror microscanning device. The objective

Figure 5.6: A reference optimal topology for the force inverter problem using 48×48 elements.

of the designed mechanism is to rotate a mirror about a single axis, and thereby accurately position the reflected image. Our design employs two 18×5×5mm piezoelectric stack actuators in a push-pull configuration.

Since this application represents a prototype design, the size and shape of a representative design domain is simply estimated. The focus of this work is not on the optimal placement of the piezoelectric actuator, since this issue has already been addressed, see Frecker [103] for examples. Therefore, in order to determine a suitable position for the piezoelectric stack, topology optimization trials, with various stack positions, were performed.

After determining a suitable stack position, the optimization problem was run several times with random starting points. Due to the global nature of the problem, approximately 70% of the randomly seeded designs resulted in a double-lever mechanism, while the remainder terminated in local inferior optima. Therefore, in order to ensure the required load-path for this type of mechanism in the initial stages of the optimization procedure, a double-lever mechanism is seeded as a starting point. These topology optimization trials further revealed that an output rotation of around 1° is comfortably realized, which translates to a tip displacement of approximately 0.5mm. The selected initial design with fixed stack position is shown in Figure 5.7. The figure identifies the design domain as well as passive (solid and void) regions.

In the results to follow, anti-symmetry is used to model the mechanism as illustrated in Figure 5.7(b), and the optimization problem is solved with the method of moving asymptotes (MMA) due to Svanberg [10]. The sensitivities of the objective functions have once again been modified with the mesh independency filter of Sigmund [100] to avoid checkerboarding. In the remainder of this section, the formulation of, and results for, the three different problem formulations are presented.

Mirror scanning device: Formulation 1

The first formulation seeks to simply maximize the output rotation subject to a constraint on the amount of available material. The required output rotation may be computed given the length of the mirror and the tangential displacement. The problem formulation can be

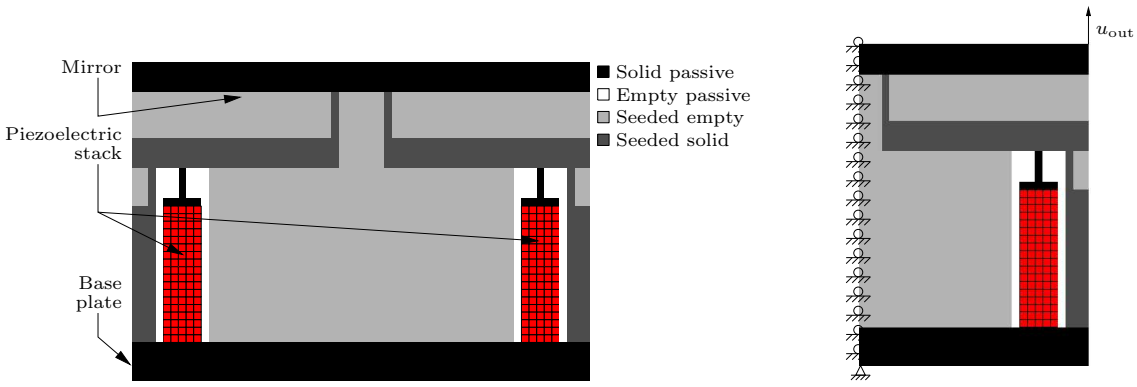

(a) (b)

Figure 5.7: Design domain and problem definition for mirror scanning device: (a) Full initial design, (b) anti-symmetric finite element model.

written as:

$$\min_{\boldsymbol{\rho}} \; f_1(\boldsymbol{\rho}) = -\left(\frac{u_{\text{out}}}{u_{\text{req}}}\right)^2 \tag{5.24}$$

$$\text{such that} \;\; : v(\boldsymbol{\rho}) = \frac{1}{v_\Omega}\left(\sum_{i=1}^{Nel} \rho_i v_i\right) - v^* \leq 0 \tag{5.25}$$

$$: \begin{bmatrix} \boldsymbol{K}_{uu} & \boldsymbol{K}_{u\phi} \\ \boldsymbol{K}_{u\phi}^T & \boldsymbol{K}_{\phi\phi} \end{bmatrix} \begin{Bmatrix} \boldsymbol{U} \\ \boldsymbol{\phi} \end{Bmatrix} = \begin{Bmatrix} \boldsymbol{F} \\ \boldsymbol{Q} \end{Bmatrix} \tag{5.26}$$

$$: \mathbf{0} \leq \boldsymbol{\rho}_{\min} \leq \boldsymbol{\rho} \leq \mathbf{1}. \tag{5.27}$$

The output rotation is maximized by maximizing the output tip displacement u_{out} due to the actuator input. The vertical output displacement is monitored at the top right vertex of the mirror, see Figure 5.7. As mentioned earlier, an output displacement of u_{req}=0.5mm is required to achieve a rotation of 1°. The displacement is normalized with respect to the required value and squared so that the direction of the displacement is not prescribed, and optimization algorithmic scaling issues are avoided.

In this case, the equilibrium equations (5.26) include the piezoelectric terms arising from the piezoelectric actuators, where $\boldsymbol{\phi}$ represents the electric potential and $\boldsymbol{Q}$ the nodal charge. The upper bound on the volume fraction is $v^* = 0.5$. Note that only $\boldsymbol{K}_{uu}$ is a function of the design variables $\boldsymbol{\rho}$ since the piezoelectric elements are considered passive solid elements.

The sensitivity of (5.24) can easily be found, using a process similar to that used to calculate the sensitivity of the output displacement for the force inverter problem, given in (5.23). Using the chain rule:

$$\frac{\partial f_1}{\partial \rho_i} = -2\frac{u_{\text{out}}}{{u_{\text{req}}}^2}\left(\frac{\partial u_{\text{out}}}{\partial \rho_i}\right). \tag{5.28}$$

In this case however, u_{out} is derived from the voltage applied to the electrodes of the piezoelectric actuators, and not directly due to any applied forces.

In the system of equations (5.26), the *unknown* displacement and potential vectors $\boldsymbol{U}$ and $\boldsymbol{\phi}$ respectively, are sought. The vectors $\boldsymbol{F}$ and $\boldsymbol{Q}$ represent not only the applied forces and charges (there are none in this case), but also reactions due to *prescribed* displacement and electric potential boundary conditions. Using static condensation, (5.26) can be rewritten in terms of only the unknown displacements as:

$$\hat{\boldsymbol{K}}\boldsymbol{U} = \hat{\boldsymbol{F}}, \tag{5.29}$$

where the equivalent stiffness matrix is given by

$$\hat{\boldsymbol{K}} = \boldsymbol{K}_{uu} - \boldsymbol{K}_{u\phi}\boldsymbol{K}_{\phi\phi}^{-1}\boldsymbol{K}_{u\phi}^{T}, \tag{5.30}$$

and where the equivalent force vector is given by

$$\hat{\boldsymbol{F}} = \boldsymbol{F} - \boldsymbol{K}_{u\phi}\boldsymbol{K}_{\phi\phi}^{-1}\boldsymbol{Q}. \tag{5.31}$$

This solution strategy, in which electric potentials are condensed from the unknown output vector, also prevents poor scaling which results if displacements and potentials are solved simultaneously [69]. Finally, the unknown potentials can be recovered (if necessary) as

$$\boldsymbol{\phi} = \boldsymbol{K}_{\phi\phi}(\boldsymbol{Q} - \boldsymbol{K}_{u\phi}^{T}\boldsymbol{U}). \tag{5.32}$$

Therefore, instead of solving for the adjoint equation as in (5.22), the solution to the adjoint equation

$$\hat{\boldsymbol{K}}\boldsymbol{\lambda} = \boldsymbol{L}, \tag{5.33}$$

is required, where $\boldsymbol{L}$ is an appropriate adjoint load vector. In terms of elementwise quantities, it can be shown that the sensitivities reduce to

$$\frac{\partial u_{\text{out}}}{\partial \rho_i} = -p(\rho_i)^{p-1}\boldsymbol{\lambda}_i^{T}\boldsymbol{k}_i^{0}\boldsymbol{u}_i, \tag{5.34}$$

where the subscript i once again indicates elemental quantities.

Mirror scanning device: Formulation 2

Using the first formulation large displacements may be obtained at the expense of mechanism stiffness. Such a mechanism may not be robust or stable enough for practical applications. The problem formulation can therefore be modified so that only the required output displacement is attained. In so doing, an additional requirement can be prescribed, i.e. that the structure should be as stiff as possible.

In this second formulation, a mechanism with minimum compliance is sought, subject to a prescribed output rotation being maintained. The required output rotation is, as before, translated to a required tangential displacement of $u_{\text{req}} = 0.5\text{mm}$. The compliance is computed using a point force applied to the output displacement point. Note that since

anti-symmetry is used to model the device, this force in fact simulates a force couple. Additionally, there is no constraint on volume imposed.

The problem can be written in standard form as:

$$\min_{\boldsymbol{\rho}} \; f_2(\boldsymbol{\rho}) = \frac{c}{c_0} \tag{5.35}$$

$$\text{such that} \; : 1 - \left(\frac{u_{\text{out}}}{u_{\text{req}}}\right) \leq 0 \tag{5.36}$$

$$: \hat{\boldsymbol{K}}\boldsymbol{U} = \hat{\boldsymbol{F}} \tag{5.37}$$

$$: \boldsymbol{K}_{uu}\bar{\boldsymbol{U}} = \boldsymbol{L} \tag{5.38}$$

$$: \mathbf{0} \leq \boldsymbol{\rho}_{\min} \leq \boldsymbol{\rho} \leq \mathbf{1}, \tag{5.39}$$

where c_0, the compliance of the initial design, is again introduced to prevent poor scaling of the optimization problem. The compliance is expressed as

$$c = \boldsymbol{L}^T\bar{\boldsymbol{U}} = \bar{\boldsymbol{U}}^T\boldsymbol{K}_{uu}\bar{\boldsymbol{U}}, \tag{5.40}$$

where the displacements $\bar{\boldsymbol{U}}$ are computed by solving the short circuited system given in (5.38), and where $\boldsymbol{L}$ is the adjoint load used to determine u_{out}. The sensitivity of c in this case can easily be shown to be

$$\frac{\partial c}{\partial \rho_i} = -p(\rho_i)^{p-1}\bar{\boldsymbol{u}}_i{}^T\boldsymbol{k}_i^0\bar{\boldsymbol{u}}_i, \tag{5.41}$$

where $\bar{\boldsymbol{u}}_i$ are again appropriate elemental displacements and $\boldsymbol{k}_i^0$ represents stiffness matrix of the solid element.

Mirror scanning device: Formulation 3

In this final problem formulation, the minimum natural frequency of the structure is maximized, again subject to the prescribed tangential displacement of $u_{\text{req}} = 0.5$mm being maintained. Since the 'rotational' stiffness of the structure is of particular interest, anti-symmetric boundary conditions are again employed to model only half of the structure. Finally, as with Formulation 2 there is no constraint imposed on the available volume of material.

The problem can be expressed as:

$$\min_{\boldsymbol{\rho}} \; f_3(\boldsymbol{\rho}) = -\frac{\lambda_{\min}}{\lambda_0} \tag{5.42}$$

$$\text{such that} \; : 1 - \left(\frac{u_{\text{out}}}{u_{\text{req}}}\right) \leq 0 \tag{5.43}$$

$$: \hat{\boldsymbol{K}}\boldsymbol{U} = \hat{\boldsymbol{F}} \tag{5.44}$$

$$: \boldsymbol{K}_{uu}\boldsymbol{\Phi}_j = \lambda_j\boldsymbol{M}\boldsymbol{\Phi}_j, \quad \forall\; j = 1, 2, ..., Ndof \tag{5.45}$$

$$: \mathbf{0} \leq \boldsymbol{\rho}_{\min} \leq \boldsymbol{\rho} \leq \mathbf{1}, \tag{5.46}$$

where λ_j is the j-th short circuited eigenvalue with corresponding eigenvector $\boldsymbol{\Phi}_j$ and $Ndof$ is the total number of degrees of freedom. The eigenvectors are normalised so that

$$\boldsymbol{\Phi}_j^T \boldsymbol{M} \boldsymbol{\Phi}_j = 1, \quad \forall\ j = 1, 2, ..., Ndof. \tag{5.47}$$

Neglecting possible issues with duplicate or multiple eigenvalues (and the resulting non-differentiability issues), the sensitivities of λ_j can be computed using (5.45) as

$$\frac{\partial \boldsymbol{K}_{uu}}{\partial \rho_i}\boldsymbol{\Phi}_j + (\boldsymbol{K}_{uu} - \lambda_j \boldsymbol{M})\frac{\partial \boldsymbol{\Phi}_j}{\partial \rho_i} = \frac{\partial \lambda_j}{\partial \rho_i}\boldsymbol{M}\boldsymbol{\Phi}_j + \lambda_j \frac{\partial \boldsymbol{M}}{\partial \rho_i}\boldsymbol{\Phi}_j. \tag{5.48}$$

By premultiplying by $\boldsymbol{\Phi}_j^T$, making use of the symmetry of $\boldsymbol{K}_{uu}$ and $\boldsymbol{M}$, and substituting (5.45) and (5.47), the sensitivity of λ_j to ρ_i can be shown to be

$$\frac{\partial \lambda_j}{\partial \rho_i} = \boldsymbol{\Phi}_j^T \left(\frac{\partial \boldsymbol{K}_{uu}}{\partial \rho_i} - \lambda_j \frac{\partial \boldsymbol{M}}{\partial \rho_i} \right) \boldsymbol{\Phi}_j. \tag{5.49}$$

This sensitivity can be written with elemental quantities only as

$$\frac{\partial \lambda_j}{\partial \rho_i} = \boldsymbol{\phi}_{j\ i}^T \left(p(\rho_i)^{p-1} \boldsymbol{k}_i^0 - \lambda_j \boldsymbol{m}_i^0 \right) \boldsymbol{\phi}_{j\ i}, \tag{5.50}$$

where $\boldsymbol{\phi}_{j\ i}$ is the elemental component of element i, corresponding to the j^{th} eigenvector, and $\boldsymbol{m}_i^0$ is the mass matrix of the i^{th} solid element.

The modified SIMP material model, for removing localized eigenmodes in low density areas, suggested by Pedersen [104], has been used. Specifically, mass and stiffness terms are interpolated using the following relations:

$$\text{mass:} \quad \boldsymbol{m}_i = \rho_i \boldsymbol{m}_i^0 \quad \text{for } 0 \leq \rho_{\min} \leq \rho_i \leq 1 \tag{5.51}$$

$$\text{stiffness:} \quad \boldsymbol{k}_i = \rho_i^3 \boldsymbol{k}_i^0 \quad \text{for } 0.1 < \rho_i \leq 1 \tag{5.52}$$

$$: \quad \boldsymbol{k}_i = \tfrac{\rho_i}{100} \boldsymbol{k}_i^0 \quad \text{for } 0 \leq \rho_{\min} \leq \rho_i \leq 0.1. \tag{5.53}$$

Reasonable results are achieved without making special provision for multiple eigenvalues. If problems were encountered, the techniques described in [105] could be employed. Alternatively, a bound-formulation could be applied in which the formulation is typically modified as follows

$$\max_{\boldsymbol{\rho}} \ \beta \tag{5.54}$$

$$\text{such that} \ : [\alpha]^j \lambda_j \geq \beta, \quad \forall\ j = 1, 2, ..., Ndof \tag{5.55}$$

$$: \boldsymbol{K}_{uu}\boldsymbol{\Phi}_j = \lambda_j \boldsymbol{M}\boldsymbol{\Phi}_j, \quad \forall\ j = 1, 2, ..., Ndof, \tag{5.56}$$

where for example $\alpha = 0.95$. This additional constraint ensures that consecutive eigenvalues are at least a certain fraction smaller than the previous. It may however, prevent eigenmodes from switching order during the iteration process [4].

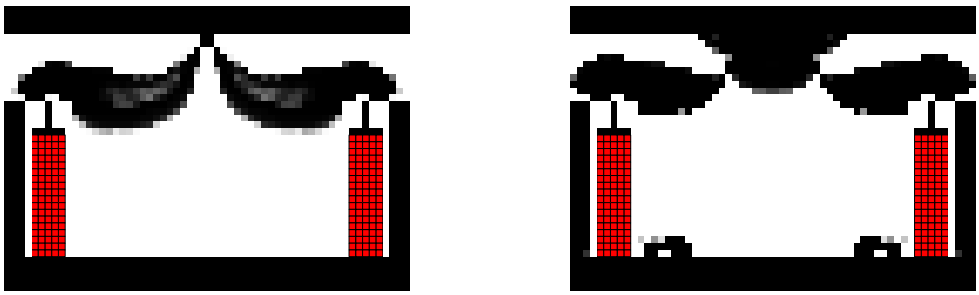

(a) (b)

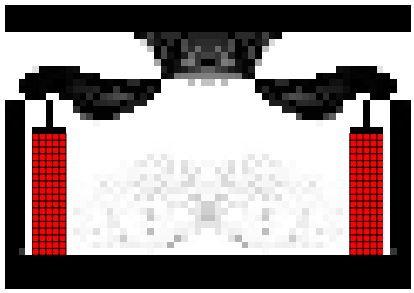

(c)

Figure 5.8: Optimal topologies for: (a) Formulation 1, (b) Formulation 2, (c) Formulation 3. Although anti-symmetry is used in the finite element model, the complete design is shown.

Numerical results

The optimal topologies for the three different problem formulations are depicted in Figure 5.8. Figures 5.8(a), 5.8(b) and 5.8(c) depict the optimal topologies resulting from formulations 1, 2 and 3, respectively. In each case, standard Q4 elements are used in the finite element solution, and the mesh-independency scheme of Sigmund is used to prevent checkerboarding.

As expected, each of the three designs result in similar double-lever mechanisms, although their connection points to the mirror, vary. The designs resulting from formulations 2 and 3 in particular, are very similar. Furthermore, since formulations 2 and 3 do not have a restriction on the amount of available material, superfluous features in the area between the two piezoelectric stacks are obtained, as illustrated in Figures 5.8(b) and 5.8(c).

In each case depicted in Figure 5.8, the optimal design is unacceptible due to the formation of one-node connected hinges. These mechanisms all exploit the unrealistic flexability of the one-node connected hinges to attain the required mobility. After interpretation and post-processing of these designs, it is likely that significantly lower mobility than precicted, will be achieved due to the higher stiffness of realistic hinges. Schemes which prevent their formation (or improve their finite element model) within the topology optimization procedure are therefore sought.

5.5 New schemes to prevent checkerboarding and one-node hinges

In this section, two new schemes to deal with one-node connected hinges and diagonal members are detailed. Results containing diagonal members have been illustrated in Section 5.4.2, when no scheme for checkerboard prevention is employed. Furthermore, in Sections 5.4.3 and 5.4.4 it has been demonstrated that one-node hinges are possible even if Sigmund's mesh independency filter is used to prevent checkerboarding.

In particular, we attempt to show how elements with drilling DOFs may be exploited in formulating schemes to overcome (or improve the modelling of) one-node hinges and diagonal members. The first scheme is based on the NoHinge scheme proposed by Poulsen [15]. Poulsen's scheme is modified to incorporate a measure of rotation so that distinction can be made between a hinge undergoing rotation, and a diagonal member in tension.

The second scheme attempts to perform the 'post-processing step' of interpreting the final topology automatically during the optimization process. Since a one-node hinge is often interpreted as a thin beam, it seems reasonable to directly use beam finite elements in areas where one-node hinges or diagonal members occur.

5.5.1 Scheme I: A modified scheme based on NoHinge

The rotations at one-node hinges are usually large, and since rotations are computed at each node associated with Q4X elements, they present a natural measure to detect excessive rotations at suspect nodes.

However, since the rotations (and displacements) calculated at nodes surrounded by empty elements can be large, but are considered irrelevant, a density function is necessary to eliminate rotations and displacements calculated at these nodes. In the current scheme, the NoHinge method proposed by Poulsen [15] is used as an appropriate density function. Combining the scheme of Poulsen with a measure of rotation, results in a scheme which effectively detects and prevents checkerboarding and, in particular, one-node connected hinges. However, the new scheme is also capable of distinguishing between a one-node hinge and a *diagonal structural member* subjected to purely axial loads

Poulsen developed a local function h that efficiently detects one-node connected hinges. The scheme is a function of (the densities of) the four elements surrounding each interior node in the finite element mesh. His scheme makes use of the fact that a one-node hinge is not *quasi-monotonic* in density around a node.

Each local (non-negative) h function is simply summed, resulting in a global measure H which is added to the topology optimization problem as a single additional constraint. This scheme was shown by Poulsen to eliminate both one-node connected hinges and checkerboarding.

The local (density) function, h, which detects one-node connected hinges is defined as

$$h(a,b,c,d) = m(a,b,d) \cdot m(a,c,d) \cdot m(b,a,c) \cdot m(m,d,c), \tag{5.57}$$

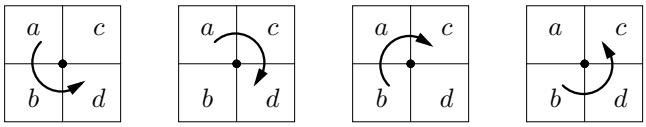

Figure 5.9: Four paths around node to check for quasi-monotonicity.

where a, b, c, d are the material density values in the elements surrounding the node, as indicated in Figure 5.9, and m is defined as

$$m(a, b, c) = |b - a| + |c - b| - |c - a|. \tag{5.58}$$

It is propsed here to modify this local function h, and to define a new funtion, denoted h', as follows

$$h'_{ij} = |\psi_{ij}| h_{ij}, \tag{5.59}$$

where i and j are pointers to the location of an interior node at row i and column j in the finite element mesh, and ψ_{ij} is the rotation at interior node i, j. For implementation in a gradient-based optimization environment, the absolute value function is replaced with a continuous approximation. For example, $|x|$ would be replaced by the approximate function A, where

$$A(x) = \sqrt{x^2 + \epsilon^2} - \epsilon, \tag{5.60}$$

where ϵ is an appropriately small number. The modified descriptor function H' based on the modified local function h' is therefore defined as

$$H'(\boldsymbol{\rho}) = \sum_{j=1}^{k-1} \sum_{i=1}^{l-1} h'(\rho_{i\ j}, \rho_{i+1\ j}, \rho_{i\ j+1}, \rho_{i+1\ j+1}, \psi_{ij}), \tag{5.61}$$

where k is the number for rows of elements and l is the number of element columns in the regular finite element mesh. As in the scheme of Poulsen, this modified descriptor function is added to the original topology optimization function as a single additional constraint function:

$$H'(\boldsymbol{\rho}) - \delta \leq 0, \tag{5.62}$$

where δ is a prescribed tolerance. Note that in applications where engineering materials are used, the rotations may be relatively small, and may therefore need to be scaled.

In (5.59), the sensitivity of each h_{ij} is given by Poulsen [15] and the sensitivities of each ψ_{ij} can be found using the adjoint method. A significant drawback of this method is therefore the additional computational effort required for sensitivity calculations. For each iteration (if no active set type strategy is used to minimize the computational cost) there are as many additional adjoint loads required as internal nodes.

5.5.2 Scheme II: A new scheme to improve checkerboard, one-node hinge and diagonal member modelling

In this section, the second of the two new schemes is presented. Instead of explicitly preventing the formation of checkerboard, one-node hinge and diagonal member layouts as before,

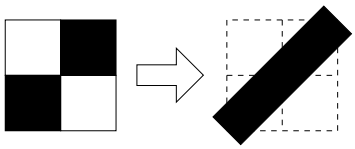

Figure 5.10: Post-processed interpretation of a 2×2 hinge.

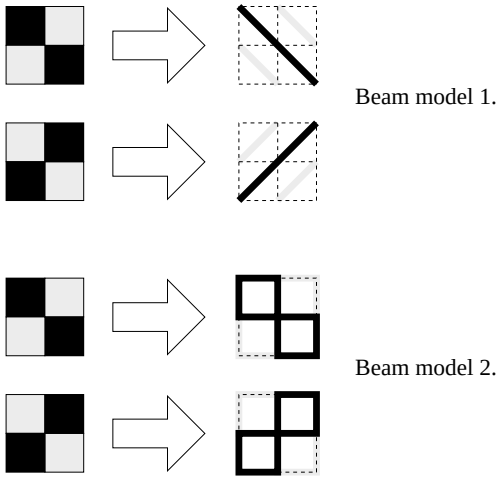

Figure 5.11: Two different beam models of a hinge.

this scheme aims at improving the finite element model of these layouts by replacing selected elements with a more representative beam model.

Traditional Q4 elements possess only translational DOFs and therefore combining beam elements and Q4 elements in a single model often calls for *ad hoc* modelling 'tricks', or the use of MPC's. Planar elements with drilling DOFs however, allow for the direct connection of beam and plane elements.

The use of beam elements in conjunction with elements with drilling DOFs, to improve the modelling of, in particular one-node hinges, is explored. We argue that instead of eliminating these layouts, an alternative is to use an improved finite element model.

The idea is therefore to replace undesirable 2-D planar element layouts with an equivalent beam model, which represents a reasonable post-processed or interpreted model of the original 2-D element layout. A reasonable interpretation of a one-node hinge is depicted in Figure 5.10. Note that the interpreted geometry preserves the volume of material in the original layout.

Herein however two possible beam models for representation of a one-node hinge are evaluated, as depicted in Figure 5.11. The first model replaces the planar elements with diagonal beams as suggested in Figure 5.10. In a second model, the planar elements are replaced with a box-like beam structure, similar to the 2-D element's layout. Although both are valid interpretations of a one-node hinge, the most natural and easiest to manufacture is the diagonal beam (beam model 1 in Figure 5.11).

The steps involved in the proposed strategy to automatically detect and replace problematic

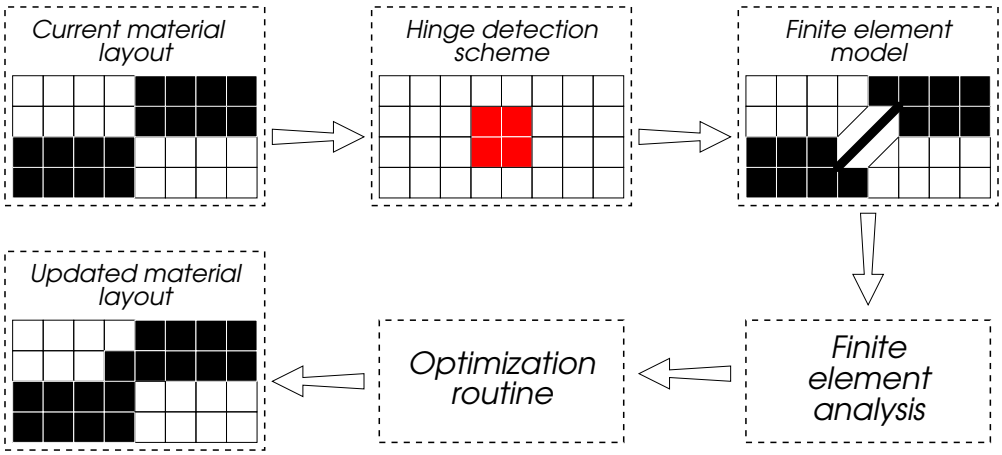

Figure 5.12: Beam replacement scheme.

planar elements by beam elements is schematically depicted in Figure 5.12. Firstly, it is assumed that the vector of design variables describing the material layout are arranged in a fixed grid, as is usually the case in topology optimization procedures. Next, possible hinges or diagonal members are identified, based solely on the material distribution. Then, depending on whether or not unsuitable material distributions are detected, selected planar elements are removed from the finite element model, and replaced with an equivalent beam model. This assembly of beam and planar finite elements is analysed using the finite element method, and the results passed to the optimization procedure. Finally, the optimization procedure makes a preciction of an improved material layout, and the process is repeated. If an updated design is predicted with no unsuitable material layouts, as is the case illustrated in Figure 5.12, planar elements are not replaced by beam elements, making the process of element replacement completely reversable.

The suggested process by which 2-D planar elements are replaced by their equivalent beam model, is similar to the way in which multiple materials have been used in topology optimization [106]. Instead of a second density measure however, a *function* which returns 1 if the beam model is to be used, and 0 if the planar element is appropriate, is used. This scalar function is denoted $\mathcal{H}$, with $0 \leq \mathcal{H} \leq 1$, and essentially indicates whether an element forms part of a one-node hinge or not. The elemental stiffness matrix, denoted $\boldsymbol{k}^e$, is accordingly calculated as

$$\boldsymbol{k}^e_{i,j} = \rho^p_{i,j}(\mathcal{H}_{i,j}\boldsymbol{k}^0_{\text{frame}} + (1 - \mathcal{H}_{i,j})\boldsymbol{k}^0_{\text{Q4X}}), \quad i = 1, 2, \ldots, N, \ j = 1, 2, \ldots, M, \tag{5.63}$$

where the subscript i, j denotes the i^{th} row and j^{th} column in a grid of elements with N rows and M columns. The density associated with the element is denoted $\rho_{i,j}$, while p is a penalty parameter used in the SIMP method. The beam and the 2-D planar element's stiffness matrices are denoted $\boldsymbol{k}^0_{\text{frame}}$ and $\boldsymbol{k}^0_{\text{Q4X}}$ respectively.

As a first step towards calculating $\mathcal{H}_{i,j}$, a local function to detect a one-node hinge at each interior node in the mesh is required. Our local function shall be denoted $\tilde{h}$ and uses the four orthogonal basis vectors $\boldsymbol{\phi}^k$, $k = 1, 2, 3, 4$, depicted in Figure 5.13 see [98]. The basis

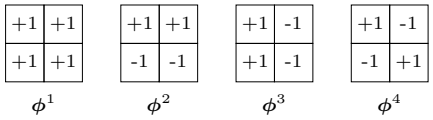

Figure 5.13: Orthogonal basis vectors.

vectors are given explicitly as

$$\begin{array}{rcrrrr} \boldsymbol{\phi}^1 & = & [1 & 1 & 1 & 1] \\ \boldsymbol{\phi}^2 & = & [1 & -1 & 1 & -1] \\ \boldsymbol{\phi}^3 & = & [1 & 1 & -1 & -1] \\ \boldsymbol{\phi}^4 & = & [1 & -1 & -1 & 1] \end{array} \tag{5.64}$$

where $\boldsymbol{\phi}^4$ represents the basis for a one-node hinge. A vector of element densities in a given patch of four elements at interior nodes i, j, is given by

$$\boldsymbol{v}_{i,j} = [\rho_{i,j} \quad \rho_{i+1,j} \quad \rho_{i,j+1} \quad \rho_{i+1,j+1}], \tag{5.65}$$

where the relationship between the elements and nodes is depicted in Figure 5.14. Now, the four components of the density vector $\boldsymbol{v}_{i,j}$ in each of the basis vector directions is given by the dot product of $\boldsymbol{v}_{i,j}$ with $\boldsymbol{\phi}^k$, $k = 1, 2, 3, 4$. In order to ensure only positive quantities in the calculation of the local $\tilde{h}$ function, the dot products are squared and the result denoted ζ^k, $k = 1, 2, 3, 4$:

$$\zeta^k_{i,j} = (\boldsymbol{v}_{i,j} \cdot \boldsymbol{\phi}^k)^2, \quad k = 1, 2, 3, 4. \tag{5.66}$$

The local scalar function to identify a one-node hinge for the four elements around interior node i, j is finally introduced as

$$\tilde{h}_{i,j} = \left(\frac{\zeta^4_{i,j}}{\zeta^1_{i,j}}\right)\left(1 - \frac{\zeta^2_{i,j}}{\zeta^1_{i,j}}\right)\left(1 - \frac{\zeta^3_{i,j}}{\zeta^1_{i,j}}\right). \tag{5.67}$$

It is clear from this function that $0 \leq \tilde{h}_{i,j} \leq 1$. Poulsen [15] defined a similar function (NoHinge) using the nonmonotonic behaviour of a one-node hinge around a given node, see equation (5.57). Unfortunately his function decreases sharply as the density of the elements decrease. Our new function effectively detects one-node hinges even when made up of elements with intermediate density. Incidentally, Rozvany [99] independently suggested a number of different functions to overcome the problems associated with Poulsen's function.

As depicted in Figure 5.14, an arbitrary interior element i, j can be involved in four different local $\tilde{h}$ functions, any of which could be a potential one-node hinge. A vector of local functions to which element i, j contributes, is defined as

$$\boldsymbol{H}_{i,j} = \left[\tilde{h}_{i-1,j-1} \quad \tilde{h}_{i,j-1} \quad \tilde{h}_{i-1,j} \quad \tilde{h}_{i,j}\right]. \tag{5.68}$$

Special attention is now required for boundary elements. For example, considering an element in the 1st row and 1st column, the functions $\tilde{h}_{0,0}$, $\tilde{h}_{1,0}$ and $\tilde{h}_{0,1}$ do not exist. Each local $\tilde{h}$ in (5.68) is therefore defined by

$$\tilde{h}_{k,l} = \begin{cases} \tilde{h}_{k,l} & \text{if } h_{k,l} \text{ exists, and} \\ \emptyset & \text{otherwise} \end{cases} \tag{5.69}$$

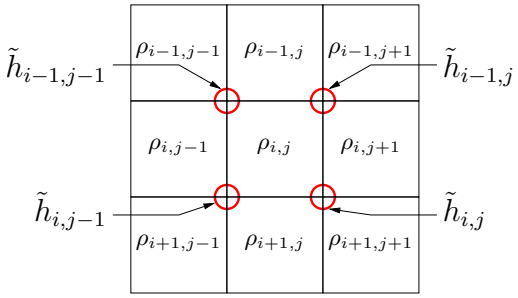

Figure 5.14: Patch of nine elements around element i, j.

where $\emptyset$ denotes an empty set. So, for example, $\boldsymbol{H}_{1,1} = \begin{bmatrix} \emptyset & \emptyset & \emptyset & \tilde{h}_{1,1} \end{bmatrix} = \begin{bmatrix} \tilde{h}_{1,1} \end{bmatrix}$. The measure quantifying whether element i, j takes part in a one-node hinge or not, may now simply be defined as the maximum term in the $\boldsymbol{H}_{i,j}$ vector (5.68).

$$\mathcal{H}_{i,j} = ||\boldsymbol{H}_{i,j}||_{\infty}. \tag{5.70}$$

Note that $\mathcal{H}_{i,j}$ is a function of only the four element densities defining the maximum local $\tilde{h}$ function.

As illustrated in Figure 5.11, beam model 1 is dependant on the orientation of the element densities. Therefore, once each element's $\mathcal{H}_{i,j}$ has been calculated, the orientation of the beam model needs to be determined. To decide which of the two diagonal beams is more appropriate, the sign of $(\boldsymbol{v}_{i,j} \cdot \boldsymbol{\phi}^4)$ can be used. Beam model 2 is not dependant on the arrangement of the elements.

A possible complication in an optimization environment is the discontinuous nature of $\mathcal{H}_{i,j}$. In order to alleviate this discontinuity, the infinity norm in (5.70) is approximated by a continuous function. A p-norm is not appropriate since values of $\mathcal{H} > 1$ should be avoided, and the p-norm converges to the infinity norm from above for $p \geq 1$. The function

$$\hat{\mathcal{H}}_{i,j} = \frac{(||\boldsymbol{H}_{i,j}||_2)^2}{||\boldsymbol{H}_{i,j}||_1}, \tag{5.71}$$

satisfies our requirements. $\hat{\mathcal{H}}_{i,j}$, is a function of all 9 elements depicted in Figure 5.14. For this reason the orientation of a diagonal beam model (beam model 1 in Figure 5.11) cannot easily be determined. Therefore, only the box-like model (beam model 2 in Figure 5.11) will be used for this measure. Finally, in order to prevent $||\boldsymbol{H}_{i,j}||_1$ from becoming zero, a small perturbation on the $\tilde{h}$ functions is necessary, therefore $\epsilon \ll 1$ is added to (5.67).

5.6 Numerical examples and applications

In this section, the merits of the two newly introduced scheme are evaluated using the test problems introducted in Section 5.4.

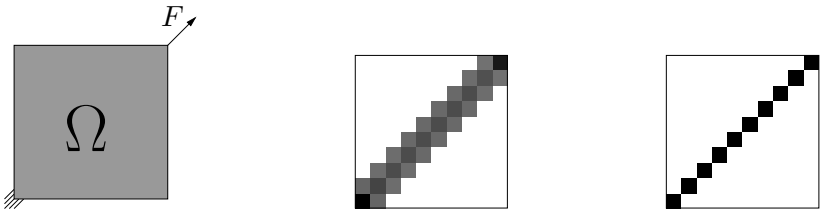

(a) (b) (c)

Figure 5.15: Illustration of the effect of the proposed scheme to overcome one-node hinges: (a) The design problem, (b) optimal design using the scheme of Poulsen, (c) optimal design using the proposed scheme.

5.6.1 Application of Scheme I

A potential drawback of the original scheme of Poulsen is the possibility of undue penalization of an optimal design. An example of this situation is depicted in Figure 5.15, where the square design domain is discretized into a 10×10 mesh, with loads and constraints as depicted, and a prescribed volume fraction of $v^* = 0.1$. Although this design problem is probably not practically significant, a similar situation could occur locally in topology optimization problems, especially if a coarse discretization is used.

Figure 5.15(a) depicts the design problem. Figure 5.15(b) depicts the optimal design found using the scheme of Poulsen, in which one-node hinges are prevented, and unduly penalized. Figure 5.15(c) depicts the optimal design using the modified scheme proposed herein (Scheme I), in which the local functions h' are expressed in terms of the absolute value of rotation at the applicable node. In so-doing only those one-node hinges that actually act as hinges (viz. associated with large rotations) are avoided. For the simple problem depicted in Figure 5.15, zero rotations arise due to the applied load. Therefore no penalization is required or enforced.

For this problem the optimal topology using the original scheme of Poulsen has to violate either the volume constraint or the additional constraint imposed by NoHinge. For the modified scheme, since zero rotation is induced along the diagonal, both the volume constraint and the constraint on H' can be satisfied exactly.

Figure 5.16 depicts the application of the original scheme of Poulsen [15] and our modified scheme suggested herein to the force inverter compliant mechanism with a 48×48 mesh and volume constraint $v^* = 0.3$. A reference solution was presented in Figure 5.6 illustrating the formation of one-node connected hinges. The stronger penalization of one-node hinges with large rotations (enlarged view Figure 5.16(b)) which is induced with the modified method, forces the density distribution around the hinge towards relatively large areas with intermediate densities, as compared to the original scheme of Poulsen (Figure 5.16(a)). Having said that, both solutions can be accommodated in a post-processing step and are quite similar.

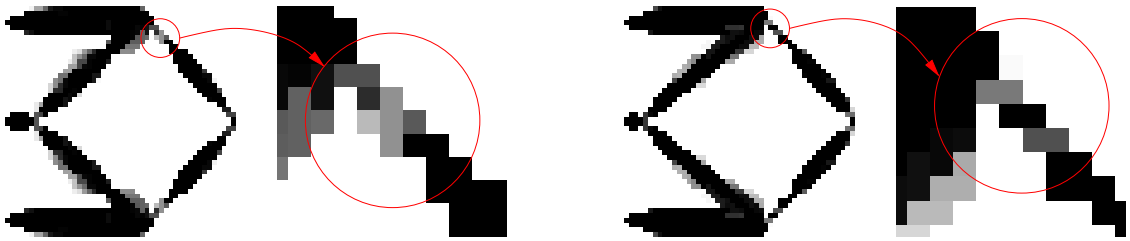

(a) (b) (c) (d)

Figure 5.16: Application of different filters to the force inverter: (a) optimal design using new method, (b) enlarged view of potential hinge, (c) optimal design using original method of Poulsen [15], (d) enlarged view of potential hinge.

5.6.2 Application of Scheme II

In this section the second scheme (Scheme II) is firstly validated on a number of benchmark problems to determine the modelling accuracy. Thereafter, the scheme is used in a topology optimization infrastructure to solve the popular MBB beam problem, and finally the compliant mirror scanning device.

Numerical accuracy benchmark problems

In an attempt to determine the applicability of this new method, some accuracy benchmarking evaluations of the alternative finite element models are conducted. In the tables to follow, results for both measures $\mathcal{H}$ (calculated in (5.70)) and $\hat{\mathcal{H}}$ (from (5.71)) are presented. 'Beam 1' refers to the diagonal beam model, denoted beam model 1 in Figure 5.11. 'Beam 2' refers to the box-like beam model, labeled beam model 2 in Figure 5.11. Considering the box-like beam representation (Beam 2), the ratio of horizontal to vertical beam element heights is equal to the aspect ratio of the 2-D element. In the presentation of the results, Q4 is used to denote the results employing traditional planar elements *without* drilling DOFs, whereas Q4X identifies results for planar elements *with* drilling DOFs. Furthermore, V refers to the volume of the beam representation and V^0 to the volume of the original 2-D element. To determine the sensitivity of the scheme to beam thickness, beam representations with two different volumes, namely $V = V^0$ and $V = 2V^0$, will be evaluated.

The first test problem, used to benchmark the modelling accuracy, is depicted in Figure 5.17(a) with the applied load as shown. It represents a square domain modelled with $(n+1)\times(n+1)$ square elements, and an $n\times n$ diagonal member. The black elements in the figure are solid ($\rho = 1$) while all other elements are void and have a density of $\rho = \rho_{\min} = 10^{-3}$. A penalty parameter of $p = 3$ in (5.63), is used. The displacements calculated with the various elements are normalized with respect to a finite element analysis, using a refined mesh, of the post-processed geometry shown in Figure 5.17(a).

Table 5.1 presents the normalized tip displacements of a diagonal member subject to the load in Figure 5.17(a), using various elements, and for different mesh refinements. For this problem the model employing diagonal beam elements (Beam 1) is relatively accurate, even

	n=2	n=4	n=8	n=16
$\mathcal{H}$, Beam1, $V{=}V^0$	1.6265	1.3203	1.1602	1.0811
$\mathcal{H}$, Beam2, $V{=}V^0$	1.9217	2.9930	3.5756	3.8807
$\mathcal{H}$, Beam2, $V{=}2V^0$	0.30913	0.44165	0.51366	0.55126
$\hat{\mathcal{H}}$, Beam2, $V{=}V^0$	1.8674	2.9192	3.5131	3.8309
$\hat{\mathcal{H}}$, Beam2, $V{=}2V^0$	0.32815	0.46079	0.52669	0.55927
Q4X	5.9252	3.4241	2.2835	1.9220
Q4	$8.4119{\times}10^6$	$2.2008{\times}10^6$	$4.2153{\times}10^5$	$7.0902{\times}10^4$

Table 5.1: Normalised tip displacement of a diagonal member.

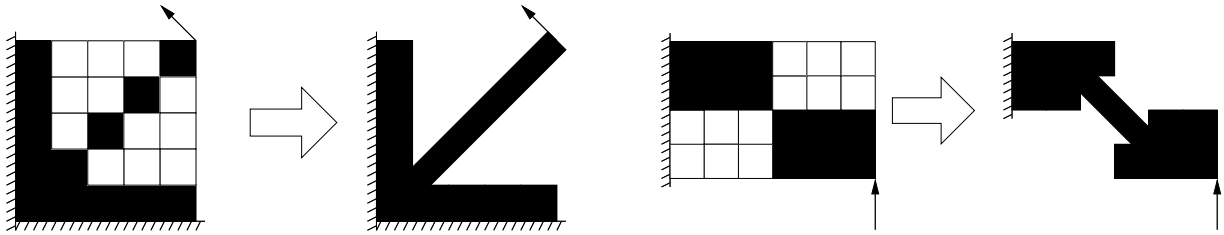

(a) (b)

Figure 5.17: Modelling accuracy benchmark problems: (a) Diagonal member, (b) one-node hinge.

for the extreme case of a diagonal member with only two elements ($n = 2$). The results indicate that the box beam section with the same volume as the original element ($V = V^0$) over-predicts the displacement, while a box section with twice the original volume ($V = 2V^0$) is too stiff. Similar results for both functions $\mathcal{H}$ and $\hat{\mathcal{H}}$ employing the box-like beam model (Beam 2) are calculated. Finally, the diagonal member modeled with Q4X elements, is not sufficiently accurate to approximate the interpreted geometry. Q4 elements, possess no stiffness in this configuration, with only the void elements preventing the singularity.

Table 5.2 presents the results of modelling the one-node hinge depicted in Figure 5.17(b), for the load shown. The first column presents the normalised vertical displacement of the node

	$n_{\text{bisect}}{=}0$	$n_{\text{bisect}}{=}1$	$n_{\text{bisect}}{=}2$	$n_{\text{bisect}}{=}3$
$\mathcal{H}$, Beam1, $V{=}V^0$	2.6086	2.3400	2.2747	2.2719
$\mathcal{H}$, Beam2, $V{=}V^0$	2.3251	2.4760	2.5342	2.5440
$\mathcal{H}$, Beam2, $V{=}2V^0$	0.43379	0.41329	0.40839	0.40584
$\hat{\mathcal{H}}$, Beam2, $V{=}V^0$	2.3177	2.4684	2.5263	2.5362
$\hat{\mathcal{H}}$, Beam2, $V{=}2V^0$	0.43525	0.41499	0.41011	0.40756
Q4X	2.9994	2.7231	2.7123	2.7202
Q4	$3.5400{\times}10^6$	$1.0266{\times}10^6$	$2.6914{\times}10^5$	$6.8014{\times}10^4$

Table 5.2: Normalised displacement of a one-node hinge.

	Formulation 1	Formulation 2	Formulation 3
Q4	3.7718×10^{-3}	4.1903×10^{-4}	4.1904×10^{-4}
Q4X	1.9901×10^{-4}	2.6926×10^{-4}	2.7286×10^{-4}
$\hat{\mathcal{H}}$, Beam2, $V{=}2V^0$	5.1435×10^{-5}	1.1554×10^{-4}	1.1136×10^{-4}

Table 5.3: Output displacement of optimal mirror mechanisms.

to which the load is applied, using the discretization shown in the figure. Results are then presented for the number of mesh bisections of the original mesh given by n_{bisect}. Results are again normalized with respect to a detailed finite element analysis of the post-processed geometry depicted in Figure 5.17(b).

For this problem, the model employing diagonal beams (Beam 1) is relatively inaccurate when compared to the previous test problem. Again the model employing the box-like beam model over-predicts the displacement if the volume of the original 2-D element is conserved and is too stiff if the beam representation's volume is doubled. In this case, the model simply using elements with drilling DOFs (Q4X) predicts a similar displacement to the model containing the diagonal beam element. Again, the Q4 elements possess very little stiffness for this bending-dominated load.

Finally, the new scheme is used to re-evaluate the optimal topologies (of the mirror scanning device) presented in Section 5.4.4. For brevity, only the results of the box-like beam model with twice the 2-D element's volume is presented in Table 5.3. The Q4X elements, which have been shown in the benchmark problems to under-predict the stiffness of the interpreted design, produce substantially lower output displacements than the original model with Q4 elements. This is especially true for the design resulting from optimization Formulation 1. Notably, the beam model employed here severely penalizes the working of the mechanism, containing one-node hinges and therefore seems a promising method to penalise the formation of one-node hinges in topology optimization results.

Topology optimization implementation

The developed scheme is now used in a topology optimization infrastructure. The first benchmark topology optimization test problem is the well known MBB beam, detailed in Section 5.4.1. Exploiting the symmetry of the problem, only half the beam is modelled.

Figure 5.18(a) depicts the results using Q4 elements with no filters or other devices. The checkerboarding problem is clearly illustrated. In Figure 5.18(b) the checkerboard layout is eliminated using the filter of Sigmund [100] with a filter radius of 1.2 element lengths. Figures 5.18(c) to 5.18(e) show the results using the proposed scheme with various beam element models. From these figures, it is apparent that the beam models are sufficiently flexible to alleviate checkerboard layouts. Moreover, the results achieved using the new scheme are also far less defuse than results computed using filtering.

Finally, the new scheme is applied in the design of the mirror mechanism discussed in Section 5.4.4. The optimization is performed for the second problem formulation (Formulation 2 in Section 5.4.4). The optimal topology in this case, depicted in Figure 5.19, closely resem-

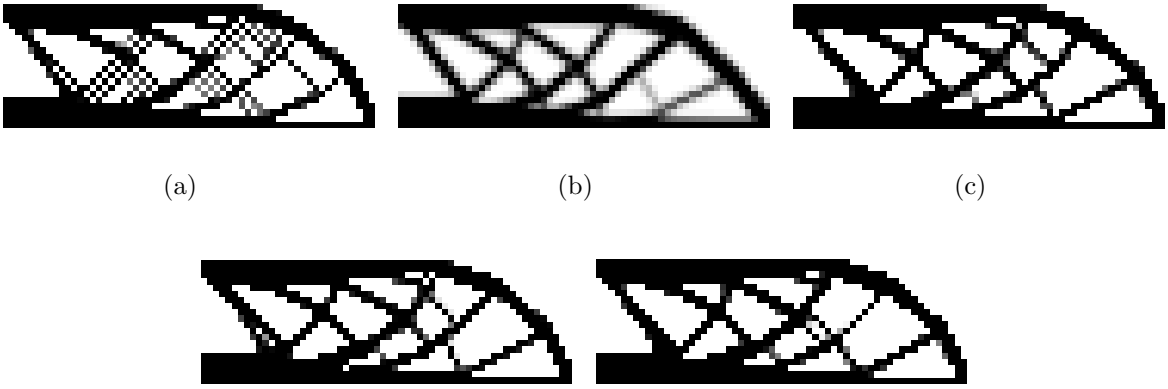

Figure 5.18: MBB beam solutions using: (a) Q4 elements, (b) Q4 with filter of Sigmund, (c) $\hat{\mathcal{H}}$, Beam2, $V{=}V^0$, (d) $\hat{\mathcal{H}}$, Beam2, $V{=}2V^0$, (e) $\hat{\mathcal{H}}$, Beam1, $V{=}V^0$.

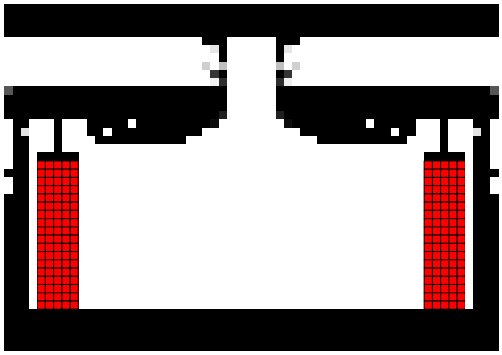

Figure 5.19: Mirror mechanism design using new scheme, $\hat{\mathcal{H}}$, Beam2, $V{=}2V^0$.

bles the starting design, and is quite different from the results achieved with Q4 elements and standard filtering techniques, see Figure 5.8(b). Notably, one-node hinges have been sufficiently 'stiffened' such that their existence is practically infeasible.

Upon further investigation, no feasible discrete (0-1) solution has been found for this specific discretization, despite extensive numerical experimentation. That is to say, the required displacement can only be achieved by inclusion of one-node connected hinges or by the introduction of elements with intermediate desities.

Therefore the prediction from the initial topology optimization study, suggesting that a 0.5mm displacement is attainable with 1mm thick hinges is misleading since the unrealistic flexiblity of one-node hinges are exploited to achieve this displacement.

The optimal design using the scheme suggested herein (depicted in Figure 5.19), rather compromises on the hinge densities to achieve the required flexibility, indicating that thinner hinges are required. The suggestion is therefore that a finer mesh is required in order to allow for thinner hinges.

5.6.3 Discussion of results

Our two proposed schemes have been applied to solve a number of topology optimization problems. The first scheme, Scheme I, based on the NoHinge method of Poulsen, was shown to clearly distinguish between diagonal members subjected to axial loads and hinges undergoing rotation. However, when applied to practical topology optimization problems, such as the force inverter problem, results closely resemble those of the NoHinge scheme. A significant drawback of our method is the additional adjoint loads required for the constraint sensitivity calculations.

Considering the second scheme, Scheme II, the results of the benchmark accuracy evaluations emphasize that the direct connection between a beam element to a *single* node of a planar element (with drilling DOFs) should be avoided since moments cannot accurately be transfered. Such a situation occurs in the case of the diagonal beam model (denoted Beam model 1 in Figure 5.11), and the unpredictable behaviour is illustrated by the difference in accuracy of the results presented in Tables 5.1 and 5.2.

A preferable situation occurs in the case of the box-like structure (Beam model 2 in Figure 5.11) since this structure allows for the transmission of moments from the beam representation to the 2-D elements predictably. However this beam representation does not accurately predict the displacement of the favoured interpretation of a hinge depicted in Figure 5.10. It is worthwhile noting however, that the accuracy of the box-like beam model would be considerably better if a comparison with respect to a box-like post-processed design were carried out. However, the manufacture of such a structure would be more complex than than the diagonal beam-type interpretation. Some work is therefore still required to develop an improved beam model which accurately predicts the response of the post-processed one-node hinge (depicted in Figure 5.10).

Nevertheless this scheme remains a promising alternative to filtering methods. It is demonstrated that this scheme effectively 'softens' checkerboard layouts preventing their formation. Furthermore, one-node connected hinges are shown to be sufficiently 'stiffened' such that their formation is infeasible in compliant mechanism design problems. An additional salient feature of this scheme applied in a topology optimization environment, is that it does not require any additional constraints and therefore optimality criteria methods can be used to solve simple minimum compliance problems. What is more, unlike topology optimization performed with a ground structure of beam elements, the majority of the resulting design using this method, is continuous.

5.7 Conclusions

In this chapter the benefits of using membrane finite elements with drilling degrees of freedom (DOFs) in topology optimization applications has been demonstrated. These elements increase numerical accuracy and analysis capability, while not excessively increasing the computational effort.

Although a detailed study of the checkerboarding instability is carried out in Chapter 7, it is shown here, via numerical experiments, that employing these elements significantly reduces

the amount of checkerboarding obtained in optimal topologies.

In addition, elements with drilling DOFs present a natural way of detecting and/or penalizing one-node connected hinges and diagonal members. Alternatively, they can be used to improve on the numerical modelling of one-node hinges and diagonal members. Two new schemes to treat these material layouts have been suggested, exploiting drilling DOFs.

The first scheme is based on NoHinge, a scheme originally proposed by Poulsen [15]. Our modified scheme however, uses the rotations computed at internal nodes to distinguish between material layouts which are behaving as a hinge (rotating) and a diagonal structural member subjected to axial loads. This scheme however, requires a somewhat numerically expensive constraint sensitivity computation, and its practical application is therefore somewhat limited.

A second scheme to model a one-node hinge, such that the computed response is similar to a reasonable interpretation of the material layout, is presented. A function has been developed which indicates whether or not an element takes part in a layout with unsuitable numerical representation. Thereafter, selected elements are replaced by an equivalent beam model which is numerically better behaved. Since this process is dictated by the material distribution at each iteration, it is reversible so that planar elements which have formerly been replaced by beam elements, may again become planar elements and *vice versa*. Using this new method, it has been demonstrated that it is relatively easy to stiffen a one-node hinge in compliant mechanism design (or soften checkerboard layouts), thereby preventing their formation.

Finally, topology optimization has been employed in the design of a mirror scanning device, employing three different problem formulations. The first seeks to simply maximize the output rotation, while the other two maximize some measure of stiffness subject to a required output rotation being maintained. Each of the resulting optimal topologies, computed using standard Q4 elements and filtering techniques, contain a number one-node hinges and are therefore not acceptable. The most promising scheme (Scheme II) has therefore finally been applied in the design of the device. The design employing our new scheme effectively penalized one-node hinges in critical areas, thereby preventing their formation.

Chapter 6

Effect of element formulation on membrane, plate and shell topology optimization problems

6.1 Summary

In this chapter the effects of membrane, plate and flat shell finite element formulations on optimal topologies are investigated. Two membrane components are considered. The first is a standard 4-node bilinear quadrilateral with only two translational degrees of freedom per node. The other is a 4-node element with three degrees of freedom per node, which properly accounts for in-plane (drilling) rotations. Plate elements selected for evaluation include Discrete Kirchhoff Quadrilateral (DKQ) elements as well as two Mindlin-Reissner based elements, one employing Selective Reduced Integration (SRI), and the other an Assumed Natural Strain (ANS) formulation, to overcome transverse shear locking. The flat shell elements studied, consist of an assemblage of these membrane and plate components.

Since DKQ elements are shear rigid, they are only well suited to thin plate problems. Mindlin-Reissner based elements, on the other hand, are shear flexible and may therefore be used in the analysis of thin to moderately thick plate problems. For popular benchmark topology optimization plate problems, both Mindlin-Reissner elements are shown to recover thin plate results computed using DKQ elements. However, a new benchmark problem is introduced to illustrate the deficiencies of Mindlin-Reissner elements, employing SRI on transverse shear terms, without hourglass control. On the other hand, elements with an ANS formulation are shown to be stable and robust.

For membrane and shell problems, elements which properly account for in-plane rotations are shown to be insensitive to the penalty parameter which enforces the relationship between in-plane rotations and displacements. Conversely, it is illustrated that a simple, but *ad hoc*, treatment of drilling degrees of freedom for standard bilinear membrane elements is sensitive to the introduced parameter for a number of popular shell problems. A benchmark problem which further highlights this sensitivity, in the form of a pretwisted beam, is also introduced.

6.2 Introduction

Due to the competitive nature of industry, designers are increasingly expected to produce optimal, or near optimal, designs. What is more, they are expected to do so rapidly to ensure that superior products are launched timeously. This, in part, explains the recent significant attention that structural optimization has received from research institutes and industry alike.

The advent of inexpensive computers, capable of performing complex calculations extremely quickly, has made it feasible to optimize even complex nonlinear structures with reasonable discretization. Structural optimization could therefore in future (and of course within reason), largely automate the design process and deliver optimal solutions, making what is now mostly a trial-and-error design improvement strategy redundant.

Sizing and shape optimization rely on the engineer or designer's judgment and experience to select an acceptably good starting design, since in both cases the topology is fixed throughout. Topology optimization is seen as particularly powerful since it is capable of exploring different topologies during the optimization process. Topology optimization can therefore generate optimal, sometimes unintuitive designs while simultaneously generating the optimal shape.

Topology optimization has been receiving unprecedented attention of late. This is particularly evident at specialized structural and multidisciplinary optimization meetings, such as the recent WCSMO6 congress held in Rio de Janeiro, Brazil, where topology optimization drew significant attention. All this research effort has led to many advances in topology optimization, especially in the types of problems which can now be addressed.

The recent revival of interest is largely credited the early paper of Bendsøe and Kikuchi [107] who employed homogenization techniques to perform generalized shape optimization. Even before this, a pivotal role was played by the problem of variable thickness plate design, see for example the original work of Cheng and Olhoff [108].

In this work the popular SIMP (Simple Isotropic Material with Penalization) material parameterization is employed in order to demonstrate the effect of element selection in topology optimization. Bendsøe [109] is largely credited for the introduction of the SIMP material model, which was independently derived by Zhou and Rozvany [110] and Rozvany *et al.* [111].

Special attention is paid to plate and shell problems in this chapter. It is therefore appropriate to give some background on topology optimization of plate and shell problems at this point. There has been a plethora of work in this field, so this is by no means an exhaustive review of all work done. A more thorough review can be found in, for example the book of Bendsøe and Sigmund [4].

Tenek and Hagiwara [112] employed homogenization techniques to generate optimal isotropic single layer and multilayer anisotropic plate topologies. They minimize the structural strain energy subject to a volume constraint, employing sequential linear programming to solve the optimization problem. The finite elements used in their work are based on Mindlin-Reissner plate theory, and are four noded bilinear quadrilateral elements with only 5 degrees of freedom (DOFs) per node (the in-plane rotation is omitted since only flat problems are

considered).

Their work was extended by Tenek and Hagiwara [113] so that the topology optimization of plates, as well as single and doubly curved shell structures are considered. Again, strain energy was minimized subject to a volume constraint. Both homogenization as well as optimal thickness distribution problems are considered. Again, simple four noded quadrilateral elements with 5 DOFs per node were employed with Selective Reduced Integration (SRI) to alleviate shear locking. They rely on the cubic relation between element stiffness and element thickness in bending to prevent intermediate densities.

There are of course numerous other authors who have used homogenization methods to solve topology optimization problems for plate and shell structures, for example see Díaz *et al.* [114], Krog and Olhoff [115], or see Bendsøe and Sigmund [4] for a more complete list of references.

Recently Hinton and co-workers [116, 117] have addressed the topology optimization problem of plate and shell structures using SIMP-like material models. A resizing algorithm based on Optimality Criteria (OC) methods is used to perform the iterative optimization. The Mindlin-Reissner based element used in their work is detailed in [118], and employs SRI on shear terms to overcome transverse shear locking. Since then SIMP-like material parameterizations have become very popular in this type of problem, see for example Pedersen [119], Jog [120] (who incidentally implement the MITC4 and MITC9 elements of Bathe and co-workers [16]) and Stegmann and Lund [121], who also use MITC elements.

Other interesting developments include simultaneous shape and topology optimization as performed by Ansola *et al.* [1, 2] and the hybrid (Homogenization-Evolutionary) method developed by the ADOPT group, see for example [122, 123, 124] which has been used in static and vibration problems of plate and shell structures.

Meanwhile, many advances have been made in finite element technology, which have a direct bearing on topology optimization, since most of the applications in topology optimization employ the finite element method as an analysis tool. Often, however, little attention is paid to the actual finite element formulation in the application. In this chapter, the abilities of the more sophisticated finite element formulations are leveraged in a topology optimization setting.

Element selection is an important part of finite element analysis, relying on the experience of the analyst to select a suitable element type. There are several different models for physical structural elements, e.g. beam, two dimensional planar, plate and shell, or solid models. Each of these models may have several different formulations, e.g. displacement-based, hybrid and mixed formulations, etc. perhaps with various interpolations or other mechanisms to improve element accuracy.

In this chapter, flat shell finite elements as an assembly of plate and membrane elements are considered. These elements can only be effective if the membrane and plate components are independently accurate and robust. To illustrate this point, it is demonstrated that the use of dubious, ad-hoc treatments of, in particular in-plane rotations and methods to overcome shear locking could lead to misleading ‘optimal’ topologies.

Flat shell elements are simpler than generally curved shell elements, both in terms of formu-

lation and computer implementation. Since the element Jacobian matrix is constant through the thickness, analytical through thickness integration is possible. Furthermore, in flat shell elements the inclusion of drilling DOFs is straightforward and, if required, element out of plane warp can be handled on the element level with the aid of warp corrections to the nodal DOFs.

Flat shell elements generally allow for 6 DOFs per node, two in-plane displacements and one in-plane rotation (membrane contributions) and the remaining two out of plane rotations and single out of plane displacement (plate bending components). The membrane component of a the flat shell element is considered first.

In general, membrane elements only require two displacement DOFs per node to adequately describe the kinematics. However, in membrane and shell elements, the additional rotational DOFs are highly desirable. They allow for the modeling of, for instance, folded plates and beam-slab intersections. Due to the enriched displacement field, these elements are also significantly more accurate than their counterparts with translational DOFs only [21]. For bending dominated problems for example, drilling DOFs enhance the accuracy of 4-node elements to a level comparable to that of 8- or 9-node elements, while the 4-node element with translational DOFs only (Q4) is notoriously inaccurate. Since provision is generally made for the in-plane rotation, regardless of how it is derived, including drilling DOFs in flat shell element formulations is largely (numerically) free of charge. Further detail regarding these elements can be found in Chapters 2 and 3.

As a flat shell element is constituted of membrane and plate components a suitable plate component is also crucial to the formulation. Successful quadrilateral isotropic plate and shell elements are mostly based on discrete Kirchhoff-Love theory (e.g. the Discrete Kirchhoff Quadrilateral (DKQ) [125]) or first order shear deformation theory of Mindlin-Reissner. The discrete Kirchhoff-Love theory allows only for shear rigid formulation and existence of the integral expressions of the stiffness matrices requires C^1 continuity of interpolation functions. The Mindlin-Reissner theory includes shear deformation and only C^0 continuity of the shape functions is required. For a large range of engineering problems, especially layered composites, exclusion of shear deformation leads to unacceptable results and the Mindlin-Reissner plate formulation is preferred.

However, 4-node displacement-based plate elements derived from Mindlin-Reissner theory are prone to severe locking associated with the transverse shear deformation and therefore require modifications in the finite element interpolation to alleviate this shear locking. Shear locking was overcome in a number of elements through the use of reduced or Selective Reduced Integration (SRI) schemes. For 4-node plate bending elements, these integration schemes, however, result in the appearance of spurious zero energy modes. A number of elements with stabilization methods [89] overcome this problem, however these elements generally require adjustable parameters.

Although these elements are reported to be highly accurate, alternative methods such as assumed strain or mixed methods are based on variational principles and are theoretically better founded. A number of elements based on Mindlin-Reissner theory exist. They differ mainly with respect to the assumptions in the finite element interpolation or in the handling of kinematic locking phenomena. One of the most efficient element formulations appears to

be the Assumed Natural Strain (ANS) formulation of Bathe and Dvorkin [126, 127], which has some similarities to the elements proposed by MacNeal [128] and Hughes and Tezduyar [129], and are also known as MITCn (Mixed Interpolation of Tensorial Components) elements, with n the number of nodes.

In this work it is illustrated that, for the SIMP method, Kirchhoff and Mindlin-Reissner based elements result in different topologies for thick plate problems. SRI, as a method to overcome shear locking, is also analyzed and compared to an ANS formulation. Finally, an investigation of the effect of drilling DOFs in membrane and shell elements is reported on.

In the longer term, the aim is to suggest suitable element formulations for work in piezoelectric actuators, to be used in micropositioning applications[1]. We should, nonetheless be mindful of the dangers inherent in the linear assumption [130] in plate and shell formulations, and its effect in topology optimization [121]. However since micropositioning applications with extremely small displacements are of interest, the linear assumption is applicable here. Ultimately this research is to be used for the selection of suitable piezoelectric finite element formulations for topological optimization applications, similar to those in for example [131].

This chapter is set out as follows: In Section 6.3 a discussion of the topology optimization problem formulation, and the material parameterization used, is briefly presented. In Section 6.4 a short summary of the finite element formulations used in this work are offered. Section 6.5 presents the findings of the numerical experiments carried out on membrane, plate and shell problems. Finally, some concluding remarks are presented in Section 6.6.

6.3 Topology optimization problem formulation

In this section, a discussion of the topology optimization formulation used for evaluation, is briefly presented. Minimum compliance membrane, plate and shell problems are specifically focused on. Some details of the material parameterization of multilayer designs are given. Also presented is a very short description of the optimality criteria based updating scheme employed, as well as the filtering strategy employed to address the mesh dependency problem.

6.3.1 Material parameterization

The discretized finite element model is parameterized using the popular Simple Isotropic Material with Penalization (SIMP) method [4], in which material properties are scaled with an artificial density parameter ρ, as will be detailed in this section. As a simple example, the elastic modulus is parameterized as

$$E = \rho^p E^0, \tag{6.1}$$

where ρ is an artificial density parameter with $0 \leq \rho \leq 1$ and p (usually $1 < p \leq 6$) is a penalty exponent which renders intermediate densities uneconomical, encouraging the design to a discrete solution. Finally, E is the modified (parameterized) modulus of elasticity of a region with artificial density ρ. The materials actual elastic modulus is given by E^0.

[1] However, for the time being, only linear elastic finite element formulations are considered.

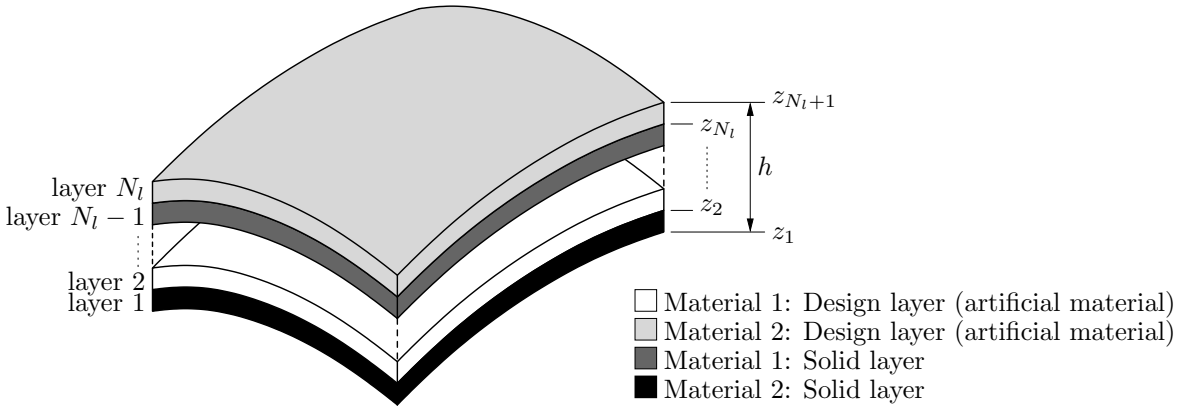

Figure 6.1: A schematic representation of a general material layup for topology optimization problems.

As in Lee *et al.* [116] and Stegmann and Lund [121] numerical experiments with multilayer shell models are performed. Perforated plates and shells as well as reinforcement, honeycomb or general multilayer structures are therefore allowed for. Only layups of isotropic materials are considered, although extension to orthotropic materials with constant [121] or variable [132] material coordinates is also possible.

Perfect bonding between adjacent layers is assumed, allowing for the use of a single element through the thickness. Although the same material is used for each layer, material properties can of course vary due to layerwise artificial density variations. The constitutive relations are computed using classical laminate theory by analytical through the thickness integration.

For the isotropic materials used in this study, the stress resultant form of the constitutive equations can be calculated by pre-integration through the thickness. Thus for for a laminate of thickness h with N_l layers, the relations between the stress resultants and strains for multilayer shells can be expressed as [116]

$$\begin{Bmatrix} \boldsymbol{N} \\ \boldsymbol{M} \\ \boldsymbol{Q} \end{Bmatrix} = \begin{bmatrix} \boldsymbol{\mathcal{A}}(\rho) & \boldsymbol{\mathcal{B}}(\rho) & \mathbf{0} \\ \boldsymbol{\mathcal{B}}(\rho) & \boldsymbol{\mathcal{D}}(\rho) & \mathbf{0} \\ \mathbf{0} & \mathbf{0} & \boldsymbol{\mathcal{G}}(\rho) \end{bmatrix} \begin{Bmatrix} \boldsymbol{\epsilon}_{\mathrm{m}} \\ \boldsymbol{\kappa} \\ \boldsymbol{\gamma} \end{Bmatrix}, \tag{6.2}$$

where $\boldsymbol{\epsilon}_{\mathrm{m}}$, $\boldsymbol{\kappa}$ and $\boldsymbol{\gamma}$ are the membrane, bending and transverse shear strains respectively and $\boldsymbol{N}$, $\boldsymbol{M}$ and $\boldsymbol{Q}$ are the corresponding stress resultants.

Figure 6.1 schematically shows the problem considered. Although an identical material for each layer is used, the general case in which each layers material type may vary, even without artificial density effects, is presented. Specifically, the submatrices in (6.2) are calculated for each element as:

Membrane stiffness:

$$\boldsymbol{\mathcal{A}}(\boldsymbol{\rho}) = \int_{-\frac{h}{2}}^{\frac{h}{2}} \boldsymbol{C}(\boldsymbol{\rho}, z)\mathrm{d}z = \sum_{i=1}^{N_l} {\rho_i}^p \boldsymbol{C}_i(z_{i+1} - z_i). \tag{6.3}$$

Membrane-bending stiffness:

$$\boldsymbol{\mathcal{B}}(\boldsymbol{\rho}) = \int_{-\frac{h}{2}}^{\frac{h}{2}} \boldsymbol{C}(\boldsymbol{\rho}, z) z \mathrm{d}z = \frac{1}{2} \sum_{i=1}^{N_l} \rho_i{}^p \boldsymbol{C}_i (z_{i+1}^2 - z_i^2). \tag{6.4}$$

Bending stiffness:

$$\boldsymbol{\mathcal{D}}(\boldsymbol{\rho}) = \int_{-\frac{h}{2}}^{\frac{h}{2}} \boldsymbol{C}(\boldsymbol{\rho}, z) z^2 \mathrm{d}z = \frac{1}{3} \sum_{i=1}^{N_l} \rho_i{}^p \boldsymbol{C}_i (z_{i+1}^3 - z_i^3). \tag{6.5}$$

Transverse shear stiffness:

$$\boldsymbol{\mathcal{G}}(\boldsymbol{\rho}) = \int_{-\frac{h}{2}}^{\frac{h}{2}} \boldsymbol{D}(\boldsymbol{\rho}, z) \mathrm{d}z = \sum_{i=1}^{N_l} \rho_i{}^p \boldsymbol{D}_i (z_{i+1} - z_i). \tag{6.6}$$

For plane stress, $\boldsymbol{C}_i$ and $\boldsymbol{D}_i$ are given by

$$\boldsymbol{C}_i = \frac{E_i^0}{(1-\nu_i^2)} \begin{bmatrix} 1 & \nu_i & 0 \\ \nu_i & 1 & 0 \\ 0 & 0 & \frac{(1-\nu_i)}{2} \end{bmatrix}, \text{ and} \tag{6.7}$$

$$\boldsymbol{D}_i = \frac{k\ E_i^0}{2(1+\nu_i)} \begin{bmatrix} 1 & 0 \\ 0 & 1 \end{bmatrix}. \tag{6.8}$$

In the foregoing, E_i^0 is the elastic modulus and ν_i the Poisson's ratio of the material in layer i, and k is the shear correction factor. The artificial density of layer i is denoted ρ_i. Note that layers that are *a priori* solid or void, and therefore do not form part of the design problem, are simply accounted for by setting $\rho_i = 1$ for solid layers or $\rho_i = \rho_{\min}$ for void layers. The vector containing the density in the N_l layers is denoted $\boldsymbol{\rho}$.

Usually, topology optimization problems impose a constraint on the amount of material or resource which can be utilized. The volume of a given element can be computed (assuming a constant area A through the thickness) as

$$V_e(\boldsymbol{\rho}) = \int_{-\frac{h}{2}}^{\frac{h}{2}} A(\boldsymbol{\rho}) \mathrm{d}z = \sum_{i=1}^{N_l} \rho_i\ A(z_{i+1} - z_i). \tag{6.9}$$

The volume of the entire structure is then easily computed as the sum of all element volumes:

$$V = \sum_{e=1}^{N_{el}} V_e, \tag{6.10}$$

where N_{el} represents the total number of elements in the assembly. In this work the design volume, or the volume of the design domain, will also be referred to. This is calculated as the difference between the total volume (6.10) and the volume of the elements or layers which are prescribed to be solid or void. In other word, the design volume is the volume of all the layers which are a function of the design variables (artificial densities).

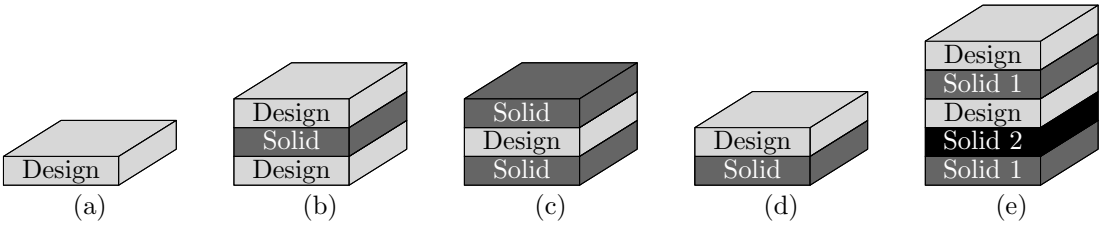

Figure 6.2: Various multilayer models with solid and design layers. (a) Single layer model, (b) Ribbed layup, (c) Honeycomb layup, (d) eccentric stiffened material model and (e) general asymmetric layup.

6.3.2 Layer models

Numerous laminate material models are possible using the material parameterization described in Section 6.3.1. Some of the popular schemes which have been used by other researchers are shown in Figure 6.2. Specifically, the examples depicted in Figure 6.2 are:

1. Single layer material model, depicted in Figure 6.2(a). This represents the classical topology optimization problem for plate and shell problems, and allows for the introduction of holes through the entire thickness (perforated plates/shells).

2. Three layer ribbed or rib stiffened material model, graphically represented in Figure 6.2(b). This model maintains an inner layer which is *a priori* solid with outer layers consisting of artificial material, allowing for the introduction of stiffening zones concentric to the shell mid-surface.

3. Three layer honeycomb model schematically depicted in Figure 6.2(c). This layup maintains two solid outer layers of equal thickness, concentric to the mid-surface, and an inner layer consisting of artificial material. This material description allows for core design. Although Stegmann *et al.* [121] question the practical interpretation of such a design problem, this material model will be employed as a benchmark for comparison with previously published results.

4. Other more general material models. Models 1 to 3 above, all result in symmetric material distributions, and therefore result in no membrane-bending coupling, i.e. $\boldsymbol{\mathcal{B}} = \mathbf{0}$. For problems such as the two-layer eccentric stiffener in Figure 6.2(d) and the general asymmetric laminate in Figure 6.2(e), coupling between membrane and bending actions becomes important. Although these material models present no real conceptual difficulty, we restrict ourselves to models 1 to 3 above. The effect of numerically adjustable parameters and element formulation on these more 'traditional' problems are to be investigated, especially since piezoelectric actuators usually result in symmetric layups as, for example, the case of piezoelectric bimorphs.

6.3.3 Problem formulation and sensitivities

In this work, the traditional topology optimization problem of minimizing compliance is considered. The minimum compliance problem may be written as

$$\min_{\boldsymbol{\rho}} c(\boldsymbol{\rho}) \tag{6.11}$$

$$\text{such that : } \sum_{e=1}^{N_{el}} V_e \leq V^*, \tag{6.12}$$

$$: \boldsymbol{KQ} = \boldsymbol{F}, \tag{6.13}$$

$$: 0 < \rho_{\min} \leq \rho_e \leq 1, \quad e = 1, 2, \ldots, N_{el} \tag{6.14}$$

where c is the compliance given by $c(\boldsymbol{\rho}) = \boldsymbol{F}^T\boldsymbol{Q}(\boldsymbol{\rho})$, and where the displacements are determined from $\boldsymbol{Q}(\boldsymbol{\rho}) = \boldsymbol{K}(\boldsymbol{\rho})^{-1}\boldsymbol{F}$. In this problem, the force vector $\boldsymbol{F}$ is independent of the artificial density. The allowable volume is denoted V^*. The sensitivity of the linear volume constraint in (6.12) can easily be determined. The sensitivity of the compliance (6.11) can be calculated using the adjoint method [4]. It can easily be shown that

$$\frac{\partial c}{\partial \rho_e} = -\boldsymbol{Q}^T \frac{\partial \boldsymbol{K}}{\partial \rho_e}\boldsymbol{Q}, \quad e = 1, 2, \ldots, N_{el}. \tag{6.15}$$

This problem has been presented in some detail in Chapter 5, Section 5.4.1. Note that in the treatment above, each element e in the finite element mesh has only one corresponding density variable ρ_e. In the case of the three layer stiffening model, for example, this variable scales the material properties of the two outer layers simultaneously. Each layer's material properties could of course be scaled independently, and therefore in up to N_l variables for each element (without any solid or void layers) are possible. However, only the former procedure is considered here.

6.3.4 Design update and filtering strategies

In Section 6.3.3 it was described how the function value and constraint functions are evaluated. In this section the design updating scheme as well as the treatment of some numerical difficulties in topology optimization are briefly discussed.

The design update is carried out using the standard fixed-point updating scheme based on the conditions of optimality [4], i.e.

$$\rho_{k+1} = \begin{cases} \max\{(1-\zeta)\rho_k, \rho_{\min}\}, & \text{if } \rho_k B_k^{\eta} \leq \max\{(1-\zeta)\rho_k, \rho_{\min}\} \\ \min\{(1+\zeta)\rho_k, 1\}, & \text{if } \min\{(1+\zeta)\rho_k, 1\} \leq \rho_k B_k^{\eta} \\ \rho_k {B_k}^{\eta} & \text{otherwise} \end{cases} \tag{6.16}$$

where $B_k = -\frac{\partial c}{\partial \rho_k}{\lambda_k}^{-1}$, λ_k is the Lagrange multiplier enforcing the volume constraint and determined using a simple bisection method, and where $\zeta = 0.2$ is a move limit and $\eta = \frac{1}{2}$ is a tuning parameter. The density distribution at iteration k is denoted ρ_k. Although the optimal topology calculated using this scheme is known to be somewhat sensitive to the

parameters ζ and η [116], the aforementioned settings are exclusively used for all results presented herein. In this way, the effect of element formulation on optimal topology is isolated.

The final implementational issue is that of mesh dependency. In order to overcome this problem, as well as the checkerboarding problem (see [4, 13, 100] for details) the sensitivity filtering method of Sigmund [100] is used, with a filter radius of 1.2 element side lengths in all cases.

6.4 Finite element formulations

In this section, the formulations of the various shell finite elements used in the numerical experiments, are briefly outlined. Flat shell finite elements, which can be thought of as an assemblage of membrane and plate components, are employed.

Without presenting details of the various finite element formulations at this point, the resulting discretized system can be described using

$$\boldsymbol{K}\boldsymbol{Q} = \boldsymbol{F}, \tag{6.17}$$

which usually results from minimization of appropriate functionals based on linear elasticity assumptions. Here $\boldsymbol{F}$ is a vector representing the global forces and moments, and $\boldsymbol{Q}$ is the associated vector of global displacements and rotations. $\boldsymbol{K}$ is the global stiffness matrix, comprising all the assembled elemental stiffness matrices:

$$\boldsymbol{K} = \mathbf{A}_{e=1}^{Nel} \boldsymbol{k}_e, \tag{6.18}$$

where $\mathbf{A}$ represents the assembly operator and $\boldsymbol{k}_e$ the elemental stiffness matrix in the global coordinate system. In this chapter, membrane, plate and shell problems are considered, and therefore some details of the formulation of shell elements, which can be used to solve all of the presented test problems, are presented. Each shell finite element, with associated elemental displacements and rotations, can be further decomposed as

$$\boldsymbol{k}\,\boldsymbol{q} = \begin{bmatrix} \boldsymbol{k}_{\mathrm{m}} & \boldsymbol{k}_{\mathrm{mp}} \\ \boldsymbol{k}_{\mathrm{mp}}^T & \boldsymbol{k}_{\mathrm{p}} \end{bmatrix} \begin{Bmatrix} \boldsymbol{q}_{\mathrm{m}} \\ \boldsymbol{q}_{\mathrm{p}} \end{Bmatrix}; \qquad \begin{aligned} \boldsymbol{k}_{\mathrm{p}} &= \boldsymbol{k}_{\mathrm{b}} + \boldsymbol{k}_{\mathrm{s}} \\ \boldsymbol{k}_{\mathrm{mp}} &= \boldsymbol{k}_{\mathrm{mb}} + \boldsymbol{k}_{\mathrm{ms}} \end{aligned} \tag{6.19}$$

where $\boldsymbol{k}$ represents the stiffness matrix in a locally defined coordinate system, with related local nodal displacements and rotations $\boldsymbol{q}$. The partitioned membrane and plate stiffness matrices are denoted $\boldsymbol{k}_{\mathrm{m}}$ and $\boldsymbol{k}_{\mathrm{p}}$, respectively. The coupling stiffness between membrane and plate actions is denoted $\boldsymbol{k}_{\mathrm{mp}}$.

As indicated in (6.19), the plate component of the stiffness matrix is composed of bending ($\boldsymbol{k}_{\mathrm{b}}$) and transverse shear ($\boldsymbol{k}_{\mathrm{s}}$) components. Similarly the coupling between plate actions can be decomposed into coupling between membrane and bending ($\boldsymbol{k}_{\mathrm{mb}}$) and that between membrane and transverse shear ($\boldsymbol{k}_{\mathrm{ms}}$). It is usually assumed that there is no coupling between membrane and transverse shear, or between bending and transverse shear components. The local shell stiffness matrix can therefore be rewritten as

$$\boldsymbol{k} = \begin{bmatrix} \boldsymbol{k}_{\mathrm{m}} & \boldsymbol{k}_{\mathrm{mp}} \\ \boldsymbol{k}_{\mathrm{mp}}^T & \boldsymbol{k}_{\mathrm{p}} \end{bmatrix}. \tag{6.20}$$

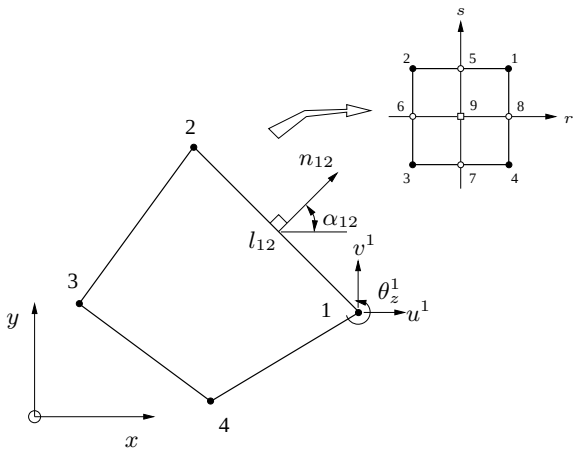

Figure 6.3: Quadrilateral element with drilling degrees of freedom.

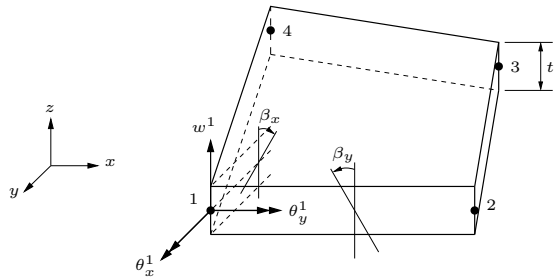

Figure 6.4: Quadrilateral Mindlin-Reissner plate element.

In the foregoing, the associated local displacements $\boldsymbol{q}$ are decomposed into terms associated with membrane actions, $\boldsymbol{q}_{\rm m}$, and those associated with the plate component, $\boldsymbol{q}_{\rm p}$. Specifically, $\boldsymbol{q}_{\rm m} = [\boldsymbol{u}\ \boldsymbol{v}\ \boldsymbol{\theta}_z]^T$, where $[\boldsymbol{u}\ \boldsymbol{v}]^T$ represent the in-plane nodal displacements only, and $\boldsymbol{\theta}_z$ denotes the in-plane rotations or drilling DOFs at each node. A quadrilateral membrane element with drilling DOFs is schematically depicted in Figure 6.3. The plate transverse displacement and rotations are given by $\boldsymbol{q}_{\rm p} = [\boldsymbol{w}\ \boldsymbol{\theta}_x\ \boldsymbol{\theta}_y]^T$, as shown in Figure 6.4.

For clarity, some detail of the membrane and plate components of the elemental stiffness matrix are now presented separately in the local coordinate system.

6.4.1 Membrane elements

Two membrane finite element formulations are employed in this work. The first is the traditional Q4 displacement based element which neglects in-plane rotations. The rotations can, however, be accommodated by an extremely simple, but *ad hoc* treatment. This method has no theoretical basis, and is used to illustrate the pitfalls of an improper treatment of element deficiencies.

The second membrane element is based on the variational formulation due to Hughes and

Brezzi [18], with the finite element implementation investigated by Ibrahimbegovic *et al.* [21]. This formulation, detailed in Chapter 2, is based on a rigorous mathematical foundation, and represents a robust, accurate membrane element.

Standard displacement based membrane element

The first membrane element is the standard displacement-based quadrilateral element with bilinear displacement interpolations, see for example [17]. The potential energy functional used to derive the elemental stiffness matrix is given by:

$$\Pi_{\mathrm{m}}^{\mathrm{Q4}}(\boldsymbol{u}_{\mathrm{m}}) = \frac{1}{2}\int_V {\boldsymbol{\epsilon}_{\mathrm{m}}}^T \boldsymbol{C}_{\mathrm{m}} \boldsymbol{\epsilon}_{\mathrm{m}} \mathrm{d}V - \frac{1}{2}\int_V {\boldsymbol{u}_{\mathrm{m}}}^T \boldsymbol{f} \mathrm{d}V, \tag{6.21}$$

where

$${\boldsymbol{\epsilon}_{\mathrm{m}}}^T = \left[\frac{\partial u}{\partial x}\ ;\quad \frac{\partial v}{\partial y}\ ;\quad \frac{\partial u}{\partial y} + \frac{\partial v}{\partial x}\right], \tag{6.22}$$

and $\boldsymbol{C}_{\mathrm{m}}$ is the constitutive relation. The displacement field is denoted $\boldsymbol{u}_{\mathrm{m}} = [u\ v]^T$ and $\boldsymbol{f}$ is the body force vector field. Surface tractions and point forces can be considered in the standard fashion [17].

The element stiffness matrix which results from this functional, is given by

$$\boldsymbol{k}_{\mathrm{m}}^{\mathrm{Q4}}(\rho) = \int_A [\boldsymbol{B}_{\mathrm{m}}^{\mathrm{Q4}}]^T \boldsymbol{\mathcal{A}}(\rho) \boldsymbol{B}_{\mathrm{m}}^{\mathrm{Q4}} \mathrm{d}A, \tag{6.23}$$

where $\boldsymbol{B}_{\mathrm{m}}^{\mathrm{Q4}}$ is the strain-displacement operator and $\boldsymbol{\mathcal{A}}(\rho)$ is the through thickness integrated constitutive relation given in (6.3). Note that $\boldsymbol{\mathcal{A}}$ is a function of the artificial density introduced in the SIMP material parameterization procedure.

This element formulation neglects the in-plane rotational field, θ_z, and possesses only two degrees of freedom per node. The dimension of $\boldsymbol{k}_{\mathrm{m}}^{\mathrm{Q4}}$ is therefore only 8×8. For planar problems this treatment is adequate. However, for general shell problems the additional in-plane rotational DOF is required. A method which is sometimes used to account for the in-plane rotation is simply to add a small fictitious stiffness to each drilling DOF. This is done by simply replacing the on-diagonal 4×4 null matrix with the matrix $\boldsymbol{k}_{\theta z}$ given in (6.25).

$$\boldsymbol{k}_{\mathrm{m}}^{\mathrm{Q4}\alpha} = \begin{bmatrix} \boldsymbol{k}_{\mathrm{m}}^{\mathrm{Q4}} & \boldsymbol{0}_{8\times 4} \\ \boldsymbol{0}_{4\times 8} & \boldsymbol{k}_{\theta z} \end{bmatrix}, \tag{6.24}$$

$$\text{where } \boldsymbol{k}_{\theta z} = \alpha V E(\rho) \begin{bmatrix} 1 & -\frac{1}{3} & -\frac{1}{3} & -\frac{1}{3} \\ & 1 & -\frac{1}{3} & -\frac{1}{3} \\ & & 1 & -\frac{1}{3} \\ & \text{symm} & & 1 \end{bmatrix}, \tag{6.25}$$

where α is an adjustable parameter, V is the volume of the element and $E(\rho)$ is the elastic modulus which is a function of the element artificial density. As in Cook *et al.* [17] the added matrix provides each drilling DOF with a fictitious stiffness, but offers no resistance to the mode $\theta_z^1 = \theta_z^2 = \theta_z^3 = \theta_z^4$, or any other rigid mode.

This *ad hoc* treatment results in no coupling between in-plane displacements and in-plane rotations, and will probably be sensitive to element aspect ratio and distortion. Although this method is heuristic, it is tempting since implementation is trivial. Of course there are numerous other ways of treating drilling DOFs suggested in the literature, see for example [23, 24, 33]. Most methods result in a rank deficient stiffness matrix and therefore require some form of stability control which introduces other adjustable parameters to avoid potential spurious results.

Membrane element with drilling DOFs

The second membrane element accounts for in-plane rotations based on their continuum mechanics definition. The approach relies on a variational formulation employing an independent rotation field, as presented by Hughes and Brezzi [18]. The original element formulation with drilling DOFs was presented by Reissner [40]. However, the formulation of Reissner lacks stability in the discrete form. The variational problem of Reissner was modified by Hughes and Brezzi [18] in order to preserve the stability of the discrete problem. It utilizes the skew-symmetric part of the stress tensor as a Lagrange multiplier to enforce equality of independent rotations and the skew-symmetric part of the displacement gradient in a weak sense. The stress tensor is therefore not *a priori* assumed to be symmetric.

Hughes and Brezzi show that a displacement-based functional can be derived by eliminating the skew-symmetric part of stress from a mixed-type functional. Employing a notation similar to that in [22], the result is the modified functional

$$\Pi_{\mathrm{m}}^{\mathrm{Q4}\gamma}(\boldsymbol{u}_{\mathrm{m}}, \theta_z) = \frac{1}{2}\int_V {\boldsymbol{\epsilon}_{\mathrm{m}}}^T \boldsymbol{C}_{\mathrm{m}} \boldsymbol{\epsilon}_{\mathrm{m}} \mathrm{d}V + \frac{1}{2}\gamma \int_V (\omega_{xy} - \theta_z)^2 \mathrm{d}V - \frac{1}{2}\int_V {\boldsymbol{u}_{\mathrm{m}}}^T \boldsymbol{f} \mathrm{d}V, \tag{6.26}$$

where ω_{xy} is the skew-symmetric part of the displacement gradient, given by

$$\omega_{xy} = \frac{\partial v}{\partial x} - \frac{\partial u}{\partial y}, \tag{6.27}$$

see Chapter 2 for details. The translations are related to the in-plane rotations by γ, overcoming the rank deficiency present in many formulations with drilling DOFs. The patch test is passed for all $\gamma > 0$. The functional in (6.26) requires only interpolation of displacements and rotations. The stationary point can be found in the usual manner. The independent rotations are interpolated using standard bilinear functions, while the in-plane displacement approximation is taken as an Allman-type interpolation [23].

In matrix form the first term of $\Pi_{\mathrm{m}}^{\mathrm{Q4}\gamma}$ can be shown to reduce to

$$\tilde{\boldsymbol{k}}_{\mathrm{m}}^{\mathrm{Q4}\gamma} = \int_A \left[\boldsymbol{B}_{\mathrm{m}}^{\mathrm{Q4}\gamma} \;\; \boldsymbol{G}_{\mathrm{m}}^{\mathrm{Q4}\gamma}\right]^T \boldsymbol{\mathcal{A}}(\rho) \left[\boldsymbol{B}_{\mathrm{m}}^{\mathrm{Q4}\gamma} \;\; \boldsymbol{G}_{\mathrm{m}}^{\mathrm{Q4}\gamma}\right] \mathrm{d}A, \tag{6.28}$$

where $\tilde{\boldsymbol{k}}_{\mathrm{m}}^{\mathrm{Q4}\gamma}$ is a 12×12 matrix. This is in fact the QC9 or QC9(8) element (depending on the integration scheme employed to integrate the element area Ω^e). This rank deficient element was reported by Stander and Wilson [95] further to the work of Taylor and Simo [37].

To eliminate the rank deficiency, the following penalty term, in matrix form, corresponding to the second term of $\Pi_{\mathrm{m}}^{\mathrm{Q4}\gamma}$ is derived:

$$\boldsymbol{p}_{\mathrm{m}}^{\gamma} = \gamma(\rho) \int_A \begin{Bmatrix} \boldsymbol{b}_{\mathrm{m}}^{\mathrm{Q4}\gamma} \\ \boldsymbol{g}_{\mathrm{m}}^{\mathrm{Q4}\gamma} \end{Bmatrix} \begin{bmatrix} \boldsymbol{b}_{\mathrm{m}}^{\mathrm{Q4}\gamma} & \boldsymbol{g}_{\mathrm{m}}^{\mathrm{Q4}\gamma} \end{bmatrix} \mathrm{d}A \tag{6.29}$$

$$\text{where } \gamma(\rho) = \alpha G(\rho), \tag{6.30}$$

with G the shear modulus which is a function of the artificial density variable, and α an adjustable parameter as in (6.25). Quite a number of studies have reported a suitable value of γ. In their original work, Hughes and Brezzi [18] suggest a value of $\gamma = G$, the shear modulus. Recently, however, it has been shown that lower values of γ, such as $\gamma = G \times 10^{-2}$ gives better results [20, 58] and Chapter 2. Again, γ is a function of the element's artificial density ρ.

The element stiffness matrix therefore becomes

$$\boldsymbol{k}_{\mathrm{m}}^{\mathrm{Q4}\gamma} = \tilde{\boldsymbol{k}}_{\mathrm{m}}^{\mathrm{Q4}\gamma} + \boldsymbol{p}_{\mathrm{m}}^{\gamma}, \tag{6.31}$$

$\boldsymbol{p}_{\mathrm{m}}^{\gamma}$ is integrated by a single point Gaussian quadrature. By fully integrating $\tilde{\boldsymbol{k}}_{\mathrm{m}}^{\mathrm{Q4}\gamma}$ and combining with $\boldsymbol{p}_{\mathrm{m}}^{\gamma}$, spurious zero energy modes are prevented [21]. No additional devices (e.g. see [24]) are needed. The same holds if a modified 8-point quadrature, or 5-point rule [52], is employed to integrate $\tilde{\boldsymbol{k}}_{\mathrm{m}}^{\mathrm{Q4}\gamma}$ [21].

The forms of $\boldsymbol{B}_{\mathrm{m}}^{\mathrm{Q4}\gamma}$, $\boldsymbol{G}_{\mathrm{m}}^{\mathrm{Q4}\gamma}$, $\boldsymbol{b}_{\mathrm{m}}^{\mathrm{Q4}\gamma}$ and $\boldsymbol{g}_{\mathrm{m}}^{\mathrm{Q4}\gamma}$ can be found in, for example [21, 52] or in Chapter 2.

Membrane locking correction

The membrane locking appearing in elements with drilling DOFs was alleviated in [21] by employing Taylor's correction [38]. The final modified membrane strain relationship of the correction is given by,

$$\bar{\boldsymbol{\epsilon}} = \boldsymbol{B}_{\mathrm{m}}^{\mathrm{Q4}\gamma}[\boldsymbol{u}\ \boldsymbol{v}]^T + \left(\boldsymbol{G}_{\mathrm{m}}^{\mathrm{Q4}\gamma} - \frac{1}{V_e} \int_{\mathrm{V}} \boldsymbol{G}_{\mathrm{m}}^{\mathrm{Q4}\gamma} \mathrm{dV} \right) \boldsymbol{\theta}_z, \tag{6.32}$$

where $[\boldsymbol{u}\ \boldsymbol{v}]$ and $\boldsymbol{\theta}_z$ are the nodal values for displacement and rotation respectively, and $\boldsymbol{B}_{\mathrm{m}}^{\mathrm{Q4}\gamma}$ and $\boldsymbol{G}_{\mathrm{m}}^{\mathrm{Q4}\gamma}$ are the same as those in (6.28), and their explicit form is shown in, for example [21]. Finally, V_e is the element volume.

6.4.2 Plate elements

In the numerical study to follow, three different plate elements are employed. The first is the popular Discrete Kirchhoff Quadrilateral (DKQ) element based on the Kirchhoff assumptions for thin plates, in which transverse shear is neglected. The other two elements are Mindlin-Reissner based elements, and differ only in the way in which shear locking is overcome.

Discrete Kirchhoff Quadrilateral plate element

DKQ plate elements are commonly used in the analysis of thin plate problems. Since transverse shear deformation (TSD) is not permitted (γ_{xz}=γ_{yz}=0) this plate, and of course the resulting shell, is transversely shear rigid.

The formulation of the DKQ element is based on the functional (after integration through the thickness)

$$\Pi_{\mathrm{p}}^{\mathrm{DKQ}}(\boldsymbol{\beta}, w) = \frac{1}{2}\int_A \boldsymbol{\kappa}^T \boldsymbol{C}_{\mathrm{b}} \boldsymbol{\kappa}\ \mathrm{d}A - \int_A w\ p\ \mathrm{d}A, \tag{6.33}$$

$$\text{such that : } \beta_x = \frac{\partial w}{\partial x} \text{ and } \beta_y = \frac{\partial w}{\partial y}, \tag{6.34}$$

where

$$\boldsymbol{\kappa}^T = [\frac{\partial \beta_x}{\partial x}\ ;\ \frac{\partial \beta_y}{\partial y}\ ;\ \frac{\partial \beta_x}{\partial y} + \frac{\partial \beta_y}{\partial x}], \tag{6.35}$$

is the curvature, $\boldsymbol{C}_{\mathrm{b}}$ is the moment-curvature relation, p is the lateral load including surface and body forces and w is the lateral displacement. Furthermore, $\theta_x = \frac{\partial w}{\partial y} = \beta_y$ and $\theta_y = -\frac{\partial w}{\partial x} = -\beta_x$, as shown in Figure 6.4.

To circumvent the difficulty of the required C^1 continuity, the lateral displacements w and the rotations of the normals to the undeformed mid-surface in the x, z and y, z planes (β_x and β_y respectively) are assumed independently. Discrete approximations to the constraint in (6.34) are imposed by discrete elimination.

The stiffness matrix of the DKQ element is defined in the standard manner for displacement models as [125]

$$\boldsymbol{k}_{\mathrm{p}}^{\mathrm{DKQ}} = \int_A [\boldsymbol{B}_{\mathrm{b}}^{\mathrm{DKQ}}]^T \boldsymbol{\mathcal{D}}(\rho) \boldsymbol{B}_{\mathrm{b}}^{\mathrm{DKQ}} \mathrm{d}A, \tag{6.36}$$

where the specific form of $\boldsymbol{B}_{\mathrm{b}}^{\mathrm{DKQ}}$ can be found in, for example Batoz and Tahar [125] and the bending rigidity matrix $\boldsymbol{\mathcal{D}}$ is a function of the artificial density ρ, as shown in (6.5).

Mindlin-Reissner plate element with selective reduced integration

Two Mindlin-Reissner plate elements based on first order shear deformation of Mindlin and Reissner are evaluated. Both are derived from the following functional which has been pre-integrated through the thickness:

$$\Pi_{\mathrm{p}}^{\mathrm{MR}}(\boldsymbol{\beta}, w) = \frac{1}{2}\int_A \boldsymbol{\kappa}^T \boldsymbol{C}_{\mathrm{b}} \boldsymbol{\kappa}\ \mathrm{d}A + \frac{1}{2}\int_A \boldsymbol{\gamma}^T \boldsymbol{C}_{\mathrm{s}} \boldsymbol{\gamma}\ \mathrm{d}A - \int_A w\ p\ \mathrm{d}A, \tag{6.37}$$

where $\boldsymbol{\kappa}$ is given in (6.35), $\boldsymbol{C}_{\mathrm{b}}$ is the moment-curvature relationship, $\boldsymbol{C}_{\mathrm{s}}$ is the constitutive relation between shear forces and transverse shear, including the shear correction term accounting for the quadratic transverse shear stress consistent with classical theory. Finally the transverse shear strains are defined as,

$$\boldsymbol{\gamma}^T = [\frac{\partial w}{\partial x} - \beta_x\ ;\ \frac{\partial w}{\partial y} - \beta_y]. \tag{6.38}$$

Assuming independent bilinear interpolations for the transverse displacement and section rotations, the resulting stiffness matrix for a Mindlin-Reissner plate element can be written as

$$\boldsymbol{k}_{\mathrm{p}}^{\mathrm{MR}} = \boldsymbol{k}_{\mathrm{b}}^{\mathrm{MR}} + \boldsymbol{k}_{\mathrm{s}}^{\mathrm{MR}} = \int_A [\boldsymbol{B}_{\mathrm{b}}^{\mathrm{MR}}]^T \boldsymbol{\mathcal{D}}(\rho) \boldsymbol{B}_{\mathrm{b}}^{\mathrm{MR}} \mathrm{d}A + \int_A [\boldsymbol{B}_{\mathrm{s}}^{\mathrm{MR}}]^T \boldsymbol{\mathcal{G}}(\rho) \boldsymbol{B}_{\mathrm{s}}^{\mathrm{MR}} \mathrm{d}A, \tag{6.39}$$

where the standard forms of $\boldsymbol{B}_{\mathrm{b}}^{\mathrm{MR}}$ and $\boldsymbol{B}_{\mathrm{s}}^{\mathrm{MR}}$ can be found in, for example [17]. It is well known that full integration of the stiffness matrix terms in (6.39) results in severe locking for thin plates [16, 22, 17]. A simple method to overcome the locking phenomenon is to employ a selective reduced integration (SRI) scheme on the shear part of the stiffness matrix $\boldsymbol{k}_{\mathrm{s}}^{\mathrm{MR}}$. This procedure will be employed to calculate the first Mindlin-Reissner plate stiffness matrix, i.e.

$$\boldsymbol{k}_{\mathrm{p}}^{\mathrm{SRI}} = \boldsymbol{k}_{\mathrm{b}}^{\mathrm{MR}} + \tilde{\boldsymbol{k}}_{\mathrm{s}}^{\mathrm{MR}}, \tag{6.40}$$

where $\boldsymbol{k}_{\mathrm{b}}^{\mathrm{MR}}$ is calculated using a 4-point scheme and $\tilde{\boldsymbol{k}}_{\mathrm{s}}^{\mathrm{MR}}$ is evaluated using a single point integration scheme. A potential problem with this method of overcoming locking due to the parasitic shear, is the introduction of spurious zero-energy modes. Two spurious modes are introduced if SRI is employed, one of which is not communicable. No hourglass control, e.g. see [93], will be used in order to demonstrate how this mode becomes problematic in topology optimization problems.

Mindlin Reissner plate element with assumed natural strain

The second Mindlin-Reissner-based plate element overcomes the effects of shear locking by assuming a mixed interpolation of transverse displacement, section rotations and transverse strains. In particular the Assumed Natural Strain (ANS) formulation of Bathe and Dvorkin [126, 127] is considered here. The element of Bathe and Dvorkin has some similarities to the elements of MacNeal [128] and Hughes and Tezduyar [129].

This element has the advantage that it doesn't have any numerically adjustable factors (often required for hourglass control). Furthermore, it contains no spurious zero-energy modes, and passes all appropriate patch tests.

The stiffness matrix derived from this interpolation procedure finally results in the stiffness matrix

$$\boldsymbol{k}_{\mathrm{p}}^{\mathrm{ANS}} = \boldsymbol{k}_{\mathrm{b}}^{\mathrm{MR}} + \boldsymbol{k}_{\mathrm{s}}^{\mathrm{ANS}} = \boldsymbol{k}_{\mathrm{b}}^{\mathrm{MR}} + \int_A [\boldsymbol{B}_{\mathrm{s}}^{\mathrm{ANS}}]^T \boldsymbol{\mathcal{G}}(\rho) \boldsymbol{B}_{\mathrm{s}}^{\mathrm{ANS}} \mathrm{d}A, \tag{6.41}$$

where the bending part of the stiffness matrix is identical to that of $\boldsymbol{k}_{\mathrm{p}}^{\mathrm{SRI}}$, but the shear part of the stiffness matrix is derived including the ANS interpolations and evaluated using full integration. The strain operator $\boldsymbol{B}_{\mathrm{s}}^{\mathrm{ANS}}$ can be derived as described in [16, 126].

6.4.3 Membrane-bending components

For non-symmetric laminates, coupling between membrane and bending constitutive components becomes significant, i.e. $\boldsymbol{\mathcal{B}}$ in (6.4) is non-zero. Naturally, this part of the partitioned stiffness matrix, denoted $\boldsymbol{k}_{\mathrm{mb}}$ in (6.20), is a function of the specific membrane and plate components which constitute a given shell element.

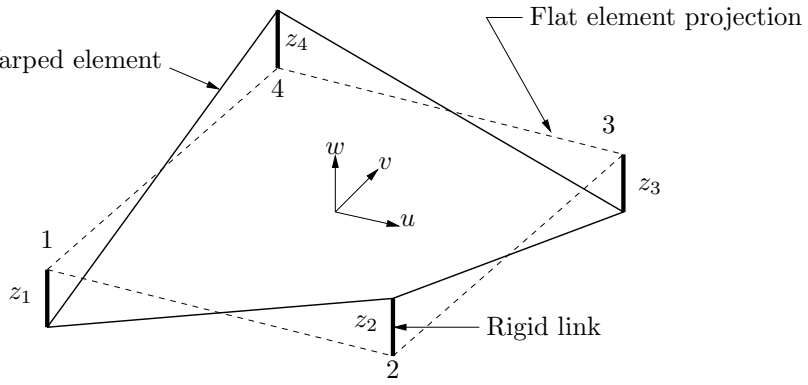

Figure 6.5: Warped and projected shell element.

The $\boldsymbol{k}_{\text{mb}}$ submatrix can simply be computed by premultiplying $\boldsymbol{\mathcal{B}}$ by the membrane strain-displacement operator, and postmultiplying by the bending strain-displacement operator. For simplicity however, in the numerical experiments presented herein only symmetric layups are considered, and consequently no coupling between membrane and bending actions is present.

6.4.4 Warp correction and local-global transformation

Where necessary, the effect of out-of-plane warp is corrected by using, the so-called 'rigid link correction' of Taylor [38], is employed to transform the nodal variables to the projected flat element variables. Figure 6.5 schematically shows the local warped and flat projected elements.

Ultimately, this corrected local element stiffness matrix $\boldsymbol{k}$ is transformed to the global coordinate system to yield,

$$\boldsymbol{k}^g = \boldsymbol{T}^T \boldsymbol{k} \boldsymbol{T} \tag{6.42}$$

where $\boldsymbol{T}$ is an appropriate transformation matrix.

6.4.5 Shell element denotation

Formulations of two membrane and three plate elements have been presented, which allows for a total of six different flat shell elements. In this section the denotations used for the various tested elements are presented.

The two membrane components are denoted:

- Q4α - The standard Q4 displacement based four node quadrilateral element with the *ad hoc* treatment of drilling DOFs. The Q4α stiffness matrix is given in (6.24).
- Q4γ - The four node membrane element based on the variational formulation of Hughes and Brezzi [18], and with local stiffness matrix given by (6.31).

The three plate components are denoted:

- DKQ - The plate element based on the Kirchhoff-Love thin plate assumption of shear rigidity. The stiffness matrix in local coordinates is presented in (6.36).
- SRI - The irreducible Mindlin-Reissner based element with selective reduced integration on transverse shear terms, and stiffness matrix given by (6.40).
- ANS - The assumed natural strain plate element based on Mindlin-Reissner assumptions, suggested by Bathe and Dvorkin [126], in which each of the natural strain components is independently interpolated. The elemental plate stiffness matrix is given in (6.41).

Shell elements will be denoted using first the membrane, followed by the plate designations. Recalling the form of the partitioned stiffness matrix in local coordinates, as presented in (6.20), the element made up of Q4α membrane and DKQ plate components can be represented as Q4αDKQ, with elemental stiffness matrix:

$$\boldsymbol{k}^{\mathrm{Q4}\alpha\mathrm{DKQ}} = \begin{bmatrix} \boldsymbol{k}_{\mathrm{m}}^{\mathrm{Q4}\alpha} & \boldsymbol{k}_{\mathrm{mb}}^{\mathrm{Q4}\alpha\mathrm{DKQ}} \\ (\boldsymbol{k}_{\mathrm{mb}}^{\mathrm{Q4}\alpha\mathrm{DKQ}})^T & \boldsymbol{k}_{\mathrm{p}}^{\mathrm{DKQ}} \end{bmatrix}. \tag{6.43}$$

Each partitioned matrix in (6.43) is 12×12 in size.

6.5 Numerical Examples

Several different finite element implementations are numerically tested in a SIMP topology optimization setting. A number of popular benchmark problems, which have been used mostly by researchers to verify effectiveness or correctness of implementation, are investigated. Some new problems, which highlight possible element deficiencies, are also introduced. Membrane, plate and shell problems are considered. In particular, we wish to investigate:

- The sensitivity of optimal topologies to parameters related to drilling DOFs in membrane and shell structures.
- The effect of employing Selective Reduced Integration (SRI) in Mindlin-Reissner plate elements, compared to mathematically sound and reliable procedures for overcoming shear locking.
- The difference in optimal topologies generated using elements based on Kirchhoff theory, compared to those using Mindlin-Reissner theory for thick and thin plate structures.

In each case, a uniform material distribution which exactly satisfies the volume constraint is chosen as an initial design or starting point. As detailed in Section 6.3.4 the mesh independency filter, due to Sigmund [100], is used to prevent checkerboarding. A filter radius equal to 1.2 times the element side length is utilized.

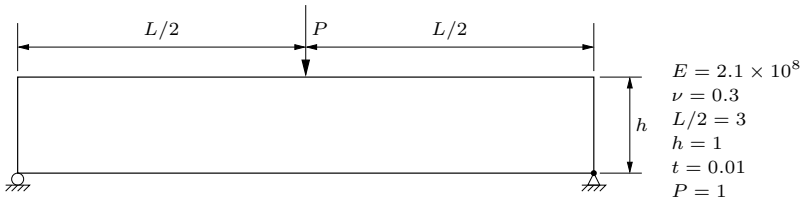

Figure 6.6: MBB beam geometry and constraints.

A stopping criterion based on the number of iterations only has been implemented. Therefore, in the discussion to follow the final topology, i.e. the topology after 100 iterations will be referred to as the optimal topology. In some cases numerical deficiencies cause singularities which result in the gradient of strain energy in particular elements to become very close to zero or even positive. In such circumstances, these spurious values are replaced manually by zero. This problem occurs only when SRI plate elements are used, and instances where the correction is made, are explicitly pointed out.

The remainder of this section details the results of the investigation into membrane, plate and finally shell problems. After each subsection, a brief discussion of the results is presented in which the most important points are emphasized.

6.5.1 Membrane example

Since the use of elements with drilling DOFs based on sound mathematical theory is advocated, it is important to determine the sensitivity of optimal topologies using elements with drilling DOFs, to the adjustable parameter α in Q4γ elements, see (6.30). For the purpose of this study, the popular MBB beam problem is selected.

MBB beam

The geometry, material properties, restraints and loading are all depicted in Figure 6.6. Although symmetry is used to model the structure, the complete topology is reported. In total 2700 square elements are used, 90 elements along the length of the finite element model, $L/2$ and 30 elements in the height h. Of course, since only membrane components are evaluated, only the single layer material model is tested. The available volume fraction is half of the design domain. In order to stabilize the convergence, the penalty exponent is stepped from 1 to 3. Also, the objective is normalized with respect to the starting value of compliance in order to improve the problem scaling.

Figure 6.7 depicts the sensitivity of the optimal compliance calculated using the Q4γ element to the value of the adjustable parameter α, see (6.30). Note that for the Q4γ membrane element, a value of $\alpha = 1$ corresponds the the value of γ suggested by Hughes and Brezzi [18]. However, recently a number of studies have suggested that a value of $\alpha = 10^{-2}$ results in more accurate solutions, see for example [20, 58] and Chapter 2. Therefore the upper bound of $\alpha = 10^2$ which is tested, is significantly higher than the optimal value suggested in

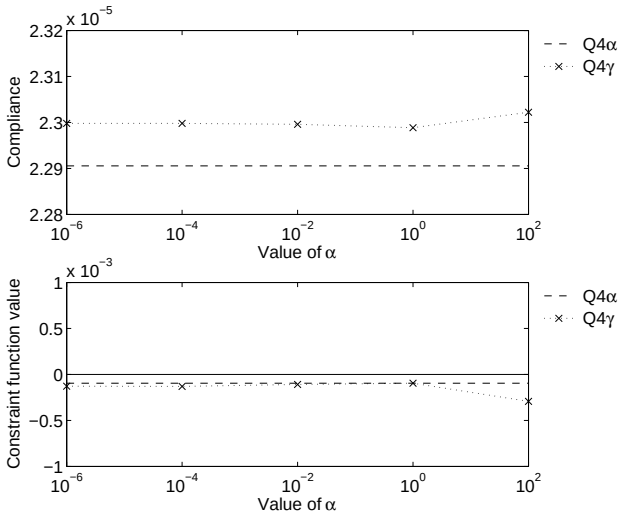

Figure 6.7: Compliance and constraint function values for optimal topologies as a function of α for the MBB beam problem.

the studies listed above. However, Hughes and Brezzi [18] showed that elements based on their variation formulation are convergent for all values of $\alpha > 0$.

It is clear from this figure that the optimal value of compliance computed using Q4γ elements is not significantly sensitive to the value of α. In fact, the slight increase in compliance around $\alpha = 10^2$ can be attributed to a corresponding decrease in volume, depicted in Figure 6.7, at this point rather than an elemental phenomenon. For this example, the optimal topology calculated using Q4α elements is of course insensitive to the value of α. In fact, for all 2-D planar analyses the correction in (6.24) is unnecessary since the standard Q4 element ($\boldsymbol{k}_{\mathrm{m}}^{\mathrm{Q4}}$ in (6.24)) is sufficient to capture the planar kinematics. Also plotted in the figure is the constraint function value at the various values of α tested.

Figure 6.8 depicts the optimal topologies corresponding to each point in Figure 6.7. Clearly, the optimal topology calculated using the Q4α element and the Q4γ elements are (visually) identical for the range of α tested. The indication is, therefore that Q4γ elements are reliable in membrane topology optimization problems over a wide range of α values. Furthermore, the actual value of compliance resulting from these optimal topologies is stable over a wide range of α values. An element with $\alpha = 0$ can be shown to be rank deficient and cannot always be relied upon to deliver accurate results. Nevertheless, for completeness this problem is evaluated for $\alpha = 0$, and satisfactory results are still found.

Readers interested in the convergence histories for the topologies depicted in Figure 6.8 are referred to Appendix B.1.1.

6.5.2 Analysis of membrane results

Based on the membrane example presented, a number of remarks can be made:

(a) Q4α element. (Same for all α.)

(b) Q4γ element, $\alpha = 0$.

(c) Q4γ element, $\alpha = 10^{-6}$.

(d) Q4γ element, $\alpha = 10^{-4}$.

(e) Q4γ element, $\alpha = 10^{-2}$.

(f) Q4γ element, $\alpha = 10^{0}$.

(g) Q4γ element, $\alpha = 10^{2}$.

Figure 6.8: Optimal topologies of MBB beam for various values of α.

- For membrane problems, Q4α and Q4γ elements produce almost identical topologies.
- As expected, the optimal topologies computed with Q4α elements are not a function of the adjustable parameter α, for 2-D planar problems.
- The optimal topologies calculated using Q4γ elements are insensitive to scaling parameter α over a wide range of values.
- The actual value of compliance (objective function value) of the optimal topologies generated with Q4γ elements are relatively insensitive to the numerical value of α over the range tested.

6.5.3 Plate examples

In order to determine the sensitivity of optimal topologies calculated using various plate elements and the SIMP method, a number of popular plate benchmark problems are considered. Additionally, a new problem which demonstrates the deficiencies associated with SRI is proposed. The geometry, material properties and support conditions for the plate example problems are depicted in Figure 6.9.

Both thick and thin plates are studied, with various layer models, i.e. single layer (see Figure 6.2(a)), rib stiffened design (as in Figure 6.2(b)) and honeycomb design (schematically depicted in Figure 6.2(c)). Each of these problems is analyzed using Discrete Kirchhoff Quadrilateral (denoted DKQ) elements, Mindlin-Reissner based elements with selective reduced integration on shear terms (denoted SRI) and Mindlin-Reissner based elements with assumed natural strain interpolations (denoted here as ANS) elements.

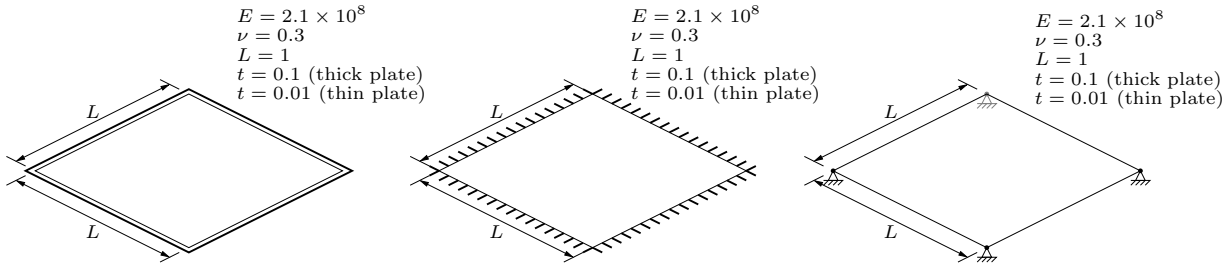

(a) Simply supported square plate subjected to center point load.

(b) Clamped square plate subjected to center point load.

(c) Corner supported square plate subjected to center point load.

Figure 6.9: Example plate problems, geometry and constraints.

In each of the multilayer examples to follow, the layup comprises three layers, with layers 1 and 3 (the outer layers) having thickness $\frac{t}{4}$ and a center layer with thickness of $\frac{t}{2}$ where t is the total thickness of the laminate. For the thick plates, thickness is set to $t = 0.1$ and for the problems considering thin plates $t = 0.01$ is used. These aspect ratios are in line with those used by Zienkiewicz and Taylor [22] to classify thick and thin plates.

In each plate example, the problem symmetry is exploited by modeling only a quarter of the plate using 900 square elements in total (i.e. a discretization of 30×30). Again, although only a quarter of the structure is modeled, the full topology is reported. The available volume for the volume constraint is set, in each case, to half of the design volume (i.e. the sum of the volume of the design layers).

Simply supported plate with center point load

The geometry and constraints for the first plate problem are depicted in Figure 6.9(a). The problem consists of a square plate which is simply supported, and subjected to a unit point load applied to the center of the plate. For brevity, only the single layer results will be detailed in this section. Interested readers are referred to Appendix B.2.1 which contains the results for the multilayer material models.

The compliance, together with the corresponding optimal topologies are plotted as a function of plate thickness for the three different plate elements used in the study. Figure 6.10(a) depicts the compliance as a function of plate thickness plotted on a log-log scale for the three different plate elements. From Figure 6.10(a) it was confirmed that the DKQ optimal compliance results, follow a cubic trend almost exactly with only slight variations due to numerical noise and truncation. Furthermore, Figure 6.11 confirms that the DKQ optimal topologies are insensitive to plate thickness.

Figure 6.10(b) depicts the results on a linear scale, normalized with respect to the (cubic) DKQ results. At the thin plate limit (t=0.01), very little difference is observed between the compliance of the different designs. From this figure, it is clear that the SRI plate

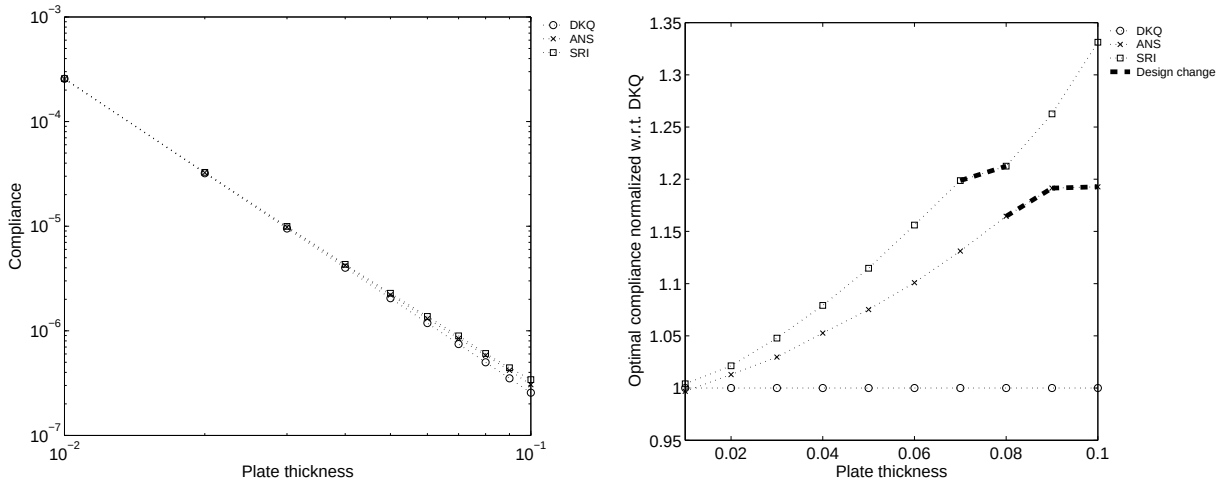

(a) Compliance on log-log scale.

(b) Compliance normalized with respect to DKQ's cubic relation.

Figure 6.10: Optimal topology compliance as a function of plate thickness for the simply supported plate problem.

element is less stiff than the ANS element since higher values of compliance are computed at each thickness, even when topologies are similar. Also indicated on the figure are the thickness ranges over which design changes occur, corresponding to the changes in the slope of the curve. In both cases the design is significantly changed when the compliance of the structure is approximately 1.2 times that of the DKQ result. Since the slope of the SRI curve is greater than that of ANS, this point is reached at a lower thickness for the SRI element and does not occur as gradually as the ANS element. Figure 6.11 depicts the actual topologies corresponding to the points on the curves in Figures 6.10(a) and 6.10(b).

The conclusion is therefore that the differences in topology resulting from SRI and ANS elements, is due to the SRI element being 'softer' (in transverse shear) than the ANS element. Since the bending terms are identical, the softer shear terms of the SRI elements offer less resistance and therefore relatively more strain energy is accommodated by these terms.

Clamped plate with center point load

The geometry for this problem is depicted in Figure 6.9(b). The load considered is again a unit point load applied to the center of the plate. This problem has been considered by a number of authors [4, 115], and our thin plate results compare favorably with theirs.

Results similar to those found for the simply supported plate with centre point load are found for this problem. Therefore, since no real insight is gained through presentation of these results, interested readers are simply referred to Appendix B.2.2. However, the results presented in Appendix B.2.2 are significant in that they are similar to those presented by

previous works that have considered this problem, e.g. Krog and Olhoff [115] and therefore confirm the correctness of our model and optimization routine.

Corner supported plate with center point load

The final plate geometry with restraints is depicted in Figure 6.9(c). It represents a corner supported plate (i.e. transverse displacement is constrained at the four corner nodes only). For this problem, the first load case considered, is again a center point load as before. The single layer, ribbed and honeycomb material models are again analyzed. Once again for brevity only selected results are presented in this section, with the results from the remaining material models and plate thicknesses given in Appendix B.2.3. In particular, only results for the thin ribbed material model are presented.

The tables accompanying each figure, tabulate the difference in compliance between the optimal topologies, analyzed using the three plate elements utilized in this study. The values represent the percentage difference between the compliance of the optimal topology computed with a given element, and the compliance calculated using the remaining two elements. Of course, there is no difference between the compliance of the optimal topology calculated with any element and itself, accounting for the zero terms on the diagonal of each table.

Figure 6.12 depicts the results for the thin ribbed model subjected to a center point load. Although all optimal topologies are similar, the convergence history of using SRI elements, depicted in Figure 6.12(f) indicates that some numerical problems occurred. In fact, during iteration 73 elements with negative compliance (or positive compliance sensitivity) were encountered. Table 6.1 confirms that there is not a significant difference between the various optimal topologies.

	Optimal topology generated using:		
	DKQ	ANS	SRI
Analysed with DKQ	0.0000	-0.0088	1.5140
Analysed with ANS	0.0281	0.0000	1.3180
Analysed with SRI	-0.4786	-0.5854	0.0000
Constraint value	-3.3392e-05	1.5709e-05	-2.9578e-05

Table 6.1: Percentage difference: Corner supported square plate subjected to center point load, ribbed model, $t = 0.01$.

Corner supported plate subjected to uniform distributed load

In the previous plate problems which have been presented there appears to be little or no difference between the results computed using the ANS and SRI Mindlin-Reissner based elements. A problem is now tested for which SRI is known to have difficulty solving [133].

In this problem the same corner supported geometry and restraints, depicted in Figure 6.9(c), are used but the applied load in this case is uniformly distributed over the plate

surface. In order to ensure that the load is not design dependent, only the ribbed and honeycomb material models are considered. Again, to illustrate, results are shown only for the thin ribbed material model (similar to the previous example), while the results of the other material models are contained in Appendix B.2.4.

Figure 6.14 demonstrates that the optimal topologies calculated using the DKQ and ANS elements are, once again, similar. The convergence history of the SRI element depicted in Figure 6.14(f) is extremely erratic due to the element instability. Indeed, many iterations resulted in elements with slightly negative or near zero compliance. As a result, the optimal topology calculated using SRI elements is completely different to the other two elements results. Table 6.2 emphasizes that the compliance of the DKQ and ANS topologies, computed using SRI elements, is completely spurious. In order to explain this, the displaced shape of the optimal topology generated using DKQ elements, analyzed using SRI elements is plotted in Figure 6.13. The hourglass mode which is known to propagate through SRI meshes can clearly be seen.

	Optimal topology generated using:		
	DKQ	ANS	SRI
Analysed with DKQ	0.0000	0.2396	79.4795
Analysed with ANS	-0.0308	0.0000	79.1851
Analysed with SRI	3583.5656	921450354.1646	0.0000
Constraint value	-2.4021e-05	1.6275e-05	6.2786e-05

Table 6.2: Percentage difference: Corner supported square plate subjected to uniform distributed load, ribbed model, $t = 0.01$.

6.5.4 Analysis of plate results

For the results which have been presented in this section, a number of observations and remarks can be made:

- Since the DKQ element is shear rigid, it is not capable of distinguishing between thick and thin plate topology optimization problems. As a result, identical topologies result for any plate thickness.
- The ANS elements have been shown to be reliable and stable. They are capable of reproducing thin plate results similar to those computed using DKQ elements, but are also sensitive to plate thickness.
- The SRI plate element is 'softer' than the ANS element in transverse shear. The SRI element is therefore more sensitive to plate thickness than the ANS elements. The result is that occasionally this sensitivity to thickness drives the SRI element to better designs than that of the ANS or DKQ elements. However, the fact that the SRI element possesses a communicable spurious mode makes it an unreliable element in certain circumstances.

- In cases where SRI elements manifest the propagating spurious mode, the actual topology calculated using SRI elements is not of concern. The conclusion is that there are cases (even in linear static problems) for which SRI is not suitable. Therefore, the use of SRI elements with no hourglass control is not recommended in topology optimization.
- Finally, the correctness of the thick plate results should be tested with an analysis of solid slab-like structures. However, the purpose of this work is simply to show that the thin and thick plate results differ.

6.5.5 Shell examples

Finally, some results for the analysis of thin shell examples are presented. The flat shell elements are constructed as an assemblage of the two membrane elements presented in Section 6.4.1, and the DKQ plate element presented in Section 6.4.2. Since the effect of plate formulation on optimal topologies has already been demonstrated, the effect of membrane component, and especially the inclusion of drilling DOFs, in shell elements is now studied. Therefore, in order to ensure that the results are not a function of the plate formulation, only shell elements with shear rigid plate components are evaluated. It is thereby guaranteed that only thin shell results are recovered, since DKQ elements have just been shown to be insensitive to plate thickness.

Two problems are presented, the first being a cylindrical shell example, which has been studied by several authors [116, 134]. The second problem, with geometry in the shape of a pretwisted beam, is introduced here to highlight the element dependenceny of optimal shell topologies.

Cylindrical shell

The first shell problem is depicted in Figure 6.15. The geometry, restraints, applied loads and material properties are all depicted in the figure. The symmetry of the problem is exploited by only modeling one quarter of the structure with a 30×30 discretization. A volume constraint of half of the design volume is again imposed. Once again, for brevity only single layer results are presented with ribbed and honeycomb results presented in Appendix B.3.1.

Figure 6.16 depicts the optimal compliance values for the single layered material model, as a function of scaling parameter α (see (6.25) for the Q4α membrane component and (6.30) for the Q4γ component). The row of encircled topologies represent the optimal topologies generated using the Q4αDKQ element at each value of α. Above these, are depicted the optimal topologies at the same α value, calculated using Q4γDKQ elements.

Figure 6.16 illustrates that distinctly different topologies are recovered for relatively high values of α, i.e. $\alpha = 1$ and $\alpha = 100$, when the Q4αDKQ element is employed in the finite element analysis. On the other hand, the optimal topologies generated using Q4γDKQ elements are shown to be insensitive to the scaling value of α. The figure also shows that the actual value of compliance is far more sensitive to α when using Q4αDKQ elements than Q4γDKQ elements. The notable decrease in compliance at high values of α, when using

Q4αDKQ elements, is due to the artificially high stiffness of the drilling DOFs which, due to the curvature, is propagated through the structure.

Pretwisted shell

The final shell example is depicted in Figure 6.17. The problem is that of a pretwisted beam, which is clamped at the root, with two point loads applied at the vertices opposite the fixed end. The full geometry is modeled with a 40×40 discretization. A volume constraint of half of the design volume is imposed. For brevity, only the single layer results will be presented. This problem has previously been shown to be sensitive to the value of α [135].

Figure 6.18 depicts the optimal topologies employing Q4αDKQ and Q4γDKQ elements together with the corresponding optimal topologies. For this problem, the range of values of α for which the Q4αDKQ and Q4γDKQ elements result in similar topologies is much smaller than the cylindrical shell problem. In fact, values of $\alpha = 10^{-6}$, 10^{-4} and 10^{2}, each result in different topologies when the finite element model employs Q4αDKQ elements! In contrast, the Q4γDKQ element is once again shown to be stable for all tested values of α.

6.5.6 Analysis of shell results

Based on the results presented in this section the following remarks are appropriate:

- The optimal topologies computed using Q4γDKQ elements are shown to be insensitive, over a wide range, to the scaling value of α. In fact, the only perceivable difference in compliance over the range of tested values of α is a result of the slight difference in volume.

- In contrast, the optimal topologies resulting from the use of the Q4αDKQ elements are shown to be a function of α, and that the sensitivity to α appears to be problem dependent. Authors [17] suggests that if the *ad hoc* correction for absence of drilling DOFs (as in the membrane part of the Q4αDKQ) is made, that a value should be chosen which is small enough not to affect the finite element analysis, while being large enough to alleviate any spurious modes. It is shown here that even if a small value of α is selected, preventing numerical instabilities, different topologies result from those calculated from elements with true drilling DOFs. In fact, the only tested value of α which consistently results in the same results as the Q4γDKQ element is 10^{-2}.

6.6 Conclusions

Numerical experiments have been performed in order to determine the effect of finite element formulation on membrane, plate and shell topology optimization problems. It is shown that, for given topology optimization algorithmic settings, the resultant optimal topology is a function of the element type. It should be noted however, that 'optimal' topologies are known to be a function of the algorithm settings [116]. Therefore, the global optimal topologies

of the evaluated problems are not necessarily reported here. Having said that, optimal topologies presented herein closely resemble previously reported results, where comparison is possible. The implication of this study is therefore that the global optimal topology for a given problem could be a function of the type of element which is used in the analysis.

For membrane problems, it is demonstrated that both standard Q4 (Q4α) and element with drilling degrees of freedom (DOFs) (Q4γ elements) results in identical optimal topologies. The Q4γ elements are shown to be largely insensitive, over a large range of values, to the penalty parameter which enforces the definition of in-plane rotation in terms of in-plane displacements.

The plate examples presented confirmed that, since the DKQ element is shear rigid, optimal topologies computed using these elements are not sensitive to plate thickness. Elements employing an Assumed Natural Strain (ANS) formulation are shown to be robust and reliable. The ANS elements consistently recovered thin plate results similar to the DKQ results. Mindlin-Reissner elements with Selective Reduced Integration (SRI) on transverse shear terms are shown to be 'softer' in transverse shear than the ANS Mindlin-Reissner based elements and are therefore more sensitive to plate thickness. However, the SRI element possesses a spurious communicable mode which occasionally renders this element unstable. A plate example is introduced which exemplifies this problem.

Finally, the effect of parameters related to drilling DOFs of shell problems are studied. It is shown that optimal topologies computed with elements with drilling degrees of freedom based on sound mathematical theory are insensitive to the penalty parameter over a wide range. On the other hand, elements with an *ad hoc* treatment of drilling degrees of freedom are found to be far more sensitive to adjustable parameters. This sensitivity to the adjustable parameter is a furthermore shown to be problem dependent. A new shell example, in the form of a pretwisted beam, is introduced to highlight this dependence.

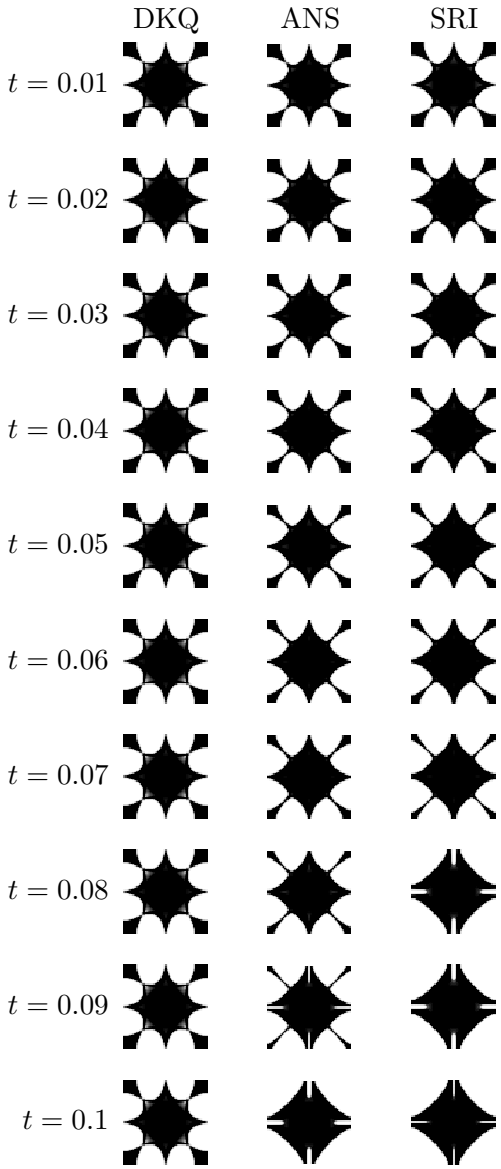

Figure 6.11: Optimal topologies of a simply supported plate subjected to center point load for various plate thicknesses, computed using different plate elements.

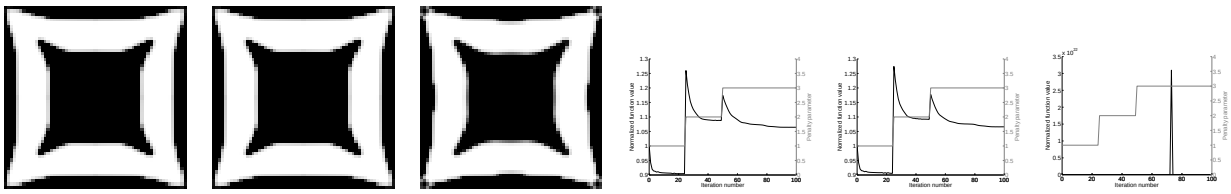

(a) DKQ. (b) ANS. (c) SRI. (d) DKQ. (e) ANS. (f) SRI.

Figure 6.12: Optimal topologies of a corner supported square plate subjected to center point load, ribbed model, $t = 0.01$: (a)-(c) optimal topologies, (d)-(f) convergence histories.

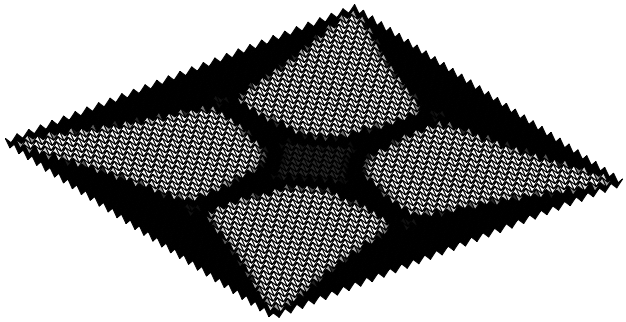

Figure 6.13: Optimal topology, computed using DKQ, of the corner supported plate subjected to distributed load with thin ribbed material model: Displaced shape analyzed using SRI elements, amplification factor 3×10^{-10}.

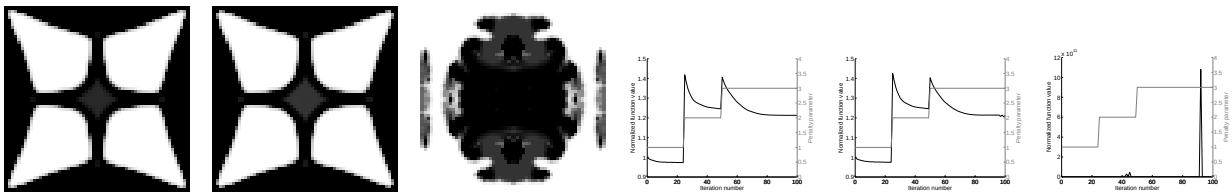

(a) DKQ. (b) ANS. (c) SRI. (d) DKQ. (e) ANS. (f) SRI.

Figure 6.14: Optimal topologies of a corner supported square plate subjected to uniform distributed load, ribbed model, $t = 0.01$: (a)-(c) optimal topologies, (d)-(f) convergence histories.

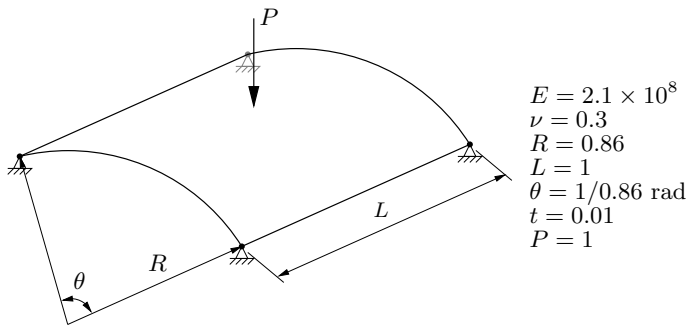

Figure 6.15: Corner supported cylinder geometry and constraints.

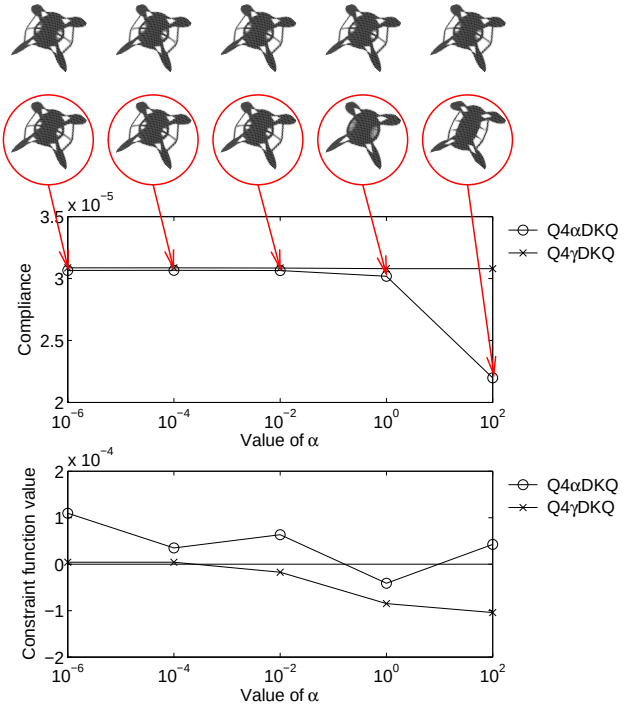

Figure 6.16: Optimal topologies of a corner supported cylinder with single layer material model. Above are the optimal topologies solved employing the standard Q4γDKQ element. On the second row are the optimal topologies employing Q4αDKQ for various values of scaling factor α. Also shown are the optimal function and constraint values for various values of scaling factor α.

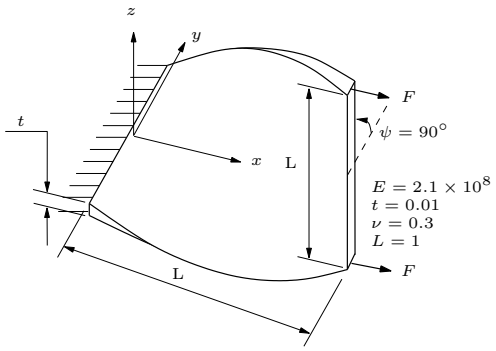

Figure 6.17: Pretwisted beam geometry and constraints.

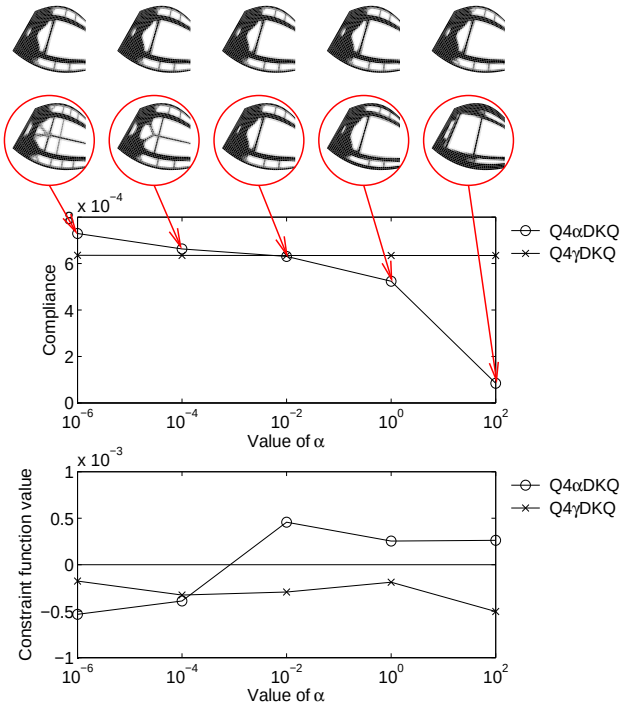

Figure 6.18: Optimal topologies of a pretwisted beam with single layer material model. Above are the optimal topologies solved employing the standard Q4γDKQ element. On the second row are the optimal topologies employing Q4αDKQ for various values of scaling factor α. Also shown are the optimal function and constraint values for various values of scaling factor α.

Chapter 7

Effect of reduced order integration schemes and elements with in-plane rotations on checkerboard patterns in topology optimization

7.1 Summary

In this chapter, the effect of different planar element formulations on the stiffness of a checkerboard patch of elements is investigated. Standard 4-node bilinear elements (Q4) as well as 4-node elements with drilling degrees of freedom (Q4X) are considered. Furthermore, the effect of reduced order integration schemes on quadratic Q8 and Q9 elements is examined. Employing a reduced 4-point integration scheme in elemental calculations of higher order elements leads to the introduction of spurious zero-energy modes, some of which are communicable. Here, it is shown how modified reduced order integration schemes suppress spurious modes, while simultaneously reducing the stiffness of a checkerboard patch of elements, thereby making checkerboarding unlikely in topology optimization applications. It is finally also shown how this reduced stiffness allows for the use of a larger penalty parameter in the SIMP material parameterization, making intermediate densities unattractive without risking the formation of checkerboard material layouts.

7.2 Introduction

Topology optimization has seen a resurgence in popularity in recent times, largely credited to the paper of Bendsøe and Kikuchi [107]. This increased research interest has led to many significant advances and has seen the use of topology optimization in a number of applications and fields. Examples include minimum compliance problems (against which most new procedures and theories are benchmarked) [109, 110], vibration problems [104, 136], compliant mechanism design [100, 137] and even multiphysics problems [106, 138].

However it was accepted relatively early on, during this recent progress, that there are several numerical issues which need to be carefully dealt with in order to achieve sensible results [14]. One of the numerical issues that has received significant attention is the problem of checkerboarding. Checkerboarding is characterised by a significant part of the material layout, forming a checkerboard pattern. That is, if the finite element method is employed and elemental densities are graphically represented on a finite element mesh, the resulting pattern is reminiscent of a checkerboard.

It is pertinent at this stage to emphasise that topology optimization is a challenging global optimization problem. It should therefore be qualified that, although checkerboarding is accepted as being a physical phenomenon, the severity of checkerboarding is dependant on a number of factors, including: optimization algorithm type and settings (such as step limit), objective function (checkerboarding is less prevalent in compliant mechanism design than minimum compliance problems), starting point, as well as problem discretization and, in the SIMP environment, whether or not continuation methods are applied or not. Furthermore, there have been numerous schemes suggested to eliminate checkerboarding from a design generated using topology optimization. Examples include [15, 98] as well as many of the restriction methods detailed in Appendix A. These schemes naturally also have an effect on the checkerboarding severity.

The checkerboarding problem was studied in detail by especially Jog and Haber [102] and Díaz and Sigmund [14]. By interpreting the layout problem as a mixed variational problem in density and displacement, Jog and Haber attribute this problem to a violation of the Babuska-Brezzi or LBB condition. Unfortunately, as reported by Díaz and Sigmund [14], the conditions under which the standard Babuska-Brezzi arguments are applied to mixed variational problems are not met by the layout optimization problem [139].

A different approach was adopted by Díaz and Sigmund. They suggest that the pattens can be explained on the basis of local behaviour. They show that numerical approximations introduced by the finite element method may, under certain circumstances, cause material arranged in a checkerboard fashion to appear artificially stiff. Under these conditions a local arrangement in a checkerboard-like fashion appears to be locally stiffer than any other arrangement of the two constitute materials with the same volume.

Díaz and Sigmund found that quadratic Q9 elements are less likely to checkerboard than standard bilinear Q4 elements. However, the numerical stability of higher order elements (such as Q8 or Q9) comes at a price. They are numerically more expensive than lower order (Q4) elements due to lower connectivity of Q4 elements. Nevertheless, with the advent of ever increasing computing power, this additional expense may become less significant in future. It is therefore still of interest to study the use of higher order elements to alleviate checkerboarding in topology optimization problems. The work of Díaz and Sigmund is built upon here, by exploring the use of reduced order integration schemes in higher order elements in order to further reduce the stiffness of a checkerboard patch of elements.

In the earlier days of the development of the finite element method, numerical integration schemes attracted significant attention (e.g. see [54, 86, 87, 88]), possibly due to the limitations of the computing devices available at the time.

Reduced integration schemes are less numerically expensive than higher order schemes. This

saving in computational effort on the element level comes at the expense of integration accuracy. However, the induced integration error is often on higher-order terms, which in some instances actually enhances finite element accuracy. In summary, reduced integration may be able to simultaneously reduce cost, reduce accuracy in the evaluation of integration expressions, and increase the accuracy of the finite element analysis. This principle was recently successfully applied by Long and Groenwold [140] who applied modified reduced order quadratures to quadratic Q8 and Q9 elements (see also Chapter 4).

It is well known that quadratic elements are less susceptible to checkerboarding than standard bilinear elements. Since planar elements with drilling degrees of freedom (DOFs) are based on a quadratic 'parent element', the stiffness of a checkerboard arrangement of elements with drilling DOFs is also briefly investigated.

This chapter is set out as follows: In Section 7.3 the modified numerical integration schemes employed in this study are briefly described. Section 7.4 presents a very brief discussion of element formulations with drilling degrees of freedom. The theory used by Díaz and Sigmund to estimate the stiffness of a checkerboard patch is summarised in Section 7.5. In Section 7.6 the numerical results of employing reduced order integration on elements with drilling degrees of freedom, and on higher order elements such as Q8 and Q9, are presented. Finally, conclusions are drawn in Section 7.7.

7.3 Modified reduced order quadrature integration rules

Reduced integration is frequently used in evaluating the element stiffness matrix of quadratically interpolated finite elements. Typical examples are the serendipity (Q8) and Lagrangian (Q9) membrane finite elements, for which a reduced 2×2 Gauss-Legendre integration rule is frequently used, as opposed to full 3×3 Gauss-Legendre integration. This 'softens' these element, thereby increasing accuracy, albeit at the introduction of spurious zero energy modes on the element level. This is in general not considered problematic for the 'hourglass' mode common to Q8 and Q9 elements, since this spurious mode is non-communicable. The remaining two zero energy modes occurring in the Q9 element are indeed communicable. However, in topology optimization for instance, conditions may arise where the spurious mode associated with the Q8 element becomes activated. To effectively suppress these modes altogether in elements employing quadratic interpolation fields, two modified quadratures have been employed [140]. As compared to fully integrated elements, the new rules enhance element accuracy due to the introduction of soft, higher-order deformation modes. For completeness, some detail regarding the schemes employed is presented. For further detail, the reader is referred to Chapter 4 and [140].

7.3.1 Numerical integration schemes

The schemes proposed in this section were originally proposed by Dovey [54]. Consider the area integral given by

$$I = \int_{-1}^{1} \int_{-1}^{1} F(r,s) \, \mathrm{d}r \, \mathrm{d}s, \tag{7.1}$$

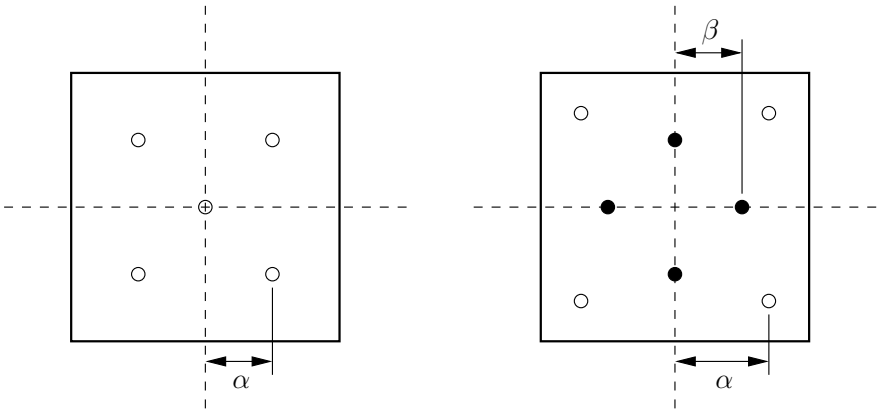

(a) 5-point scheme. (b) 8-point scheme.

Figure 7.1: Modified reduced order integration schemes.

where $F(r,s)$ is any polynomial function of r and s. Any polynomial expression of two variables can be expressed in the form

$$F(r,s) = \sum_{i,j} A_{ij} r^i s^j. \tag{7.2}$$

No limits are placed on the summation indices i and j as any arbitrary polynomial is being considered.

Let any N-point numerical integration rule be written as

$$I^* = \sum_{n=1}^{N} W_n F(r_n, s_n), \tag{7.3}$$

where I^* represents the numerical approximation to I. Integration point n is given by (r_n, s_n) and the associated weight is given as W_n.

Each term of (7.2) may be trivially integrated as follows:

$$\int_{-1}^{1}\int_{-1}^{1} A_{ij} r^i s^j \, dr ds = \begin{cases} \frac{2^2 A_{ij}}{(i+1)(j+1)} & i,j \text{ both even} \\ 0 & \text{otherwise} \end{cases} \tag{7.4}$$

Based on this exact integral, numerical approximations are proposed with leading error terms related to ever higher exponents.

7.3.2 A five-point rule

The 5-point rule is depicted in Figure 7.1(a). Due to symmetry, the weights W_α are identical. The rule is indicated by

$$I^* = W_0 F(0,0) + W_\alpha F(\pm\alpha, \pm\alpha). \tag{7.5}$$

The second term of (7.5) indicates four points when all combinations of positive and negative signs are taken. Now, combining (7.2) and (7.3), comparing with (7.4) and grouping terms including A_{00}, A_{20} and A_{02} and disregarding the centre weight (refer to Chapter 4 for details for details) leads to:

$$\alpha = 1/\sqrt{3}; \quad W_\alpha = 1 \quad \text{and} \quad W_0 = 0, \tag{7.6}$$

which is identical to the 2×2 Gaussian product rule. However, the center point may be retained by selecting a value for W_0 and computing W_α and α.

The scheme is now defined by

$$W_\alpha = 1 - W_0/4, \tag{7.7}$$

$$\alpha = \left(\frac{1}{3W_\alpha}\right)^{\frac{1}{2}}. \tag{7.8}$$

The scheme only has physical meaning while $0 \leq W_0 < 4$. The error in the A_{22} term is minimized as $W_0 \rightarrow 0$. In practice this implies that the 5-point scheme converges to the 2×2 Gaussian scheme as $W_0 \rightarrow 0$. It was however, shown by Long and Groenwold that it is preferable if W_0 is chosen such that $0 \leq W_0 \leq \frac{8}{3}$.

7.3.3 An eight-point rule

The 8-point rule is depicted in Figure 7.1(b). The rule is described by

$$I^* = W_\alpha F(\pm\alpha, \pm\alpha) + W_\beta \left[F(\pm\beta, 0) + F(0, \pm\beta)\right]. \tag{7.9}$$

As demonstrated in Chapter 4, the four equations associated with A_{00}, (A_{02} and A_{20}), A_{22} and (A_{04} and A_{40}) may be satisfied simultaneously and the solution is

$$\alpha = \sqrt{7/9}; \quad W_\alpha = 9/49; \quad \beta = \sqrt{7/15}; \quad W_\beta = 40/49. \tag{7.10}$$

This rule gives the same order of accuracy as the 3 x 3 Gaussian rule. A scheme of lower accuracy is defined by

$$W_\alpha = 1 - W_\beta, \tag{7.11}$$

$$\alpha = \left(\frac{1}{9W_\alpha}\right)^{\frac{1}{4}}, \tag{7.12}$$

$$\beta = \left(\frac{2/3 - 2W_\alpha\alpha^2}{W_\beta}\right)^{\frac{1}{2}}. \tag{7.13}$$

In this case both α and β are restricted to be between 0 and 1. This implies that W_β be chosen such that $0 < W_\beta < \frac{8}{9}$.

7.4 Elements with drilling degrees of freedom

In this section, a very brief account of formulations for elements with drilling degrees of freedom is presented. These membrane elements account for in-plane rotations based on a continuum mechanics definition of rotation. The approach relies on a variational formulation employing an independent rotation field, as presented by Hughes and Brezzi [18]. It utilizes the skew-symmetric part of the stress tensor as a Lagrange multiplier to enforce equality of independent rotations and the skew-symmetric part of the displacement gradient in a weak sense. The stress tensor is therefore not *a priori* assumed to be symmetric.

Hughes and Brezzi show that a displacement-based functional can be derived by eliminating the skew-symmetric part of stress from a mixed-type functional. Employing a matrix notation similar to that in [22], the result is the modified functional

$$\Pi_{\mathrm{m}}^{\mathrm{Q4}\gamma}(\boldsymbol{u}_{\mathrm{m}},\theta_z) = \frac{1}{2}\int_V \boldsymbol{\epsilon}_{\mathrm{m}}{}^T \boldsymbol{C}_{\mathrm{m}}\boldsymbol{\epsilon}_{\mathrm{m}}\mathrm{d}V + \frac{1}{2}\gamma\int_V(\omega_{xy}-\theta_z)^2\mathrm{d}V - \frac{1}{2}\int_V \boldsymbol{u}_{\mathrm{m}}{}^T\boldsymbol{f}\mathrm{d}V, \tag{7.14}$$

where ω_{xy} is the rotational part of the displacement gradient, given by

$$\omega_{xy} = \frac{\partial v}{\partial x} - \frac{\partial u}{\partial y}. \tag{7.15}$$

In the foregoing, $\boldsymbol{\epsilon}_{\mathrm{m}}$ represents the membrane strains, $\boldsymbol{C}_{\mathrm{m}}$ the membrane constitutive matrix, $\boldsymbol{u}_{\mathrm{m}}$ denotes the in-plane membrane displacement field $[u, v]$ and $\boldsymbol{f}$ the body forces.

The independent rotations θ_z, are interpolated using standard bilinear functions, while the in-plane displacement approximation is taken as an Allman-type interpolation [23].

In matrix form the first term of $\Pi_{\mathrm{m}}^{\mathrm{Q4}\gamma}$ can be shown to reduce to

$$\tilde{\boldsymbol{k}}_{\mathrm{m}}^{\mathrm{Q4}\gamma} = \int_A \left[\boldsymbol{B}_{\mathrm{m}}^{\mathrm{Q4}\gamma} \;\; \boldsymbol{G}_{\mathrm{m}}^{\mathrm{Q4}\gamma}\right]^T \boldsymbol{\mathcal{A}} \left[\boldsymbol{B}_{\mathrm{m}}^{\mathrm{Q4}\gamma} \;\; \boldsymbol{G}_{\mathrm{m}}^{\mathrm{Q4}\gamma}\right] \mathrm{d}A, \tag{7.16}$$

where $\tilde{\boldsymbol{k}}_{\mathrm{m}}^{\mathrm{Q4}\gamma}$ is a 12×12 matrix.

The penalty term, in matrix form, corresponding to the second term of $\Pi_{\mathrm{m}}^{\mathrm{Q4}\gamma}$ is derived:

$$\boldsymbol{p}_{\mathrm{m}}^{\gamma} = \gamma\int_A \begin{Bmatrix} \boldsymbol{b}_{\mathrm{m}}^{\mathrm{Q4}\gamma} \\ \boldsymbol{g}_{\mathrm{m}}^{\mathrm{Q4}\gamma} \end{Bmatrix} \left[\boldsymbol{b}_{\mathrm{m}}^{\mathrm{Q4}\gamma} \;\; \boldsymbol{g}_{\mathrm{m}}^{\mathrm{Q4}\gamma}\right] \mathrm{d}A, \tag{7.17}$$

$$\text{where } \gamma = \bar{\gamma}G, \tag{7.18}$$

with G the shear modulus which is a function of the artificial density variable, and $\bar{\gamma}$ an adjustable parameter as in (6.25).

The element stiffness matrix therefore becomes

$$\boldsymbol{k}_{\mathrm{m}}^{\mathrm{Q4}\gamma} = \tilde{\boldsymbol{k}}_{\mathrm{m}}^{\mathrm{Q4}\gamma} + \boldsymbol{p}_{\mathrm{m}}^{\gamma}. \tag{7.19}$$

$\boldsymbol{p}_{\mathrm{m}}^{\gamma}$ is integrated by a single point Gaussian quadrature. By fully integrating $\tilde{\boldsymbol{k}}_{\mathrm{m}}^{\mathrm{Q4}\gamma}$ and combining with $\boldsymbol{p}_{\mathrm{m}}^{\gamma}$, spurious zero energy modes are prevented [21]. No additional devices (e.g. see [24]) are required. The same holds if a modified 8-point quadrature, or 5-point rule [45], is employed to integrate $\tilde{\boldsymbol{k}}_{\mathrm{m}}^{\mathrm{Q4}\gamma}$.

The forms of $\boldsymbol{B}_{\mathrm{m}}^{\mathrm{Q4}\gamma}$, $\boldsymbol{G}_{\mathrm{m}}^{\mathrm{Q4}\gamma}$, $\boldsymbol{b}_{\mathrm{m}}^{\mathrm{Q4}\gamma}$ and $\boldsymbol{g}_{\mathrm{m}}^{\mathrm{Q4}\gamma}$ can be found in, for example [21]. Once again, for more detail regarding these elements, the reader is referred to Chapters 2 and 3.

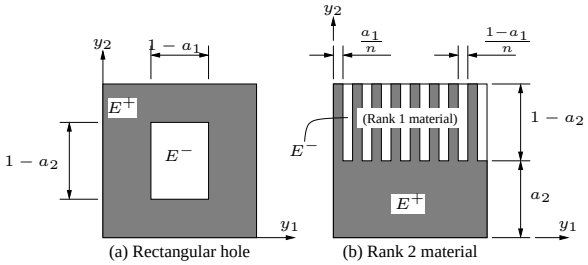

Figure 7.2: Example base cells often used in topology optimization.

7.5 On the stiffness of a checkerboard patch of elements

In this section the essential theory and results of Díaz and Sigmund [14] will be highlighted. Since much of the work presented in this section is based on their work, and in order to ensure continuity for those readers familiar with the work of Díaz and Sigmund, their notation will be used here. This section starts with a short summary of the minimum compliance topology optimization problem using homogenization theory and concludes with the main results from their paper.

7.5.1 Topology optimization using homogenization

Even with todays advanced computing power, a numerical analysis of a composite structure with complex microstructure, is infeasible if the microstructure itself is modelled. A cellular body, made of solids and voids, may be considered a simple such composite material. This is typically the type of material exploited to perform topology optimization.

Homogenization theory can be employed to replace a composite with periodic microstructure, with an effective material model. These materials are usually described in terms of a base cell, the smallest representative unit of material. Homogenization theory allows macroscopic material characterization, based solely on analysis of the microscopic base cell. Evaluation of the base cell can be performed analytically if the base cell is sufficiently simple in structure. Alternatively, a numerical analysis, usually involving the Finite Element Method (FEM), may be called for.

In a topology optimization setting, topology is most frequently described by a continuous density function which effectively transforms the problem into a material distribution problem using composite materials.

In general, the composite (base cell) is made up of a mixture of two isotropic materials, one strong with constitutive tensor E^+, and one weak with constitutive tensor $E^- \ll E^+$. The weak material typically represents a void, allowing admission or removal of holes in the structure.

Examples of two common base cells are depicted in Figure 7.2. The first is a square cell with rectangular hole, see Bendsøe and Kikuchi [107] and the second is a so-called Rank 2

material as studied by, for example Milton and Kohn [141].

The continuous density function, describing the material layout or topology, of these two base cells is given by the ratio of strong material volume to total base cell volume, in terms of cell parameters (a_1 and a_2 in Figure 7.2). The effective constitutive tensor $\bar{E}$, is then sought in terms of cell parameters a_1, a_2 and of course the two isotropic material property tensors E^+ and E^-.

The minimum compliance topology optimization problem consists of finding the material layout which minimises the mean compliance, while maintaining a bound on the amount of strong material:

$$\min_{\rho \in X_M} \min_{a \in X_\rho} f(u^*), \tag{7.20}$$

where $f(u^*)$ is the mean compliance at equilibrium, corresponding to displacement solution u^*.

$$X_M = \left\{ \rho \in L^\infty(\Omega) : \ 0 \leq \rho \leq 1, \ \int_\Omega \rho \ \mathrm{d}x \leq M \right\}, \tag{7.21}$$

where M is an upper bound on the amount of strong material, Ω is the structural domain and ρ is a scalar density function based on unit cell parameters $a = \{a_1, \ a_2\}$. Finally,

$$X_\rho = \left\{ a \in R^2 : \ a_1 + a_2 - a_1 a_2 = \rho, \ 0 \leq a_1, a_2 \leq 1 \right\}. \tag{7.22}$$

It is well known that the minimum compliance topology optimization problem can be cast in the form:

$$\max_{\rho \in X_M} \min_{u \in K} \left\{ \int_\Omega \max_{a \in X_\rho} \ w \ \mathrm{d}x - f(u) \right\}, \ \text{where} \tag{7.23}$$

$$K = \left\{ u^h \in H^1(\Omega) : \ u^h = 0 \text{ on } \Gamma^0 \right\}. \tag{7.24}$$

K represents the set of kinematically admissible displacement fields u and

$$w = \frac{1}{2} \bar{E}(a) \epsilon(u) \cdot \epsilon(u) \tag{7.25}$$

is the strain energy density resulting from strain field $\epsilon(u)$.

The implication of (7.23) is that for fixed density ρ and known strain field $\epsilon(u)$, the optimum local orthotropy is such that strain energy density is maximised [4, 14].

The finite element discretization of the problem in (7.23) can be written as

$$\max_{\rho^h \in X_R^h} \min_{u^h \in K^h} \left\{ \sum_{e=1}^{N} \frac{1}{2} \int_e \max_{a^e \in X_{\rho^e}} \ \bar{E}(a^e) \epsilon(u^e) \cdot \epsilon(u^e) \ \mathrm{d}x - f(u^h) \right\}, \tag{7.26}$$

assuming that Ω can be covered by N square finite elements. The density discretization ρ^h is assumed to be constant within each element e, taking value ρ^e. Standard shape functions $N_\alpha(x)$ are used to construct $u^h \subset K$, where elemental interpolations on element e are given by:

$$u^e = \sum_{\alpha=1}^{n} N_\alpha(x) u_\alpha^e, \ n = \text{number of nodes}, \tag{7.27}$$

and u_α^e are nodal DOFs.

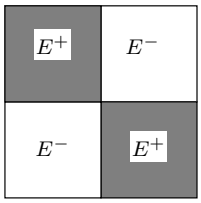

Figure 7.3: Checkerboard patch with average density ρ =1/2.

7.5.2 Effective properties of a checkerboard

Continuing to follow the procedure set out by Díaz and Sigmund, it is now demonstrated how the effective properties of a 'black-and-white' checkerboard patch of finite elements are computed. That is, the material distribution of a patch with average density $\rho = 1/2$. This represents a unit base cell Y which is divided into four equal quadrants Y^i such that $E = E^-$ in $Y^1 \cup Y^3$ and $E = E^+$ in $Y^2 \cup Y^4$, as shown in Figure 7.3.

The homogenized stiffness tensor is computed using the well-known formulae [4, 14, 141, 142, 143] by integration over the base cell area as

$$\bar{E}_{ijkl} = \int_Y \left\{ E_{ijkl} - E_{ijpq}\epsilon^*_{pq}[\chi^{(kl)}] \right\} \mathrm{d}y, \tag{7.28}$$

where the $Y-$periodic test fields $\chi_p^{(kl)}$ are found as the solution to the equilibrium equations

$$\int_Y E_{ijkl} \left\{ \epsilon^*_{pq}[\chi^{(kl)}] - \epsilon^{0^{(kl)}}_{pq} \right\} \frac{\partial v_i}{\partial y_j} \mathrm{d}y = 0, \tag{7.29}$$

for all $v \in V^h$, and $k, l = 1, 2$.

The finite element space V^h contains the same shape functions as those used to approximate the displacement field, defining

$$V^h = \left\{ v(y) \in R^2 : v(y) = N_\alpha(y) v^i_\alpha, \text{ if } y \in Y^i, \ i = 1, \ldots, 4 \right\}, \tag{7.30}$$

and where in the unit base cell, $v(0, y_2) = v(1, y_2)$ and $v(y_1, 0) = v(y_2, 1)$. The effective material tensor, given in (7.28) can be computed after solving (7.29) using three linearly independent test strains $\epsilon^{0^{(kl)}}_{pq}$ as discussed in, for example, [4, 141, 142, 143, 144].

In their paper, Díaz and Sigmund [14] find solutions to (7.28) and (7.29) using analytical integration of the finite element discretization. For an undistorted mesh of elements, this is equivalent to using full numerical integration, i.e. a 4 point Gauss quadrature for standard 4 noded elements and a 9 point scheme for 9 node elements.

They present the optimal strain energy density w^* for a known strain field $\bar{\epsilon}$ and average density $\rho = 1/2$ using: (*i*) rank 2 materials, (*ii*) materials with a base cell described by a rectangular hole, as well as (*iii*) SIMP parameterizations. They then use the foregoing theory to compare these results to the strain energy density calculated using a patch of 4 square elements, as depicted in Figure 7.3 with the same average density and applied strain field.

In particular, for rank 2 materials, it can be shown (see Díaz and Sigmund [14] and Jog *et al.* [145]) that the optimal strain energy density for fixed strain $\bar{\epsilon}$ and density $\rho = 1/2$ is given by:

$$w^*_{\text{Rank2}}(\bar{\epsilon}) = \frac{1}{2} \max_{a^e \in X, \rho^e = 1/2} \bar{E}_{\text{Rank2}}(a)\bar{\epsilon} \cdot \bar{\epsilon}, \tag{7.31}$$

where $\bar{E}_{\text{Rank2}}$ is the effective property tensor of the Rank 2 material and the a's are as depicted in Figure 7.2(b). For a void weak material ($E^- = 0$), $w^*_{\text{Rank2}}(\bar{\epsilon})$ may be expressed analytically (see Díaz and Sigmund [14]). This result is compared to

$$w^*_{\text{Q4}}(\bar{\epsilon}) = \frac{1}{2}\bar{E}_{\text{Q4}}\bar{\epsilon} \cdot \bar{\epsilon}, \text{ and} \tag{7.32}$$

$$w^*_{\text{Q9}}(\bar{\epsilon}) = \frac{1}{2}\bar{E}_{\text{Q9}}\bar{\epsilon} \cdot \bar{\epsilon}, \text{ where} \tag{7.33}$$

$\bar{E}_{\text{Q4}}$ and $\bar{E}_{\text{Q9}}$ are, respectively, the effective constitutive tensor of the 'black-and-white' patch of Q4 and Q9 elements, as depicted in Figure 7.3.

Similarly, for $\rho = 1/2$, the optimal strain energy density for a microstructure with a base cell described by a rectangular hole is given by

$$w^*_{\text{RHole}}(\bar{\epsilon}) = \frac{1}{2} \max_{a^e \in X, \rho^e = 1/2} \bar{E}_{\text{RHole}}(a)\bar{\epsilon} \cdot \bar{\epsilon}, \text{ and} \tag{7.34}$$

and for the SIMP material model,

$$w^*_{\text{SIMP}}(\bar{\epsilon}) = \frac{1}{2}\bar{E}_{\text{SIMP}}(\rho)\bar{\epsilon} \cdot \bar{\epsilon} = \frac{1}{2}\left(\frac{1}{2}\right)^p E^+\bar{\epsilon} \cdot \bar{\epsilon}, \tag{7.35}$$

where $\bar{E}_{\text{RHole}}$ and $\bar{E}_{\text{SIMP}}$ are the associated constitutive tensors. Given the preceding, the following relationships can be proven:

- For rank 2 layered materials (denoted Rank 2),

$$w^*_{\text{Q4}}(\bar{\epsilon}) \geq w^*_{\text{Rank 2}}(\bar{\epsilon}), \tag{7.36}$$
$$w^*_{\text{Q9}}(\bar{\epsilon}) < w^*_{\text{Rank 2}}(\bar{\epsilon}), \tag{7.37}$$

- For a square cell with rectangular hole (denoted RHole),

$$w^*_{\text{Q4}}(\bar{\epsilon}) > w^*_{\text{RHole}}(\bar{\epsilon}), \tag{7.38}$$
$$w^*_{\text{Q9}}(\bar{\epsilon}) < w^*_{\text{RHole}}(\bar{\epsilon}), \tag{7.39}$$

- For SIMP material model (denoted SIMP),

$$w^*_{\text{Q4}}(\bar{\epsilon}) = w^*_{\text{SIMP}}(\bar{\epsilon}), \text{ for } p = 1, \tag{7.40}$$
$$w^*_{\text{Q4}}(\bar{\epsilon}) > w^*_{\text{SIMP}}(\bar{\epsilon}), \text{ for } p > 1, \tag{7.41}$$
$$w^*_{\text{Q9}}(\bar{\epsilon}) < w^*_{\text{SIMP}}(\bar{\epsilon}), \text{ for } p < p^*_1(\nu), \tag{7.42}$$
$$w^*_{\text{Q9}}(\bar{\epsilon}) > w^*_{\text{SIMP}}(\bar{\epsilon}), \text{ for } p > p^*_2(\nu) \tag{7.43}$$

where

$$p_1^*(\nu) = \frac{\log\left(22/(6-5\nu)\right)}{\log(2)}, \text{ and} \tag{7.44}$$

$$p_2^*(\nu) = \frac{\log\left(2(6-5\nu)\right)}{\log(2)}. \tag{7.45}$$

Díaz and Sigmund suggest that checkerboarding is likely to occur if the strain energy density, based on the effective material tensor of a checkerboard patch of elements (e.g. $\bar{E}_{\text{Q4}}$, $\bar{E}_{\text{Q9}}$), is greater than that based on the effective material tensor of the relevant material parameterization (e.g. $\bar{E}_{\text{Rank2}}$, $\bar{E}_{\text{RHole}}$ or $\bar{E}_{\text{SIMP}}$). These relations can therefore be used to, not only explain why checkerboarding occurs, but also in the case of the SIMP material model, to recommend a suitable penalty parameter p.

7.6 Numerical results

In this section, some numerical results of the investigation are presented. Firstly, the effect of finite element formulation on the local χ field is explored qualitatively. Next, effective material properties of a checkerboard patch of elements are computed, employing various elements, and making use of various integration schemes. These effective properties are then used to compute strain energy densities for prescribed straining conditions. Finally, for the SIMP material model, the effects of integration scheme on the bounds of penalty parameter p_1^* and p_2^*, are investigated.

The following elements are considered in this study:

- *Q4*, a standard 4-node displacement based element.
- *Q4X*, a 4-node element with drilling degrees of freedom, based on the formulation presented in Section 7.4.
- *Q8*, the serendipity 8-node element based on the same formulation as Q4.
- *Q9*, the Lagrange 9-node element based on the the same formulation as Q4 and Q8.

The integration schemes evaluated are listed below:

- *4-point Gauss-Legendre scheme*, which is standard for evaluating Q4 elements and exact for undistorted elements. It is also commonly used to evaluate Q8 elements, although it leads to a spurious mode on the elements level.
- *5-point scheme*, with varying center weight W_0, see Section 7.3.2.
- *8-point scheme* with varying W_β, see Section 7.3.3.
- *9-point scheme Gauss-Legendre scheme*, which is the standard in evaluation of the Q9 element matrices and is also commonly used for Q8 elements.

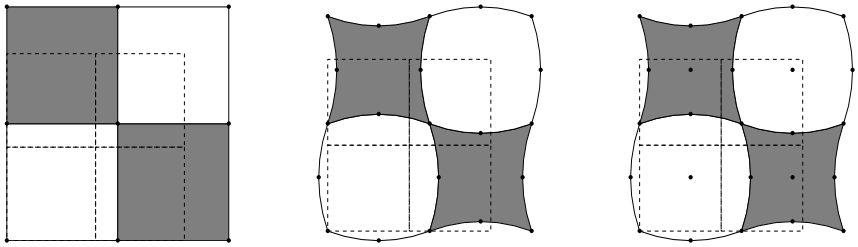

(a) Q4 and Q4X (b) Q8 (c) Q9

Figure 7.4: Local χ fields for various elements resulting from mean strain field $\bar{\epsilon}_{11} = \bar{\epsilon}_{22} = 1$ and $\bar{\epsilon}_{12} = 0$.

7.6.1 Effect of element formulation on local χ field

The solution to the cell problem (7.29) employing Q4 elements has been shown to be extremely simple, e.g. see [14]. The periodic deformation subjected to constant test strain is such that the strain in the patch is constant. That is to say,

$$\epsilon^*[\chi^{(kl)}] = 0. \tag{7.46}$$

To illustrate, the χ field for a patch of Q4 elements subjected to a constant prestrain $\bar{\epsilon}_{11} = \bar{\epsilon}_{22} = 1$, and $\bar{\epsilon}_{12} = 0$, is depicted in Figure 7.4(a).

It is now investigated whether the additional straining modes, associated with Q4X elements, result in non-constant patch strains when subjected to similar test strains. These elements are based on an 8-node parent element employing quadratic Allman-type shape functions as explained in Section 7.4. The side nodes (5-8) are then 'condensed' to the corner nodes (1-4) and related to corner nodal rotations. Q4X elements, therefore possess 3 degrees of freedom per node in total, i.e. 2 in-plane translations and an in-plane rotation.

Unfortunately, as with Q4 elements, only constant patch strains result for Q4X elements. This can be attributed to the fact that, in the solution of the cell problem, the rotational degrees of freedom are not activated by any of the test strains, and therefore neither are the higher order straining modes. The resulting local χ field is thus identical to that of Q4, as depicted in Figure 7.4(a).

In previous work, e.g. see [146] and Section 5.4.2, it has been shown that Q4X elements do in fact yield slightly different results in terms of checkerboarding than Q4 elements. This is probably due to the fact that for realistic problems with complex strain fields, the skew-symmetric part of the displacement gradient becomes non-zero. Under these circumstances Q4X appears to be less stiff than standard Q4 elements, tending to effectively suppress the formation of large areas of checkerboard material layout. To illustrate, Figure 7.5(a) depicts the optimal topology of the MBB beam employing Q4 elements and a ramping strategy to increase penalty parameter p linearly from 1 to 3 in 34 iterations, and held at $p = 3$ for a further 16 iterations after which the solution is terminated. Figure 7.5(b) depicts the results employing the same strategy, but this time employing Q4X elements. Clearly, the severity of checkerboarding is significantly reduced compared to the results employing Q4 elements.

However, in the limit of mesh refinement only constant strains are experienced, and under

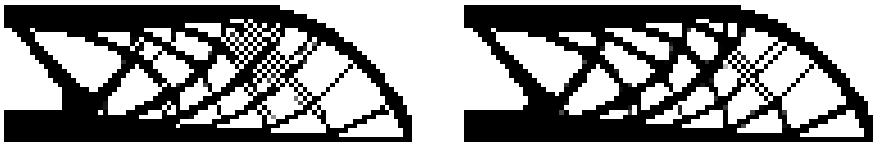

(a) Q4 elements. (b) Q4X elements

Figure 7.5: Optimal topologies of the MBB beam using symmetry and employing (a) Q4 and (b) Q4X elements.

these circumstances (fine meshes) more checkerboarding is expected. Numerical experiments have supported this conjecture. There is therefore no guarantee that Q4X elements will not checkerboard, especially when fine meshes are employed. However, elements with drilling degrees of freedom have been shown to be useful in topology optimization applications for specific problems, e.g. see [146, 77, 147]. Q4X elements are also more accurate and more stable than standard Q4 elements, at only a slight increase in numerical expense.

The local χ fields for Q8 and Q9 elements are distinctly different to those associated with the Q4 and Q4X elements. The material distribution results in nonzero local strain variations as shown in Figures 7.4(b) and (c) respectively.

The local χ fields for the Q8 and Q9 elements, depicted in Figure 7.4, are recognised as having a significant contribution from higher order staining modes. Recently, it has been shown that higher order deflection modes of quadratic elements can be softened by employing reduced order integration schemes. In the next section, these reduced order integration schemes are employed to compute effective material properties of checkerboards with the aim of reducing the strain energy density associated with prescribed strains $\bar{\epsilon}$.

7.6.2 Effect of element selection and integration scheme on effective properties of a checkerboard

A patch of 4 elements, arranged in a checkerboard as depicted in Figure 7.3, is used to determine the effect of element formulation, interpolation and integration scheme on the effective material properties computed using homogenization. In order to compare with results presented by Díaz and Sigmund, their material properties are used in similar calculations for Q4 and Q9 elements. Specifically, the weak material has constitutive tensor

$$E^- = 0, \tag{7.47}$$

and the strong material with constants

$$E^+_{1111} = E^+_{2222} = 1, E^+_{1122} = 0.3, E^+_{1212} = 0.35. \tag{7.48}$$

The variable weights selected for evaluation (for the 5- and 8-point schemes) are based on results presented in Chapter 4, wherein it was shown that employing a very small adjustable weight W could result in numerical instabilities, and therefore the use of values $W < 0.01$ are not recommended. Furthermore, in Chapter 4 settings of $W_0 = 0.1(8/3)$ and $W_\beta = 0.1(8/9)$

were suggested for improved stability and accuracy. It was also shown that a value of $W_\beta = 40/49$ results in a solution identical to employing a full 9-point integration scheme for undistorted elements. Values selected for evaluation are therefore $W_0 = 0.01$ and $8/30$ and $W_\beta = 0.01$, $8/90$ and $40/49$.

Effective material properties for the evaluated elements employing the various integration schemes and weights to solve (7.29) and then (7.28) are presented in Table 7.1.

Undistorted Q4 elements are exactly integrated using a 4 point Gauss quadrature, and all other (higher order in this case) integration schemes yield the same result. The resulting material constants are simply given by the average of the strong and weak material properties since $\epsilon^*[\chi^{(kl)}] = 0$ in (7.28).

A similar result is computed for the patch of Q4X elements, as expected, since Q4 and Q4X elements result in the same χ fields. The result is that the homogenised material properties of Q4X and Q4 are identical. Furthermore, the integration scheme employed has no effect since local strains are all constant. Note however, that employing a 4-point scheme results in a rank deficiency for Q4X elements.

Applying a reduced 4-point integration scheme in elemental calculations of Q8 elements is known to result in one spurious straining mode. For an assembly of 2 or more elements, this mode is largely non-communicable. However, as shown in, for example [17, 60, 140], the mode becomes communicable under certain circumstances, such as when elements are soft-supported (as may be the case in topology optimization applications), or in some dynamic problems (in which Escher modes appear). In the case considered here, the manner in which the two solid elements are connected in the patch (similar to a one-node hinge) also allows the mode to become communicable. In other words, the mode is not prevented from propagating between diagonal elements, since adjacent elements are empty.

Solution of the system of equations in (7.29) under these circumstances is obviously not recommended, due to the rank deficiency of the global stiffness matrix. However, for completeness singularity problems were suppressed in order to compute 'singular results'. Applying the 4-point scheme to the patch of Q8 elements and solving (7.29) and then (7.28) results in a constitutive tensor with all non-zero entries equal. This constitutive matrix is therefore rank deficient, and a strain of $\epsilon = \{\bar{\epsilon},\ \bar{\epsilon}, 0\}$ results in zero stress and therefore zero strain energy. This proves that application of the 4-point scheme in a topology optimization environment employing quadratic elements is not recommended.

The 5- and 8-point integration schemes are further evaluated with the weights suggested by Long and Groenwold [140]. The 5-point integration scheme has been shown, even at the low value of $W_0 = 0.01$, to suppress the spurious mode present when a 4-point scheme is employed. This result is mirrored by the results presented in Table 7.1. Application of the 8-point scheme, naturally also suppresses these modes. As shown in [140], application of the 8-point scheme with weight $W_\beta = 40/49$ yields identical results to a 9-point scheme for undistorted elements.

Identical results are computed when a patch of Q9, instead of Q8, elements are considered. However, application of a 4-point integration scheme to compute the element stiffness matrix of Q9 elements results in 3 spurious zero energy modes, two of which are communicable in an assemblage of elements. As a result, even application of the 5-point scheme results in a rank

deficient global stiffness matrix. Therefore, even though the computed results are similar for Q8 and Q9 elements, Q9 elements can only safely be used with 8- or 9-point integration schemes.

Finally, applying a full (9-point) integration scheme results in identical effective material properties for Q8 and Q9 elements. Since a 9-point scheme represents a full integration scheme for an undistorted quadratic element, the result is identical to solving the expressions analytically. This suggests that there is very little or no advantage in including the hierarchical bubble function, present in Q9 elements, in terms of checkerboarding of undistorted elements. Results for distorted elements may differ however.

7.6.3 Effect of integration scheme on strain energy density of quadratic elements

Since it was shown in Section 7.6.2 that both Q4 and Q4X elements result in identical effective material tensors independent of integration scheme, their results are not considered in this section. Results for Q4 elements may be found in the paper of Díaz and Sigmund [14]. Furthermore, since Q8 and Q9 elements produce identical results, as shown in Table 7.1, only results for Q8 elements will be presented here. Finally, due to the dominance of the SIMP material model in recent years, only results for SIMP will be focused upon in this subsection. However, these results are equally valid for other material parameterizations such as rank 2 materials.

The material parameterization for SIMP is extremely simple, with the equivalent material tensor given by

$$\bar{E}_{\text{SIMP}}(\rho) = \rho^p E^+, \text{ with } p \geq 1. \tag{7.49}$$

The minimum compliance problems can therefore be written as

$$\max_{\rho^h \in X_M} \min_{u^h \in K^h} \sum_{e=1}^{N} \frac{1}{2} \int_e (\rho^e)^p E^+ \epsilon(u^h) \cdot \epsilon(u^h) \mathrm{d}x - f(u^h), \tag{7.50}$$

with relevant space of density

$$X_M = \left\{ \rho \in L^\infty(\Omega) : \ 0 \leq \rho \leq 1, \ \int_\Omega \rho \ \mathrm{d}x \leq M \right\}. \tag{7.51}$$

For the SIMP problem, the strain energy density of a patch with average density ρ can simply be written as

$$w^*_{\text{SIMP}} = \frac{1}{2} (\rho)^p \, E^+ \bar{\epsilon} \cdot \bar{\epsilon}, \tag{7.52}$$

for prescribed strain $\bar{\epsilon}$. It can easily be shown that the strain energy density can be written in terms of principal strains as

$$\frac{w^*_{\text{SIMP}}}{E^+_{1111} \epsilon_I^2} = \frac{1}{2} (\rho)^p \left(1 + 2\nu\eta + \eta^2\right), \tag{7.53}$$

Table 7.1: Effective constitutive terms for different elements employing various integration schemes.

Element	Integration Scheme	Weight	$\bar{E}_{1111}$	$\bar{E}_{2211}=\bar{E}_{1122}$	$\bar{E}_{1211}=\bar{E}_{1112}$	$\bar{E}_{2222}$	$\bar{E}_{1222}=\bar{E}_{2212}$	$\bar{E}_{1212}$
Q4	4pt	–	5.0000e-01	1.5000e-01	-7.6328e-17	5.0000e-01	-6.9389e-18	1.7500e-01
Q4	5pt	$W_0 = 0.01$	5.0000e-01	1.5000e-01	-1.1102e-16	5.0000e-01	-6.9389e-18	1.7500e-01
Q4	5pt	$W_0 = 0.1\frac{8}{3}$	5.0000e-01	1.5000e-01	1.3032e-16	5.0000e-01	-2.6021e-18	1.7500e-01
Q4	8pt	$W_\beta = 0.01$	5.0000e-01	1.5000e-01	1.4658e-16	5.0000e-01	-4.5103e-17	1.7500e-01
Q4	8pt	$W_\beta = 0.1\frac{8}{9}$	5.0000e-01	1.5000e-01	1.6617e-16	5.0000e-01	-1.2040e-18	1.7500e-01
Q4	8pt	$W_\beta = \frac{40}{49}$	5.0000e-01	1.5000e-01	-1.3878e-17	5.0000e-01	0	1.7500e-01
Q4	9pt	–	5.0000e-01	1.5000e-01	-1.9452e-16	5.0000e-01	2.0046e-17	1.7500e-01
Q4X	4pt*	–	5.0000e-01	1.5000e-01	-4.8572e-17	5.0000e-01	3.4694e-17	1.7500e-01
Q4X	5pt	$W_0 = 0.01$	5.0000e-01	1.5000e-01	-2.7756e-17	5.0000e-01	-1.1796e-16	1.7500e-01
Q4X	5pt	$W_0 = 0.1\frac{8}{3}$	5.0000e-01	1.5000e-01	7.6328e-17	5.0000e-01	9.7145e-17	1.7500e-01
Q4X	8pt	$W_\beta = 0.01$	5.0000e-01	1.5000e-01	3.1225e-17	5.0000e-01	4.1633e-17	1.7500e-01
Q4X	8pt	$W_\beta = 0.1\frac{8}{9}$	5.0000e-01	1.5000e-01	1.0061e-16	5.0000e-01	2.7756e-17	1.7500e-01
Q4X	8pt	$W_\beta = \frac{40}{49}$	5.0000e-01	1.5000e-01	-1.0408e-17	5.0000e-01	2.7756e-17	1.7500e-01
Q4X	9pt	–	5.0000e-01	1.5000e-01	-1.0755e-16	5.0000e-01	-1.3878e-17	1.7500e-01
Q8	4pt*	–	1.1375e-01	1.1375e-01	-9.1901e-16	1.1375e-01	-3.1130e-15	1.1375e-01
Q8	5pt	$W_0 = 0.01$	1.1413e-01	1.1391e-01	2.9730e-16	1.1413e-01	1.0847e-16	1.1386e-01
Q8	5pt	$W_0 = 0.1\frac{8}{3}$	1.2428e-01	1.1814e-01	9.5590e-16	1.2428e-01	6.0057e-16	1.1682e-01
Q8	8pt	$W_\beta = 0.01$	1.1420e-01	1.1357e-01	-1.2468e-15	1.1420e-01	1.0146e-17	1.1376e-01
Q8	8pt	$W_\beta = 0.1\frac{8}{9}$	1.1783e-01	1.1211e-01	8.5974e-16	1.1783e-01	6.7693e-17	1.1387e-01
Q8	8pt	$W_\beta = \frac{40}{49}$	1.7184e-01	9.4066e-02	6.9568e-16	1.7184e-01	8.3630e-17	1.1582e-01
Q8	9pt	–	1.7184e-01	9.4066e-02	-5.0362e-16	1.7184e-01	-1.2759e-16	1.1582e-01
Q9	4pt*	–	1.1375e-01	1.1375e-01	2.9343e-17	1.1375e-01	-4.7436e-16	1.1375e-01
Q9	5pt*	$W_0 = 0.01$	1.1413e-01	1.1391e-01	-4.4465e-16	1.1413e-01	2.0281e-16	1.1386e-01
Q9	5pt*	$W_0 = 0.1\frac{8}{3}$	1.2428e-01	1.1814e-01	1.9876e-13	1.2428e-01	7.1124e-14	1.1682e-01
Q9	8pt	$W_\beta = 0.01$	1.1420e-01	1.1357e-01	-1.6860e-15	1.1420e-01	1.4914e-15	1.1376e-01
Q9	8pt	$W_\beta = 0.1\frac{8}{9}$	1.1783e-01	1.1211e-01	3.5281e-16	1.1783e-01	-8.8486e-17	1.1387e-01
Q9	8pt	$W_\beta = \frac{40}{49}$	1.7184e-01	9.4066e-02	-4.1730e-16	1.7184e-01	6.1592e-18	1.1582e-01
Q9	9pt	–	1.7184e-01	9.4066e-02	-6.1712e-16	1.7184e-01	1.2296e-16	1.1582e-01

* Singularity problems suppressed to perform the calulation. Use of this integration scheme is not recommended.

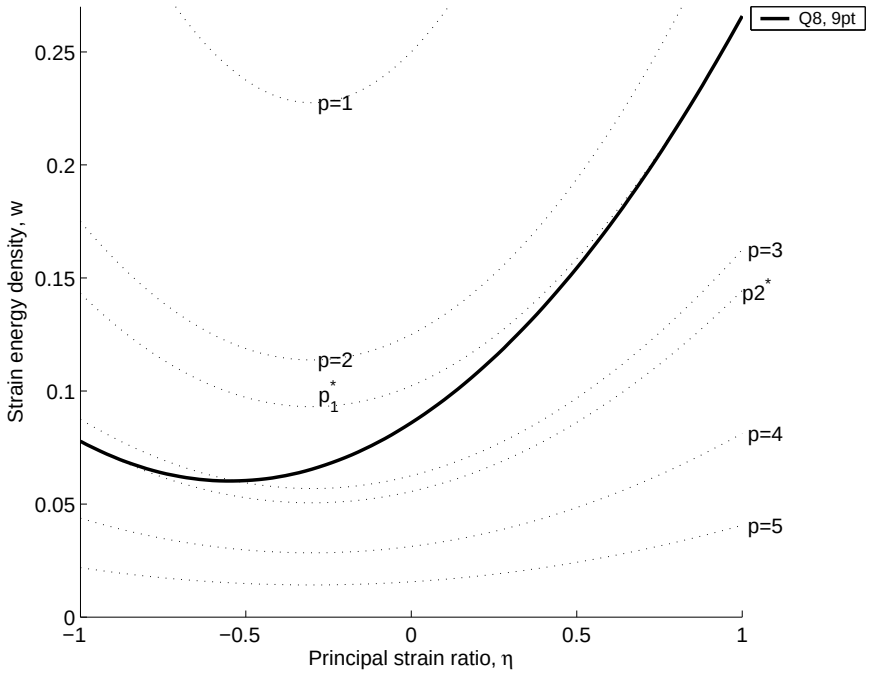

Figure 7.6: Strain energy density of fully integrated Q8 elements.

where η is the principal strain ratio $\eta = \frac{\epsilon_{II}}{\epsilon_I}$, with $|\epsilon_I| \geq |\epsilon_{II}|$, the principal strains.
Comparing this result to expressions for the (analytically or fully integrated) strain energy density of a patch of elements, given by

$$\frac{w^*_{Q4}}{E^+_{1111}\epsilon_I^2} = \frac{1}{4}\left(1 + 2\nu\eta + \eta^2\right), \tag{7.54}$$

for a checkerboard patch of Q4 elements, and

$$\begin{aligned}\frac{w^*_{Q9}}{E^+_{1111}\epsilon_I^2} =& \frac{1}{4}\left[\frac{(47 - 35\nu - 35\nu^2 + 25\nu^3)}{22(6 - 5\nu)} + \right.\\ & \frac{(50 - 26\nu - 70\nu^2 + 50\nu^3)}{22(6 - 5\nu)}\eta + \\ & \left.\frac{(47 - 35\nu - 35\nu^2 + 25\nu^3)}{22(6 - 5\nu)}\eta^2\right],\end{aligned} \tag{7.55}$$

for a patch consisting of Q9 elements, Díaz and Sigmund were able to prove the propositions in (7.40) to (7.43). Díaz and Sigmund conject that if w^*_{SIMP} is less than the strain energy density given by the equivalent patch of elements, checkerboarding is likely to occur.

The strain energy density given in (7.53) is now compared to numerically integrated counterparts of equations (7.54) and (7.55) computed using reduced order integration schemes and Q8 elements.

To illustrate, $w^*_{\text{Q8}}(\eta)$, computed using Q8 elements with full (9-point) integration, is plotted for unit E^+_{1111} and ϵ_I and for $\nu = 0.3$ in Figure 7.6. To reiterate, since Q8 and Q9 elements

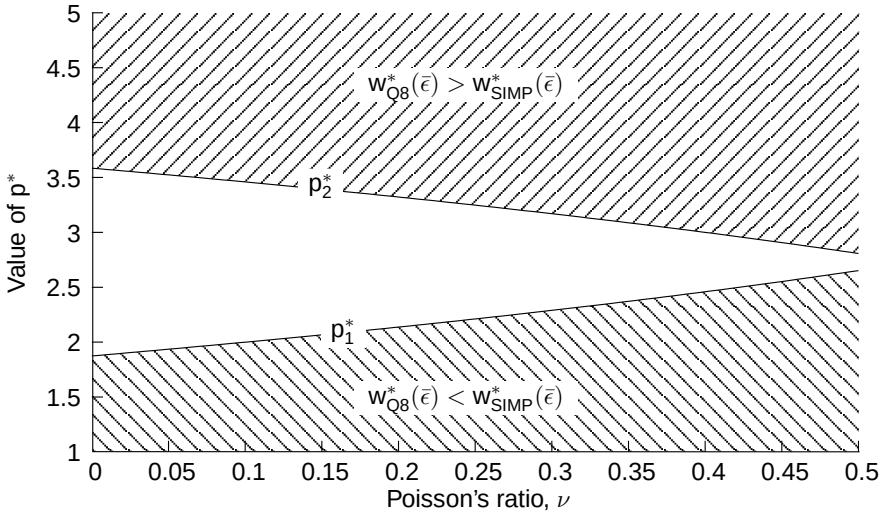

Figure 7.7: Variation of p^* for fully integrated Q8 elements.

result in identical effective material properties (see Table 7.1), the result of w^*_{Q9} is identical and given by (7.55), assuming the same integration scheme is employed. Also plotted in Figure 7.6, is $w^*_{\text{SIMP}}(\eta)$ computed using (7.53) for various values of penalty parameter p and $\rho = 1/2$. Clearly, for values of $1 \leq p < p^*_1$, $w^*_{\text{Q8}}(\eta) < w^*_{\text{SIMP}}(\eta)$, i.e. checkerboarding is unlikely, and when $p \geq p^*_2$, $w^*_{\text{Q8}}(\eta) \geq w^*_{\text{SIMP}}(\eta)$, i.e. checkerboarding is likely to occur (in both cases, independently of η).

For values of $p^*_1 < p < p^*_2$, $w^*_{\text{Q8}}(\eta)$ could be such that $w^*_{\text{Q8}}(\eta) < w^*_{\text{SIMP}}(\eta)$ or $w^*_{\text{Q8}}(\eta) > w^*_{\text{SIMP}}(\eta)$, depending on the strain being experienced. For example, if $p = 3$ in this example, $w^*_{\text{Q8}}(\eta) < w^*_{\text{SIMP}}(\eta)$ for $-1 \leq \eta \lessapprox -0.53$ and $w^*_{\text{Q8}}(\eta) > w^*_{\text{SIMP}}(\eta)$ for $-0.53 \lessapprox \eta \leq 1$.

Values of p^*_1 and p^*_2 can similarly be computed for each Poisson's ratio ν and plotted as shown in Figure 7.7. Values of p can therefore be selected using this figure so as to minimize the likelihood of checkerboarding. Since values of p as large as possible are desired (to penalize intermediate densities), a value of p^*_1 as large as possible is sought. If p^*_1 cannot be altered, the 'next best' would be to increase p^*_2.

Figures 7.8 and 7.9 depict the effect of applying the 5-point integration scheme on strain energy density, as a function of principal strain ratio η, for a patch of Q8 elements. The plot is for a material with $\nu = 0.3$, and as before, unit E^+_{1111} and ϵ_I. For clarity, only the 5-point scheme with weights $W_0 = 0.01$ and $W_0 = 8/30$ are depicted, together with the results computed using the 4-point and 9-point schemes for reference.

Clearly, applying the 5-point scheme with $W_0 = 0.01$ or $8/30$ significantly reduces the strain energy density associated with the considered straining modes. It can be shown that there is a monotonic increase in strain energy density with an increase in W_0. In fact, for weights close the the maximum permitted $8/3$, a higher strain energy density is estimated than the 9-point scheme.

Also shown in Figure 7.8 are the strain energy densities w^*_{SIMP}, calculated for different values of p. If $w^*_{\text{Q8}}(\bar{\epsilon}) > w^*_{\text{SIMP}}(\bar{\epsilon})$, checkerboarding is likely to occur. Therefore, application of reduced order integration schemes clearly reduces the likelihood of checkerboarding for

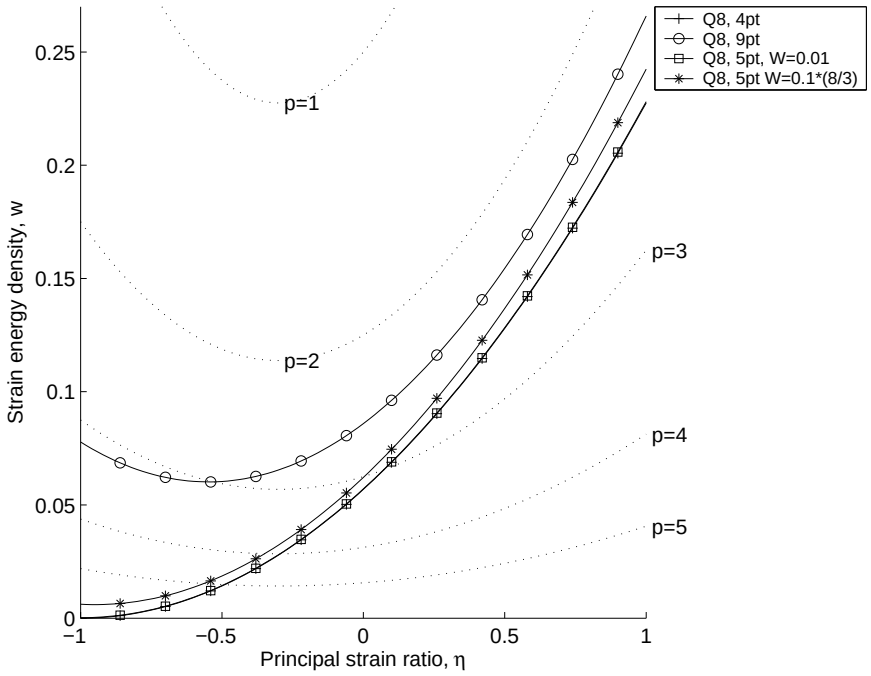

Figure 7.8: Strain energy density of Q8 elements with 5-point integration scheme.

a given p. Alternatively, it allows for the use of larger values of p without increasing the effective stiffness of the checkerboard patch of elements.

Finally, the minimum of w^*_{SIMP} computed using (7.53) occurs at $\eta = -\nu$, in this case $\eta = -0.3$. Increasing p simply decreases values of w^*_{SIMP}. However, computing the strain energy density of a patch of Q8 elements employing the various integration schemes, affects not only the value of $w^*_{\text{Q8}}(\eta)$, but also shifts the turning point towards $\eta = -1$ as the integration scheme becomes 'softer'. Unfortunately, this means that the gap between p^*_1 and p^*_2 is increased as will be shown in the next subsection.

For clarity, Figure 7.9 shows an enlargement of Figure 7.8, concentrating on the lower left corner. As described earlier, applying a 4-point integration scheme (which is equivalent to a 5-point scheme with $W_0 = 0$), results in zero strain energy being experienced at $\eta = -1$, corresponding to the rank deficiency in the constitutive matrix $\bar{E}$. Figure 7.9 also highlights the difference between the results employing the 4-point scheme and those using the 5-point scheme with $W_0 = 0.01$ and $8/30$, which is not clear in Figure 7.8.

Figures 7.10 and 7.11 depict the results for the same problem employing the 8-point scheme. Again, the results of the 4- and 9-point schemes are plotted together with results for w^*_{SIMP} for various values of p. Employing the 8-point scheme with $W_\beta = 40/49$ clearly produce identical results to those employing the 9-point scheme as expected. Again, employing low values of $W_\beta = 0.01$ and $8/90$ produce significantly lower values of strain energy density. Once again, an enlargement of Figure 7.10 is depicted in Figure 7.11. Slightly higher values of strain energy density are computed using the 8-point compared to the 5-point scheme for low weights, such as 0.01. This is significant, especially since the 5-point scheme is not recommended for Q9 elements.

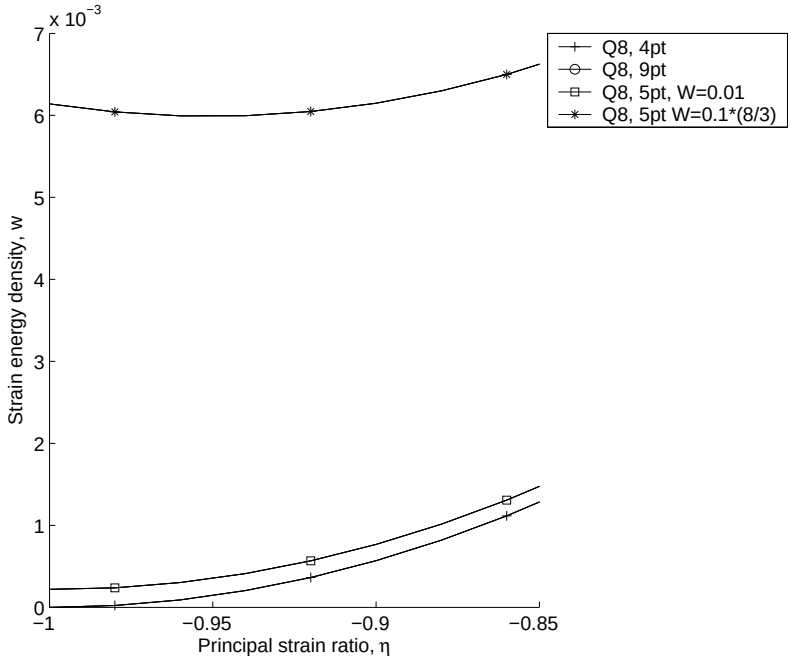

Figure 7.9: Zoom of strain energy density of Q8 elements with 5-point integration scheme.

7.6.4 Effect of integration scheme on penalty bounds p_1^* and p_2^*

Based on the computation of strain energy density for a checkerboard patch of Q8 elements compared to the expression for the SIMP material model in (7.53), limits of p can be determined for which $w^*_{\text{Q8}}(\bar{\epsilon}) < w^*_{\text{SIMP}}(\bar{\epsilon})$ (denoted $p_1^*(\nu)$) and $w^*_{\text{Q8}}(\bar{\epsilon}) > w^*_{\text{SIMP}}(\bar{\epsilon})$ (denoted $p_2^*(\nu)$) for each value of Poisson's ratio ν, as depicted in Figure 7.7.

In Figure 7.12, the values of $p_1^*(\nu)$ for Q8 elements employing the 5-point scheme are plotted, normalised with respect to the fully integrated equivalent, (shown in Figure 7.6). Also plotted as a reference are the values computed using 4- and 9-point integration schemes. The figure shows that employing the 5-point scheme with $W_0 = 0.01$ increases p_1^* significantly, almost to the level of the 4-point scheme. At a Poisson's ratio of $\nu = 0.3$ (common in engineering materials) an increase of approximately 10% is achieved employing this integration scheme. A slightly less marked increase is achieved employing the 5-point scheme with $W_0 = 8/30$.

Figure 7.13 depicts the results employing the 8-point scheme. In this case, the increase is approximately 10% for both weights $W_\beta = 0.01$ and $W_\beta = 8/90$. Once again, as expected, employing the 8-point scheme with a weight $W_\beta = 40/49$ results that are identical results to the results computed with the 9-point scheme.

Figures 7.14 and 7.15 depict the values of $p_2^*(\nu)$ for a patch of Q8 elements employing 5- and 8-point schemes, respectively. It was shown in Section 7.6.3, that for the 4-point scheme as $\eta \to -1$, $w^*_{\text{Q8}} \to 0$. This implies that $p_2^* \to \infty$. The results for the 4-point scheme are therefore not shown in Figures 7.14 and 7.15.

The scale of improvement for p_2^* is notably higher than that of p_1^*, with improvements of well over 300% for the 5-point scheme with $W_0 = 0.01$ and around 300% for the 8-point

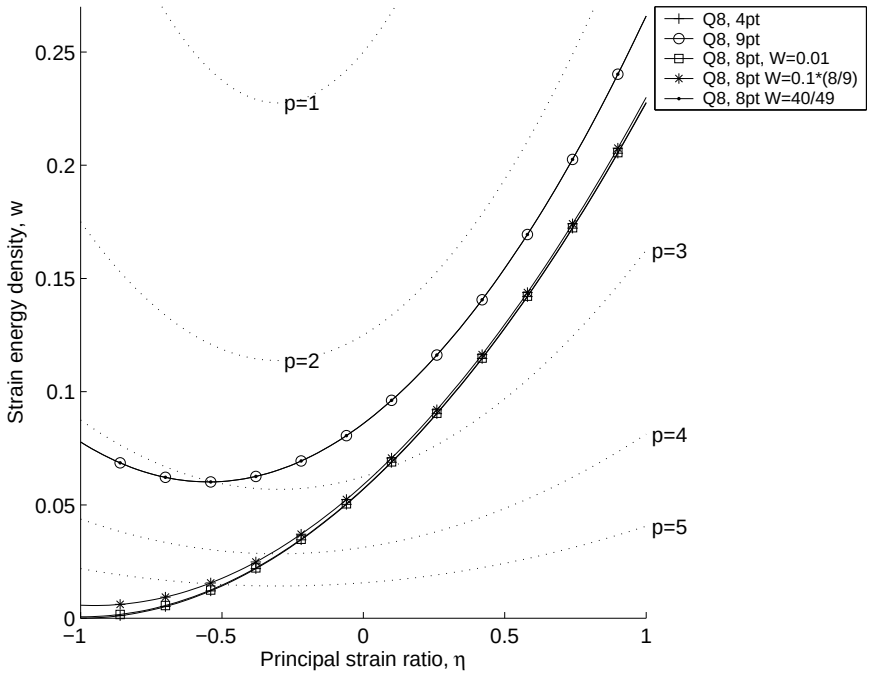

Figure 7.10: Strain energy density of Q8 elements with 8-point integration scheme.

scheme with $W_\beta = 0.01$. This results in a relatively wide range of values of p, for which checkerboarding likelihood depends on strain conditions. However, since reduced order integration does not add to element numerical cost (in fact cost is reduced) and accuracy is improved with no loss of stability, as shown in [140], it is recommend that our reduced order integration schemes be implemented for topology optimization problems.

7.7 Conclusions

Based on the theory of Díaz and Sigmund [14], the stiffness of checkerboard patches of various elements, employing different integration schemes have been assessed. Standard bilinear isoparametric 4-node elements and higher order 8- and 9-node elements as well as 4-node elements with in-plane rotational degrees of freedom are evaluated, employing full, reduced and modified reduced order integration schemes. The combinations of element and integration scheme which 'soften' the effective material tensor of a checkerboard patch of elements, effectively reducing the likelihood of checkerboarding in a topology optimization applications, are investigated.

Firstly, it is shown that both 4-node elements *with* drilling degrees of freedom (Q4X) and *without* (Q4) result in identical effective material properties for a checkerboard patch of elements. The additional degrees of freedom present in Q4X elements do not 'soften' the patch since none of the 3 linearly independent test strains applied to compute the effective material properties, activate the nodal in-plane rotations. It is however numerically demonstrated that for realistic problems, where nodal rotations are non-zero, checkerboarding is

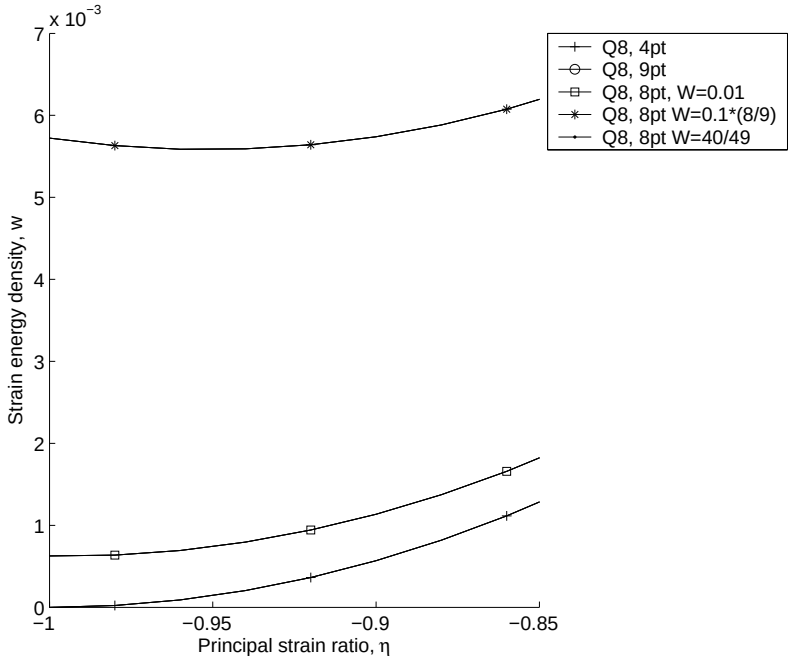

Figure 7.11: Zoom of strain energy density of Q8 elements with 8-point integration scheme.

notably reduced. However, since in the limit of mesh refinement only constant strain states are experienced, there is no guarantee that Q4X elements will unconditionally eliminate checkerboarding.

Next it is shown that undistorted higher order 8-node (Q8) and 9-node (Q9) elements result in identical effective material properties for the checkerboard patch of elements considered, if similar integration schemes are employed. It is shown that if a full (9-point) integration scheme is employed, both Q8 and Q9 elements result in effective material properties which are identical to the analytical solution computed by Díaz and Sigmund [14].

Q8 elements may be used with either 5-, 8- or 9-point integration schemes without the risk of introducing elemental rank deficiencies. Q9 elements are shown to be stable when using either 8- or 9-point schemes, with 4- and 5- point schemes resulting in communicable spurious modes.

The most significant improvements in terms of reducing the strain energy density (of a checkerboard patch) has been achieved by application of Q8 elements with a 5-point integration scheme with associated variable weight $W_0 = 0.01$. Employing this combination additionally increases the value of penalty which can be applied in the SIMP material parameterization without increasing the risk of checkerboarding. Specifically, p_1^*, the threshold at which checkerboarding is likely to occur independent of straining condition, is increased approximately 10%, while p_2^* is increased over 300% for common engineering materials This benefit is also cost-effective since employing the 5-point scheme simultaneously reduces computational cost, and increases the accuracy of the finite element approximation.

It is therefore recommended that Q8 elements with a 5-point integration scheme be used,

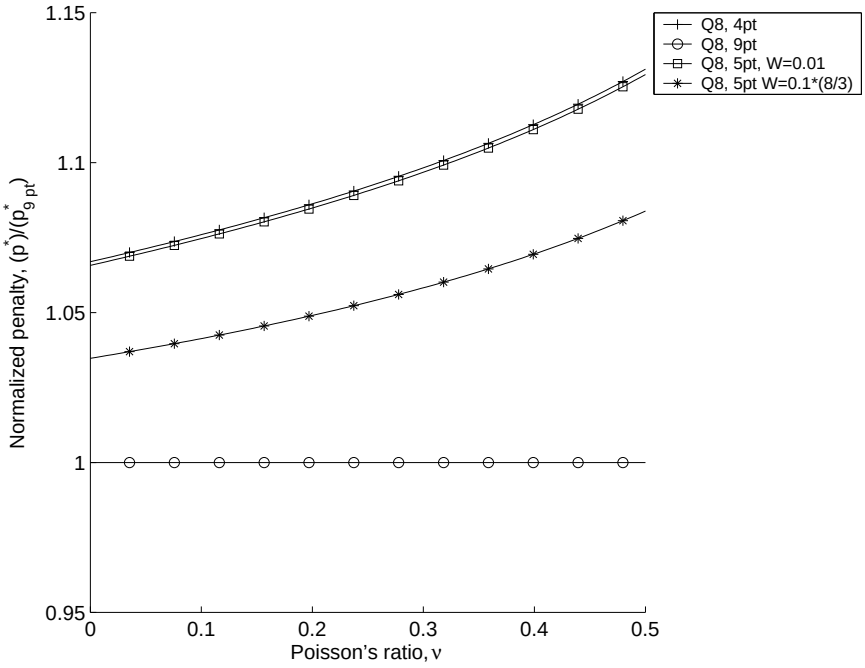

Figure 7.12: Effect of integration scheme setting on p_1^*: 5-point scheme.

instead of Q9 elements with full integration, when higher order elements are employed in SIMP topology optimization applications.

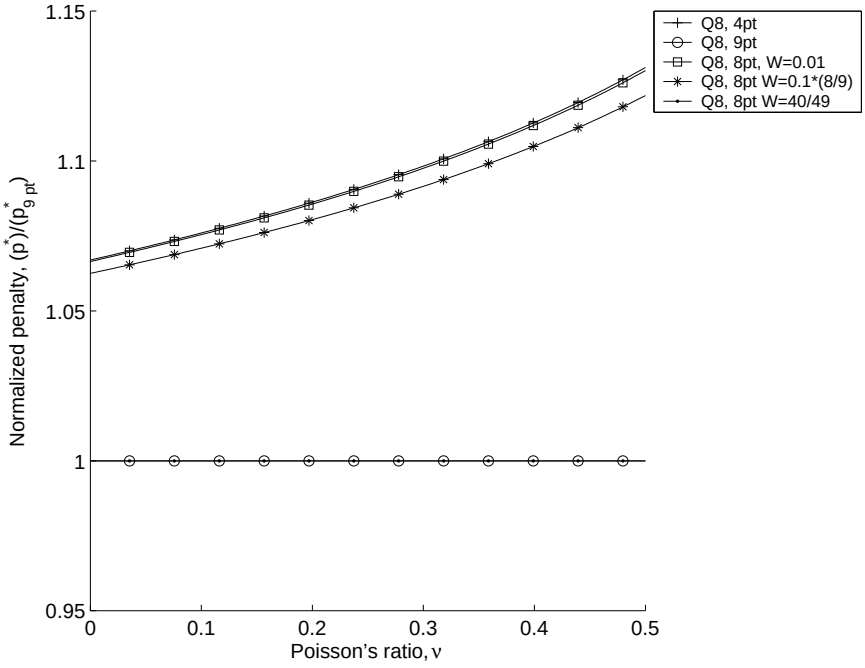

Figure 7.13: Effect of integration scheme setting on p_1^*: 8-point scheme.

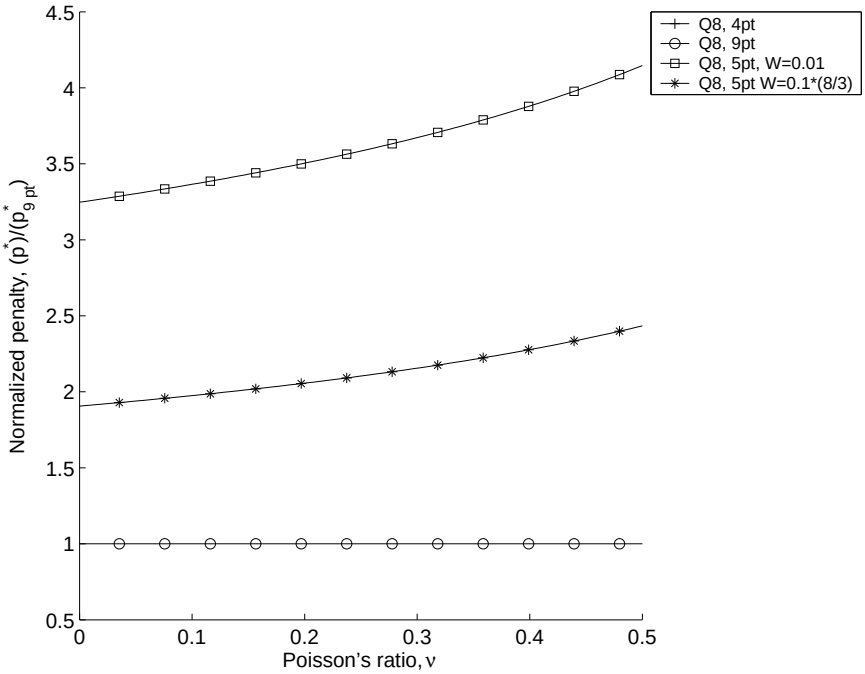

Figure 7.14: Effect of integration scheme setting on p_2^*: 5-point scheme.

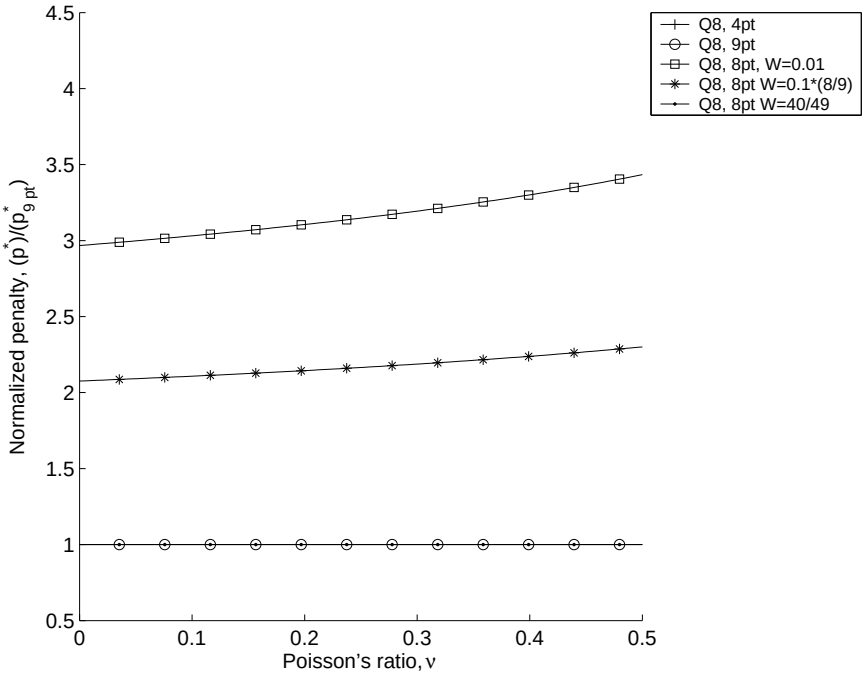

Figure 7.15: Effect of integration scheme setting on p_2^*: 8-point scheme.

Chapter 8

Conclusion

The stated objectives of this work were to:

1. Develop new finite elements, or elemental procedures, which not only improve model accuracy, robustness and/or efficiency, but can also be used in schemes which alleviate or eliminate the numerical instabilities, or improper modelling, associated with spurious material layouts in topology optimization.

2. Develop procedures which exploit the salient features of the new finite elements, or elemental procedures, in order to overcome or alleviate the numerical instabilities, or modelling deficiencies, leading to spurious material layouts in topology optimization.

These two main objectives formed the basis of this two part thesis. In the first part, emphasis is mainly concentrated on the development of planar finite elements and procedures. The stability of planar elastic elements with drilling degrees of freedom (DOFs) are considered, and piezoelectric finite elements with drilling DOFs are developed. Finally, reduced order integration schemes are applied to quadratic (Q8 and Q9) elements in order to enhance element accuracy.

In the second part of the thesis, the new finite elements, and elemental procedures, are applied in a topology optimization environment. Firstly, elements with drilling DOFs are exploited in the development of schemes to deal with problematic material layouts. The effect of element formulation on optimal topologies of membrane, plate and shell problems is then investigated. Finally it is shown how reduced order integration schemes soften checkerboard patches of higher order elements, making checkerboard material layouts less likely in optimal topologies.

In this final chapter, conclusions made during the course of the study, and evidence demonstrating that the objectives of the study have been met, are presented. Each chapter contains a presentation of specific scientific contributions made during the course of this study. As such, each chapter is intended to represent a self-contained work, which can be read in isolation of the remainder of the document. Therefore, the conclusions drawn from each chapter will also be presented separately.

8.1 PART I: Development of finite element technology

Effect of penalty parameter on elements with drilling DOFs
In Chapter 2, after a brief summary of historical developments in the formulation of elements with in-plane rotations, a numerical investigation into the effect of a penalty parameter in elements with drilling degrees of freedom is presented.

The parameter under investigation is usually denoted γ, and relates the in-plane translations and rotations. Rather than simply reporting on the quantitative influence of the penalty parameter γ on measures like displacement, rotation and stress, the skewness of the nonsymmetric part of the stress tensor is directly assessed. Results are presented for both isotropic and orthotropic constitutive relationships.

In general it is shown that, values smaller than $\gamma = \mu$, with μ the shear modulus, are desirable, even though the formulation is convergent for all values of γ. In implementing elements with drilling degrees of freedom based on the procedure suggested by Hughes and Brezzi [18], the skewness of the nonsymmetric part of the stress tensor, may directly be used to quantitatively assess the validity of selected values of γ.

Development of planar four node piezoelectric elements with drilling DOFs
In Chapter 3 a number of variational formulations accounting for piezoelectricity and in-plane rotations are presented. Two new functional families, namely M-type, which retains the skew-symmetric part of the stress tensor, and K-Type, in which the skew part of stress is eliminated, are introduced.

From the Hu-Washizu-like functionals (M- and K-type) irreducible formulations with only 'kinematic' independent variables, i.e. displacement and electric potential are developed. It is also shown how 'fully' mixed formulations, with stress and electric flux density assumed, are developed. Furthermore, 'degenerate' Hellinger-Reissner-like formulations with either stress or electric flux density assumed, are also presented. It is also illustrated how the family of functionals are related to one another.

The accuracy and robustness of these elements on a number of benchmark problems is demonstrated. The addition of drilling degrees of freedom enriches the interpolated displacement field, resulting in improved element performance. This is borne out by the improved accuracy and robustness of the irreducible elements with drilling DOFs over the standard bilinear piezoelectric element.

The improved performance of the mixed elements with drilling degrees of freedom is generally less marked when compared to existing mixed piezoelectric elements. In fact, it is difficult to conclusively state that any one of the elements used in the study is better in terms of accuracy than all the others, since none of the elements herein consistently outperforms all the other elements on all reported accuracy measures.

The 'fully mixed' elements, however, are shown to be accurate and stable, even at extreme element distortions. They also allow for improved modelling capabilities due to the additional rotational degree of freedom, e.g. compatibility with elastic elements with drilling degrees of freedom is ensured.

Modified reduced order quadratures for quadratic membrane elements
The use of modified reduced order quadrature integration rules in the evaluation of elemental matrices was the focus of Chapter 4. Modified reduced order quadrature rules as alternative numerical integration schemes for Q8 serendipity and Q9 Lagrange membrane finite elements are offered. For these elements, practitioners often either employ full integration, using order 3 Gauss rules, or reduced integration using an order 2 Gauss rule. However, full integration usually results in excessively stiff behavior while order 2 Gauss rules result in the introduction of spurious modes on the element level. Even though the spurious mode associated with the Q8 element is non-communicable, it remains undesirable, and may influence results in a number of situations of practical importance, e.g. vibration problems.

The 5 and 8 point schemes, proposed for respectively Q8 and Q9 elements, eliminate spurious zero energy modes, while element accuracy is enhanced as compared to order 3 Gauss rules, through the introduction of soft higher order deformation modes.

It is shown that for the Q8 element, both the 5 and 8 point rules can be used for integrating the element stiffness matrix. In each case the spurious mode is eliminated. Since the numerical cost of the 8 point scheme is higher than the 5 point scheme, with no other obvious benefits, it is recommended that Q8 elements be integrated using the 5 point rule. For the Q9 element, the 5 point rule is inadequate since only one of the three spurious modes is eliminated. It is therefore recommended that the 8 point rule be employed for elemental calculation of Q9 elements. Appropriate values for the variable weights which appear in the integration schemes are also suggested, so as to balance element accuracy and stability.

8.2 PART II: Application of finite element developments to topology optimization

Exploiting drilling DOFs to deal with checkerboarding, one-node hinges and diagonal members
The aim of Chapter 5 was to demonstrate that membrane finite elements with drilling DOFs can be exploited in schemes to treat problematic local material layouts, such as checkerboarding and one-node connected hinges. It is firstly demonstrated via numerical experimentation, that simply employing these elements in topology optimization problems, results in a significant reduction in the amount of checkerboarding in optimal topologies. The theoretical merits of this strategy are detailed in Chapter 7. In addition, drilling DOFs present a natural way of detecting and/or penalizing one-node connected hinges. It is therefore also shown how drilling DOFs can be used to improve on the numerical modelling of one-node hinges and diagonal structural members.

Two new schemes to deal with one-node hinges and diagonal members, exploiting drilling DOFs are suggested. The first scheme is based on NoHinge, a scheme originally proposed by Poulsen [15]. The modified scheme however, uses the rotations computed at internal nodes to distinguish between a material layout which is behaving as a hinge (in rotation) and a diagonal structural member subjected to only axial loads. This scheme however, requires

a somewhat numerically expensive constraint sensitivity computation. A second scheme in which a one-node hinge is modelled, such that the response is similar to a reasonable interpretation of the material layout, is also presented. A function which indicates whether or not an element takes part in a layout with unsuitable numerical representation, such as a one-node hinge, is developed. If such an element is detected, it is replaced by an equivalent beam model for improved modelling accuracy. Since the process is solely determined by the material layout, it is completely reversible. Using this new method, it is demonstrated that it is relatively easy to stiffen one-node hinges in compliant mechanism design, thereby penalizing their existence, and that this stiffening does not lead to checkerboarding.

This second scheme in particular seems a promising alternative to traditional methods which seek to simply eliminate these problematic material layouts altogether, and is therefore further applied in the design of a practical mirror scanning device. Firstly, standard filtering strategies are employed in the topology optimization of a mirror scanning device using three different problem formulations. The first seeks to simply maximize the output rotation, while the other two maximize some measure of stiffness subject to a required output rotation being maintained. Each of the resulting optimal topologies contain a number one-node hinges. Upon application of the newly proposed scheme, the formation of one-node hinges are however, effectively prevented.

Effect of finite element formulation on optimal topologies of generally curved shells structures

Chapter 6 presents an investigation into the effect of finite element formulation and elemental settings on optimal topologies of membrane, plate and shell minimum compliance problems. It is shown that for given optimization algorithm settings, the optimal topology which results is a function of the element type.

For membrane problems, it is demonstrated that both standard Q4 elements and element with drilling DOFs results in identical optimal topologies. Referring here to the stability of elements with drilling DOFs, studied in Chapter 2: Optimal topologies employing elements with drilling DOFs are shown to be largely insensitive to the value of the adjustable parameter γ over a large range of values.

Furthermore, the effect of the plate component of flat shell elements, is investigated. Results for Discrete Kirchhoff Quadrilateral (DKQ) elements, and two Mindlin-Reissner based elements, one employing Selective Reduced Integration (SRI) on transverse shear terms and the other employing an Assumed Natural Strain (ANS) formulation, are investigated and compared. The plate examples presented confirmed that, since the DKQ element is shear rigid, optimal topologies are not sensitive to plate thickness. Elements employing the ANS interpolations are shown to be robust reliable. The ANS elements consistently recovered thin plate results similar to the DKQ results. Mindlin-Reissner elements with SRI on transverse shear terms are shown to be 'softer' in transverse shear than the ANS Mindlin-Reissner based elements and are therefore more sensitive to plate thickness. However, the SRI element possesses a spurious communicable mode which occasionally renders this element unstable. A plate example is introduced which exemplifies the problem.

Finally, the effects of parameters related to drilling DOFs of shell problems are studied. It

is shown that optimal topologies computed with elements with drilling degrees of freedom based on sound mathematical theory are insensitive to the penalty parameter over a wide range. On the other hand, elements with an *ad hoc* treatment of drilling degrees of freedom are found to be far more sensitive to the adjustable parameter. This sensitivity to the adjustable parameter is furthermore shown to be problem dependent. This dependency is illustrated on a newly introduced benchmark problem in the form of a pretwisted beam.

Effect of reduced order integration schemes and elements with drilling DOFs on checkerboarding
The application of modified reduced order quadratures applied to quadratic membrane elements in a topology optimization environment, was the focus of Chapter 7.

Various elements, each employing different integration schemes, are assessed in term of the stiffness of a checkerboard patch of elements. The evaluation makes use of 4-node elements (with and without drilling degrees of freedom) as well as 8- and 9-node isoparametric elements, employing full and modified reduced order integration schemes. In particular, combinations of element and integration scheme which 'soften' the effective material tensor of a checkerboard patch of elements, (effectively reducing the likelihood of checkerboarding) are identified.

Firstly, it is shown that both 4-node elements with and without drilling degrees of freedom result in identical effective material properties for a checkerboard patch of elements. Since the additional straining modes associated with the drilling DOFs are not activated by the 3 linearly independent test strains applied to compute the effective material properties, elements with drilling DOFs do not affect the stiffness of a checkerboard patch. It is however numerically demonstrated that for realistic problems where nodal rotations are non-zero, checkerboarding is somewhat reduced. However, since in the limit of mesh refinement only constant strain states are experienced, there is no guarantee that elements with drilling DOFs will eliminate checkerboarding altogether.

Next it is shown that checkerboard layouts comprising higher order 8-node (Q8) and 9-node (Q9) elements employing modified reduced order integration schemes are significantly softened. The most significant improvements, in terms of softening, are achieved using the 5-point scheme in conjunction with Q8 elements. Employing this combination significantly reduces strain energy density associated with a checkerboard patch under prescribed strain. This benefit is also numerically cost-effective since employing the 5-point scheme simultaneously reduces computational cost, and increases the accuracy of the finite element approximation.

8.3 Suggested future work

Although the main objectives of the study have been successfully accomplished, the research topics have not been exhaustively addressed. For example, many of the (planar) finite element developments presented in this study could be extended to the more general three-dimensional case: The variational formulations presented in Chapter 3 are valid for planar

two-dimensional and general three-dimensional finite element development. Solid three-dimensional elastostatic elements with rotational degrees of freedom have previously been implemented by for example Choi *et al.* [148]. It should therefore also be possible to develop solid equivalents of the planar piezoelectric elements with rotational degrees of freedom presented in Chapter 3. Furthermore, in theory, it is possible to develop modified reduced order integration schemes, equivalent to those presented in Chapter 4 and to apply them in the calculation of solid three-dimensional finite elements to enhance element accuracy and reduce computational cost.

Naturally the two aforementioned solid finite element developments would also allow the schemes and theory presented in Chapters 5 and 7 to be extended to the three dimensional case if so desired.

Furthermore, in Chapter 5, two schemes exploiting elements with drilling degrees of freedom were presented. Although acceptable results were achieved, a more elegant beam representation of a one-node connected hinge (and a diagonal member) for the scheme denoted Scheme II in Section 5.5.2 would be helpful in improving the accuracy of the method.

Finally, the application of topology optimization in the synthesis of plate and shell compliant mechanisms for micropositioning problems could be attempted. A simple piezoelectric shell element has already been implemented, and its application in topology optimization problems awaits attention.